GEORGIA DOT RESEARCH PROJECT 22-21

Final Report

PHASE III: INVESTIGATION AND GUIDELINES FOR BEST PRACTICES OF THERMAL CONTROL FOR MASS CONCRETE CONSTRUCTION PROJECTS

Office of Performance-based Management and Research
600 West Peachtree Street NW | Atlanta, GA 30308

September 2025

TECHNICAL REPORT DOCUMENTATION PAGE

1. Report No.: FHWA-GA-25-2221	2. Government Accession No.: N/A	3. Recipient's Catalog No.: N/A	
4. Title and Subtitle: Phase III: Investigation and Guidelines for Best Practices of Thermal Control for Mass Concrete Construction Projects		5. Report Date: September 2025	
		6. Performing Organization Code: N/A	
7. Author(s): Yong Kwon Cho (PI), Ph.D.; Russell Gentry (coPI), Ph.D.; Kimberly Kurtis (coPI), Ph.D.; Jason Brown (Senior Research Engineer), Ph.D.; Luna Al Hasani (Senior Research Engineer), Ph. D.; Seongyong Kim (Graduate Research Assistant); Soo Hyun Lee (Associate Research Engineer)		8. Performing Organ. Report No.: 22-21	
9. Performing Organization Name and Address: Georgia Institute of Technology, 225 North Ave NW Atlanta, GA 30332, Phone: (404) 385-2038, Email: yong.cho@ce.gatech.edu		10. Work Unit No.: N/A	
		11. Contract or Grant No.: PI # 0019326	
12. Sponsoring Agency Name and Address: Georgia Department of Transportation, Office of Performance-based Management and Research, 600 West Peachtree NW, Atlanta, GA, 30308		13. Type of Report and Period Covered: Final Report(Sept. 2022 – Sept. 2025)	
		14. Sponsoring Agency Code: N/A	
15. Supplementary Notes: Prepared in cooperation with the U.S. Department of Transportation, Federal Highway Administration.			

16. Abstract:

The objective of this research is to expand and validate decision-making tools and best practices for mass concrete thermal management, integrating emerging cementitious materials. Building on the foundations established in previous phases, this project evaluates an expanded range of concrete mix designs—including Type IL cement and reclaimed fly ash—and extends the applicability of nomogram-based tools across diverse thermal control scenarios. The study focuses on validating and refining the decision-making aids developed in Phase II, enhancing their predictive accuracy under varying geometries, cooling methods, and material compositions. Comprehensive simulations, laboratory testing, and a field-based simulation case study at the Albany Bridge project assess the thermal performance of the novel mix types associated with cooling methods. Findings indicate that SCM-rich mixes, particularly those with 40% reclaimed fly ash, effectively mitigate thermal gradients while maintaining compressive strength without requiring active cooling systems. The results emphasize the viability of pre-cooling and passive insulation as cost-effective strategies, providing GDOT with actionable guidance for sustainable mass concrete construction. The research further demonstrates that integrating SCM-rich mixes not only reduces thermal gradients but also shortens curing durations, leading to potential cost savings in labor and material expenses. The findings underscore the strategic importance of adopting reclaimed fly ash as a sustainable alternative amidst declining fly ash availability, aligning thermal control practices with broader environmental objectives.

17. Key Words: Mass Concrete, Construction, Thermal Control, Nomograph, Cost Analysis		18. Distribution Statement: No restrictions	
19. Security Classification (of this report): Unclassified	20. Security Classification (of this page): Unclassified	21. No. of Pages: 109	22. Price: Free

Form DOT F 1700.7(8-72) Reproduction of completed page authorized.

GDOT Research Project 22-21

Final Report

PHASE III: INVESTIGATION AND GUIDELINES FOR BEST PRACTICES OF THERMAL CONTROL FOR MASS CONCRETE CONSTRUCTION PROJECTS

By

Yong Kwon Cho, Ph.D.
Professor, School of Civil and Environmental Engineering

Russell Gentry, Ph.D.
Professor, School of Architecture

Kimberly Kurtis, Ph.D.
Professor, School of Civil and Environmental Engineering

Jason Brown, Ph.D.
Senior Research Engineer, School of Civil and Environmental Engineering

Luna Al Hasani, Ph.D.
Senior Research Engineer, School of Civil and Environmental Engineering

Seongyong Kim
Graduate Research Assistant, School of Civil and Environmental Engineering

Soo Hyun Lee
Associate Research Engineer, School of Civil and Environmental Engineering

Georgia Tech Research

Corporation

Contract with
Georgia Department of Transportation

In cooperation with
U.S. Department of Transportation, Federal Highway Administration

September 2025

The contents of this report reflect the views of the authors, who are responsible for the facts and the accuracy of the data presented herein. The contents do not necessarily reflect the official views or policies of the Georgia Department of Transportation or Federal Highway Administration. This report does not constitute a standard, specification, or regulation.

SI* (MODERN METRIC) CONVERSION FACTORS

APPROXIMATE CONVERSIONS TO SI UNITS

Symbol	When You Know	Multiply By	To Find	Symbol
		LENGTH		
in	inches	25.4	millimeters	mm
ft	feet	0.305	meters	m
yd	yards	0.914	meters	m
mi	miles	1.61	kilometers	km
		AREA		
in^2	square inches	645.2	square millimeters	mm^2
ft^2	square feet	0.093	square meters	m^2
yd^2	square yard	0.836	square meters	m^2
ac	acres	0.405	hectares	ha
mi^2	square miles	2.59	square kilometers	km^2
		VOLUME		
fl oz	fluid ounces	29.57	milliliters	mL
gal	gallons	3.785	liters	L
ft^3	cubic feet	0.028	cubic meters	m^3
yd^3	cubic yards	0.765	cubic meters	m^3
		NOTE: volumes greater than 1000 L shall be shown in m^3		
		MASS		
oz	ounces	28.35	grams	g
lb	pounds	0.454	kilograms	kg
T	short tons (2000 lb)	0.907	megagrams (or "metric ton")	Mg (or "t")
		TEMPERATURE (exact degrees)		
°F	Fahrenheit	5 (F-32)/9 or (F-32)/1.8	Celsius	°C
		ILLUMINATION		
fc	foot-candles	10.76	lux	lx
fl	foot-Lamberts	3.426	candela/m^2	cd/m^2
		FORCE and PRESSURE or STRESS		
lbf	poundforce	4.45	newtons	N
lbf/in^2	poundforce per square inch	6.89	kilopascals	kPa

APPROXIMATE CONVERSIONS FROM SI UNITS

Symbol	When You Know	Multiply By	To Find	Symbol
		LENGTH		
mm	millimeters	0.039	inches	in
m	meters	3.28	feet	ft
m	meters	1.09	yards	yd
km	kilometers	0.621	miles	mi
		AREA		
mm^2	square millimeters	0.0016	square inches	in^2
m^2	square meters	10.764	square feet	ft^2
m^2	square meters	1.195	square yards	yd^2
ha	hectares	2.47	acres	ac
km^2	square kilometers	0.386	square miles	mi^2
		VOLUME		
mL	milliliters	0.034	fluid ounces	fl oz
L	liters	0.264	gallons	gal
m^3	cubic meters	35.314	cubic feet	ft^3
m^3	cubic meters	1.307	cubic yards	yd^3
		MASS		
g	grams	0.035	ounces	oz
kg	kilograms	2.202	pounds	lb
Mg (or "t")	megagrams (or "metric ton")	1.103	short tons (2000 lb)	T
		TEMPERATURE (exact degrees)		
°C	Celsius	1.8C+32	Fahrenheit	°F
		ILLUMINATION		
lx	lux	0.0929	foot-candles	fc
cd/m^2	candela/m^2	0.2919	foot-Lamberts	fl
		FORCE and PRESSURE or STRESS		
N	newtons	0.225	poundforce	lbf
kPa	kilopascals	0.145	poundforce per square inch	lbf/in^2

* SI is the symbol for the International System of Units. Appropriate rounding should be made to comply with Section 4 of ASTM E380. (Revised March 2003)

TABLE OF CONTENTS

EXECUTIVE SUMMARY 1

CHAPTER 1. INTRODUCTION 6

CHAPTER 2. EMERGING CEMENT AND SCM COMBINATIONS ANALYSIS THROUGH SIMULATION AND LAB TESTS (TASK 1) 9

- THERMAL MANAGEMENT STRATEGIES AND CONCRETE MIX DESIGNS ACROSS PHASES I-III 9
  - GDOT thermal control requirements for mass concrete 9
  - Review of thermal management strategies in Phase I and II 10
  - Characterization of Heat of Hydration 11
  - Phase II Mix Designs and Evaluation Results 12
  - Motivation for Phase III: Industry Shifts and Research Gaps 13
- INVESTIGATING NEW CEMENT AND SCM COMBINATIONS 14
  - Mix Type Selection 14
- LABORATORY TESTS TO ASSESS THERMAL PROPERTIES 15
  - Isothermal Calorimetry 16
  - Compressive Strength 18
  - Semi-adiabatic Calorimetry 20
- SUITABLE MIXTURE DESIGNS RECOMMENDATIONS 21
- CONCLUSION 24

CHAPTER 3. VALIDATION, EXTENSION, AND REFINEMENT OF NOMOGRAMS DEVELOPED FROM PHASE II (TASK 2) 26

- BAYESIAN STATISTICAL MODEL AND NOMOGRAM FOR NO-POSTCOOLING 27
- BASIC MODEL RESULTS 30
  - USCS units 30
- NOMOGRAM OF THE NO-POSTCOOLING SURROGATE MODEL 39
- GREEN'S FUNCTION SOLUTION TO 3D THERMAL CONCRETE HYDRATION PROBLEM 41
- CONCLUSION 46

CHAPTER 4. IDENTIFICATION OF TIME-COST TRADEOFF AMONG THERMAL CONTROL METHODS (TASK 3) 48

- OVERVIEW OF THE ECONOMIC ANALYSIS APPROACH 48
- COST ESTIMATION AND INDUSTRIAL PREFERENCE 48
- REVIEW OF SR-92 SITE FOR SIMULATION BASELINE 50
- THERMAL ASSESSMENT SIMULATION USING B4CAST 52

Analysis Methodology 53
Key Parameters and Configurations 54
Analysis Outcomes....55
Scenario-Based Case Study: Time–Cost Trade-Off Exploration 57
FINDINGS AND IMPLICATIONS 63
CHAPTER 5. CASE STUDY: INVESTIGATION OF ALTERNATIVE METHODS TO AVOID ACTIVE COOLING (TASK 4)....65
INTRODUCTION TO NON-ACTIVE COOLING STRATEGIES 65
SITE OVERVIEW: ALBANY BRIDGE CONSTRUCTION 66
B4CAST SIMULATION 67
Mass Concrete Components 67
Simulation Parameters....69
FINGDINS AND ANALYSIS 71
Intermediate Bent Analysis....71
Caisson Analysis 72
Alternatives for Mass Concrete Construction 74
CONCLUSION....76
CHAPTER 6. THE BEST PRACTICE GUIDELINE FOR MASS CONCRETE 77
MATERIAL SELECTION 77
THERMAL CONTROL METHODS 77
DECISION-MAKING 78
IMPLEMENTATION AND MONITORING 78
CHAPTER 7. CONCLUSION 80
ACKNOWLEDGMENTS....82
REFERENCES....83
APPENDIX....1
Point estimates for G and L in SI units....1
Derivation of the Green's function solution for temperature 1
Derivation of the Green's function solution for temperature gradient....12
Derivatives of the boundary condition component 13
Derivatives of the energy generation component 14
Derivatives of the spatial terms....14

LIST OF FIGURES

Figure 1. Compressive strength of concrete results 20
Figure 2. Semi-Adiabatic Calorimetry Experimental Setup 21
Figure 3. Rate of heat of hydration curve. 23
Figure 4. Cumulative heat of hydration curve. 24
Figure 5. Basic model results sampled from Phase II and Phase III data, shown for cases with $V/qA \geq 1$ ft ≈ 0.4 m and $Ti \geq 10 \circ C = 50 \circ F$. 32
Figure 6. Histogram of prediction errors for the basic model under the same conditions as Figure 5. 32
Figure 7. Basic model results sampled from Phase II and Phase III data, shown for cases with V/qA<1.. 34
Figure 8. Histogram of prediction errors for the basic model under the same conditions as Figure 7. 35
Figure 9. Bayesian surrogate model results, showing testing data where V/qA >=1. 38
Figure 10. Histogram of prediction errors from the Bayesian surrogate model. 39
Figure 11. Nomogram of the Bayesian surrogate model. 40
Figure 12. Temperature profiles from Green's function and finite element analysis (FEA) simulations at the same locations. 42
Figure 13. Comparison of maximum temperatures predicted by the Green's function model and FEA simulations using concrete mix designs from Phase II and Phase III. 43
Figure 14. Green's function and FEA simulation results using the parameter G estimated separately for non-fly ash mixes and for mixes containing fly ash. 44
Figure 15.Green's function and FEA simulation comparison showing that the Green's function model overpredicts maximum temperature by approximately 2 °F. 45
Figure 16. Example illustrating how closed-form equations allow analytical calculation of the temperature gradient. 46
Figure 17. Cross-section view of abutment and foundation of SR-92 bridge. 51
Figure 18. Post cooling system used in the SR-92 concrete abutment. 52
Figure 19. Relative cost vs. thermal control duration. 61
Figure 20. Total Effective Cost vs. duration, incorporating indirect time cost. 62
Figure 21. Location of Albany bridge construction project. 67
Figure 22. Cross-Section view of drilled caisson geometry. 68
Figure 23. Cross-section view of intermediate bent geometry. 69
Figure 24. B4Cast model of intermediate bent with 2'x4' layout. 72
Figure 25. B4Cast model of caisson with 5 pipes layout. 73
Figure 26. Intermediate bent simulation results. 73
Figure 27. Underwater caisson simulation results. 74
Figure 28. Typical caisson in air simulation results. 74
Figure 29. Surrogate model results. 75

LIST OF TABLES

Table 1. Cementitious pastes used in isothermal calorimetry tests. 18
Table 2. Concrete mix designs with selected pastes 19
Table 3. Summary statistics for parameter distributions in the Bayesian model. 37
Table 4. The conditions of the concrete placement in SR92 site. 52
Table 5. B4Cast thermal analysis focusing on passive cooling strategies. 56
Table 6. Cost component weights and factors. 59
Table 7. B4Cast thermal analysis input variables for Albany Bridge site. 70

EXECUTIVE SUMMARY

The Georgia Department of Transportation (GDOT) sponsored the Phase III research project titled "Investigation and Guidelines for Best Practices of Mass Concrete Construction Management" (RP 22-21) to advance the state-of-practice in thermal control for mass concrete elements. Conducted by the Georgia Tech Research Team, this 30-month effort builds directly upon prior work in Phases I and II but with a significantly expanded scope and a refined focus to address emerging challenges in material use, cost-efficiency, and practical implementation.

Whereas Phase I and II established baseline understanding of mass concrete behavior, explored standard mix designs, and introduced early-stage decision tools (e.g., draft nomograms), Phase III transitions the research into field application and simulation by focusing on validation, real-world adaptability, and optimization across a broader range of material options and construction site scenarios. The research explicitly tackles the increasing variability in cement and SCM availability, integrates advanced optimization techniques, and redefines guidance for balancing time and cost in thermal control.

The core objectives of this phase include:

- **Task 1. Evaluating Emerging Cement and SCM Combinations.**

The investigation of emerging cement and SCM combinations demonstrated that incorporating Type IL cement and reclaimed fly ash as partial replacements for conventional cementitious materials can effectively reduce heat generation while maintaining adequate compressive strength for mass concrete applications. The laboratory tests, including isothermal calorimetry and semi-adiabatic calorimetry, indicated that SCM-rich mixes, particularly those with 40% reclaimed fly ash (ILRF40), achieved lower peak temperatures and minimized thermal gradients without compromising structural integrity. Additionally, reclaimed fly ash exhibited comparable performance to conventional Class F fly ash, providing a sustainable alternative

amidst declining fly ash availability.

- **Task 2. Refining and Validating Nomograms.**

Three new analytical models of the thermal response to concrete hydration in non-postcooled conditions were developed. The first is a simple model to predict maximum concrete temperatures and was intended to be cast in nomogram form. This model is less ad-hoc and has greater physics content than the model used in Phase II; it envisions real (diathermal) concrete temperatures during hydration to be a diathermal correction, i.e., a temperature loss subtracted from the adiabatic temperature rise. The model was built by regression of over 890 finite element simulations incorporating isothermal calorimetry data collected during both Phase II and Phase III. In addition, this simple model was implemented in a Bayesian statistical framework to quantify uncertainty and generate confidence intervals for predicted values. A nomogram representing the top-line component of this simple model was also constructed to visualize the model output, enabling practitioners to estimate thermal risk for various mix designs and placements. Validation against simulations showed strong agreement, with 89% of predictions falling within the model's uncertainty band.

The second analytical model, in contrast to the simple model, is a complex, closed-form solution to the three-dimensional transient heat diffusion equation for hydrating concrete in non-postcooled conditions. This model, which computes temperatures at all locations and times of a hydrating concrete cuboid, was developed using Green's functions, which were made possible by using the same underlying cement hydration model as the simple model. This model was originally built to help examine the interrelations among the parameters to support nomogram construction of the simple model; the simple model above involves two equations that, while fairly simple, are nevertheless cumbersome to represent as nomograms and are likely better deployed in software or manual calculation. The Green's function model is conservative and

compares well to finite-element simulations in mixes without fly ash (overpredicting maximum temperatures by 2 °F) but overpredicts maximum temperatures by 10-20 °F in mixtures with fly ash, with the greatest overpredictions at low initial temperatures. However, its form suggests no path to packaging the simple model fully in practicable nomograms. Nevertheless, this second model, while complex and essentially requiring software implementation for practical use, is quite fast and may be combined with standard optimization routines to calculate maximum temperatures at greater speeds than finite-element simulations.

Furthermore, despite being complex, it is easy to analytically take the gradient of this model, which yields a third analytical model, this time for the temperature gradient at all locations and all times within a hydrating concrete cuboid. The model also demonstrated good agreement when compared with finite element simulations. This was developed late in Phase III; however, we hope it may be useful in future research studying the effects of spatial temperature differences.

The resulting tools improve early-stage planning by allowing rapid screening of temperature risks under various construction scenarios.

- **Task 3. Time-Cost Tradeoff Modeling of Thermal Control Methods.**

The economic analysis revealed that the incorporation of SCMs, specifically reclaimed fly ash and Portland Limestone Cement, reduced thermal control costs by minimizing the need for active cooling systems. High SCM replacement mixes, such as IL+RF40 and IL+F40, demonstrated reduced adiabatic heat rise and maintained temperature differentials within GDOT limits under passive insulation alone. This facilitated shorter thermal control durations allowing for form removal and project completion up to seven days earlier than conventional mixes, yielding notable cost savings in labor and material expenses. Additionally, the time-cost tradeoff analysis emphasized the economic feasibility of combining SCM-rich mixes with minimal

cooling interventions as a viable strategy for sustainable mass concrete construction.

- **Task 4. Investigating Alternatives to Active Cooling through a Simulation-based Case Study**

To reduce the cost and logistical complexity of embedded cooling systems, the research team conducted a simulation-based case study using the Flint River Bridge Project in Albany as a reference. The study focused on exploring strategies involving pre-cooling, passive cooling, and different mix designs aimed at eliminating the need for active cooling, which utilizes the embedded cooling pipes. Using B4Cast thermal simulations, the team analyzed the thermal behavior of mass concrete elements, including the intermediate bent and caissons, under real-world conditions. The results demonstrated that a strategic combination of high fly ash replacement, passive insulation, and pre-cooling measures effectively reduced peak temperatures, making active cooling unnecessary in certain scenarios without exceeding GDOT's thermal limits. These findings highlight how advanced material selection and thermal simulation can serve as practical alternatives to mechanical cooling.

Impact

This research directly empowers GDOT and its contractors with validated tools and evidence-based guidance to make smarter, more cost-effective decisions in mass concrete construction. By advancing from theoretical modeling to practical validation and optimization, the work of Phase III addresses long-standing industry pain points: overreliance on conservative (and costly) cooling methods, lack of standardization in thermal management, and limited adaptability to material market changes.

The outputs of this research not only reduce the risk of early-age cracking and long-term durability issues but also support improved project scheduling and budgeting. These improvements contribute to more sustainable and economically sound infrastructure investments

across the state of Georgia.

Ultimately, Phase III transforms the earlier proof-of-concept tools into robust, scalable solutions that align with GDOT's operational needs, setting the foundation for future mass concrete specifications rooted in empirical evidence and computational intelligence.

CHAPTER 1. INTRODUCTION

The Georgia Department of Transportation defines mass concrete as "any large volume of cast-in-place concrete with dimensions large enough to require that measures be taken to cope with the generation of heat and attendant volume change to minimize cracking," specifying that concrete elements with the least dimension greater than 5 ft (or drilled shafts greater than 6 ft in diameter) are designated as mass concrete (Georgia Department of Transportation, 2013). To manage mass concrete effectively, GDOT permits contractors to utilize approved cooling methods, provided they maintain an internal-to-external temperature differential of 35°F or less and do not exceed a maximum internal temperature of 158°F. Failure to properly control these parameters can lead to delayed ettringite formation, potentially causing significant long-term durability issues, or early-age thermal cracking, increasing maintenance costs and reducing structural longevity (Rashidi et al., 2017). In addition to thermal requirements, structural adequacy must also be ensured. In these projects, a compressive strength of 4,000 psi was adopted as a representative benchmark based on the previous GDOT bridge project requirements; 28-day strength is a typical reference point aligning with the design requirement for concrete class AA1, but a concrete mix was considered to meet the strength criterion once it eventually reached 4,000 psi, regardless of age. This flexibility allowed the inclusion of low-heat mix designs with slower early-age strength gain, which are advantageous in managing thermal risk in mass concrete placements.

There are typically three approaches to managing mass concrete temperature: 1) employing supplemental cementitious materials (SCMs) to alter concrete's exothermic profile, 2) pre-cooling concrete mixtures to reduce peak temperatures and thermal gradients, and 3) active cooling through embedded pipes to directly manage temperatures. Although active

cooling methods increase direct construction costs significantly, they often shorten the duration of thermal control activities, thus potentially reducing indirect project costs associated with construction delays.

In earlier phases of this research project, various mix designs and thermal control strategies for mass concrete have been explored, yielding valuable insights into optimal approaches. Specifically, Phase II efforts established nomogram-based decision-making tools that simplify selecting appropriate thermal management strategies. Despite these advancements, these nomograms remain preliminary and require additional validation and refinement to increase their robustness and expand their applicability.

Emerging challenges further complicate mass concrete management. Recent trends include increased use of Portland Limestone Cement (PLC) in place of conventional Portland cement, alongside declining availability of traditional SCMs such as fly ash. These shifts necessitate exploring alternative materials and combinations to continue meeting stringent thermal control requirements effectively.

This Phase III research aims to address these evolving challenges through a comprehensive approach encompassing the following tasks:

- Investigation of emerging cement and SCM combinations through extensive simulations and laboratory testing
- Validation, extension, and refinement of previously developed nomograms to include additional concrete mixes and thermal scenarios
- Identification of optimal time-cost tradeoffs among available thermal control methods
- Exploration of alternatives to active cooling, validated through real-world and laboratory case studies

Ultimately, this research endeavors to deliver validated, standardized thermal

management tools and guidelines, enabling efficient, cost-effective mass concrete construction practices tailored specifically to Georgia's infrastructure projects. This initiative will support GDOT in implementing robust thermal control strategies, enhancing structural performance, reducing maintenance costs, and benefiting public safety and infrastructure longevity statewide.

CHAPTER 2. EMERGING CEMENT AND SCM COMBINATIONS ANALYSIS THROUGH SIMULATION AND LAB TESTS (TASK 1)

THERMAL MANAGEMENT STRATEGIES AND CONCRETE MIX DESIGNS ACROSS PHASES I-III

The work conducted during Phase II of the research provided a critical foundation for understanding the thermal behavior of mass concrete and for formulating mix designs that minimize the risk of thermal cracking and excessive heat generation. In Phase II, the research team systematically investigated several concrete mixtures incorporating various supplementary cementitious materials (SCMs), including Class F fly ash and blast furnace slag (BFS), as well as a coarser cement alternative (Type II MH) with reduced fineness. These alternatives were evaluated to mitigate excessive internal temperature rise during hydration, which can compromise long-term durability and structural performance.

GDOT thermal control requirements for mass concrete

The Georgia Department of Transportation defines mass concrete as any structural element with dimensions large enough to require thermal control due to the risk of excessive internal temperature rise. According to GDOT specifications, the maximum allowable internal temperature for mass concrete is 158°F (70°C) to prevent deleterious effects such as delayed ettringite formation (DEF) which can compromise long-term durability. In addition, GDOT mandates that the maximum temperature differential between the interior and surface of the concrete element should not exceed 35°F (19°C) during the early-age curing period. These thermal thresholds aim to minimize the risk of thermal cracking due to non-uniform temperature distributions and restraint stresses, particularly in heavily reinforced or thick structural components. Meeting these limits often requires contractors to implement active or passive cooling strategies, carefully control initial placement

temperatures, and select mix designs with reduced heat of hydration.

Review of thermal management strategies in Phase I and II

Phase I of the mass concrete project involved the investigation of low-heat concrete mix designs for mass concrete (Cho et al., 2019). The proposed mix designs in Phase I included the incorporation of conventional SCMs (fly ash and slag) as partial replacement of type I/II Portland cement, or the use of specialty coarse cement that has low heat of hydration. The behavior of the mix designs was evaluated using semi-adiabatic mid-scale concrete mockups performed in the lab.

Phase II involved the use of a case study to further demonstrate the behavior of the mix designs proposed in Phase I (Cho et al., 2022). The SR-92 project in Douglasville, Georgia, served as a motivation case study (Al-Hasani et al., 2024). The six-foot-thick abutment walls in SR-92 were constructed using a straight cement concrete (no SCMs) with a relatively high cementitious content. For this reason, both the maximum temperature and temperature differences would have been exceeded if additional measures had not been put in place. The concrete placement temperature was reduced by using liquid nitrogen during batching, and the walls were actively cooled using an embedded cooling pipe system to control temperature exceedance. The walls were insulated using blankets during construction to control the temperature difference between the core and the surface of the elements. Therefore, the thermal control plan of the walls was both uneconomical and tedious.

An alternate thermal control plan was devised for the SR-92 abutment walls during Phase II. Several factors were investigated. The focus on the material characterization scale was on the use of the low-heat of hydration mix designs from Phase I and the robust characterization of the heat of hydration of the mix designs.

Characterization of Heat of Hydration

An essential step in mass concrete thermal modeling is the characterization of the heat of hydration of the mix design. This is usually determined through experimentation or empirical formulations. There are published empirical formulas that estimate the heat of hydration of mix designs based on the mix design proportions and the chemical properties of the cement and SCMs used. The most widely used model, referred to as the three-parameter exponential model, is an empirical model calibrated more than a decade ago using hundreds of mix designs with varying proportions and properties (Riding et al., 2012; Schindler & Folliard, 2005). The materials involved in the calibration included Portland cement and conventional SCMs. Due to the recent transformations mentioned above, the empirical formulations may no longer be representative of the mix designs used today and would require recalibration to involve limestone cement and non-conventional SCMs. Moreover, it was determined that the exponential fit is not capable of explaining the shape of hydration of more complex mix designs with slag or high amounts of fly ash (Riding et al., 2006).

Alternatively, semi-adiabatic calorimetry has conventionally been performed on-site to estimate the temperature rise and heat of hydration of concrete. The experiment involves monitoring the temperature rise of a well-insulated concrete mockup using embedded sensors. Semi-adiabatic calorimetry is a non-standardized test, and the results obtained can vary based on the procedure or the apparatus used. Though insulated, semi-adiabatic calorimetry allows heat losses from the hydrating concrete to the environment, which will need to be accounted for to find the adiabatic temperature rise and heat of hydration of the mix design. For this purpose, accurate information on insulation thermal

conductivity, concrete heat capacity, and concrete activation energy needs to be provided, or assumptions need to be made which will result in estimation errors (Wadsö, 2003). Moreover, a separate semi-adiabatic calorimetry experiment is needed for each mix design that requires evaluation, which can be a tedious task.

One of the contributions of Phase II of the project was to explore the use of robust isothermal calorimetry to find the heat of hydration of concrete and the adiabatic temperature rise. The methodology involves performing the isothermal calorimetry laboratory experiment in accordance with ASTM C1679 (ASTM International, 2017) at three or more different hydration temperatures, followed by data manipulation and analysis (Al-Hasani et al., 2022). Isothermal calorimetry is performed on small cementitious paste specimens instead of large concrete mockups and can handle eight different mix designs in one run. The resulting heat of hydration curves can also be used to recalibrate the exponential model to become more generalizable to relevant mix designs. The methodology was successfully used with high accuracy to find the heat of hydration of the mix designs proposed in Phase I and to supplement other tool submittals such as nomograms (Brown et al., 2023; Park et al., 2024) and a machine learning driven approach (Al-Hasani et al., 2023).

Phase II Mix Designs and Evaluation Results

The following five representative mixture designs were evaluated using isothermal calorimetry tests and validated through field simulations and experiments:

1. Baseline Mix: Traditional mix using Type I/II Portland Cement.
2. 25% Fly Ash (FA): Partial replacement of cement with 25% Class F fly ash.
3. 45% Fly Ash (FA): Higher replacement level to further suppress heat generation.

4. 25% FA + 20% BFS: Dual SCM mix combining fly ash and slag.

5. Coarse Cement: A low-heat cement option with reduced fineness.

These mixes were tested for both their thermal performance and strength development. Thermal behavior was characterized by maximum internal temperatures and temperature differentials under simulated curing conditions. The 45% FA and coarse cement mixtures demonstrated the most favorable thermal properties, yielding the lowest maximum temperatures and minimal thermal gradients. However, the 45% FA mix showed slower strength gain, reaching the required 4,500 psi compressive strength at 56 days instead of 28. All other mixes achieved this threshold within the 28-day benchmark.

Motivation for Phase III: Industry Shifts and Research Gaps

Building on these insights, Phase III expands the scope by incorporating additional SCM combinations as well as mix variants designed for broader climatic and placement conditions. It includes the evaluation of emerging low-carbon binders and the integration of Bayesian surrogate models to predict maximum temperatures more robustly across a range of geometries and boundary conditions. This approach not only broadens the applicability of the guidelines developed in Phase II but also enhances confidence in selecting mass concrete mixes that ensure thermal performance and structural integrity without unnecessary reliance on costly cooling systems.

After the conclusion of earlier phases of this project, some challenges had been identified that concern concrete mix designs. A major challenge is the availability of low-carbon, low-heat SCMs for use in mass concrete mix designs. A second one is the switch in the industry from Portland cement to Portland Limestone Cement. These factors partially triggered the need for Phase III, on a materials scale, to explore alternative low-heat, low-carbon mix designs, which are more relevant to the current orientation of the construction

industry, and to characterize their heat of hydration using the methods proposed in previous phases.

INVESTIGATING NEW CEMENT AND SCM COMBINATIONS

The exploration of alternative low-heat, low-carbon mix designs is essential for mass concrete. The proposed mix designs in Phase I included the incorporation of conventional SCMs (fly ash and slag), or the use of specialty coarse cement that has low heat of hydration. Whereas the proposed mix designs in Phase I were able to demonstrate an improved thermal behavior with lower maximum temperatures and temperature differences, the use of these mix designs is becoming more difficult due to limited availability. Fly ash sources are being depleted due to the closure of coal power plants globally as a step towards sustainable development (Diaz-Loya et al., 2019), and the available quantities of slag are currently depleted, for the most part, by the construction industry. Additionally, relying on specialty cements (such as the coarse cement used in Phases I and II) can be costly and impractical.

Secondly, the construction industry is rapidly switching from the use of Portland cement to Portland Limestone Cement (Cooper M, n.d.). This is an essential step to further the net-zero goal of the construction industry, since the use of limestone cement incurs around a 10% reduction in GHG emissions (*Sustainable Construction for a Circular Economy. In: Cement Association of Canada*, 2025). The mix designs proposed in Phase I of the project mainly incorporated type I/II Portland cement, which may no longer be representative of the mix designs used in mass concrete applications and the industry as a whole.

Mix Type Selection

The mix designs proposed for this phase of the project involve the incorporation of low-heat SCMs in combination with Portland Limestone Cement to explore their thermal behavior. As mentioned above, the supply of concrete-grade fly ash does not meet current demand due to factors related to the operation or closure of coal-fired power plants. So far, the construction industry has been selective with the quality of fly ash used in construction. Fly ash that has been stored in landfills or ponds does not satisfy the ASTM C618 standard (Diaz-Loya et al., 2019). This fly ash, known as reclaimed fly ash, can now be reclaimed and beneficiated for use in the concrete industry. Partial replacement of Portland Limestone Cement with reclaimed fly ash needs to be characterized for use in mass concrete and is the focus of this investigation.

The first mix is a reference mix that contains 100% Portland Limestone Cement in compliance with ASTM C595 (Standard Specification for Blended Hydraulic Cements, 2025). Two mixes have been selected to contain reclaimed fly ash with 20% and 40% replacement ratios. Similarly, two additional mixes containing ASTM C618-compliant Class F fly ash (Standard Specification for Coal Fly Ash and Raw or Calcined Natural Pozzolan for Use in Concrete, 2025) with 20% and 40% replacement ratios have been studied to better understand the behavior of reclaimed fly ash and how it compares to Class F fly ash.

LABORATORY TESTS TO ASSESS THERMAL PROPERTIES

To evaluate the thermal behavior of emerging cement and SCM combinations, a series of laboratory experiments were conducted focusing on three key performance indicators: heat of hydration, compressive strength development, and real-life mass concrete scenario simulation through semi-adiabatic calorimetry. These tests were selected to follow the

methodologies and standards established in Phase II of this research, with added emphasis on the new material of reclaimed fly ash.

Emerging cement, also known as ASTM C595 Type IL Portland Limestone Cement (PLC), was used in this task. The type IL cement was sourced from Buzzi Unicem USA, located in Chattanooga, TN. With the future decline of fly ash, ASTM C618 reclaimed Class F fly ash, also known as harvested coal ash, is increasingly in demand as it is known for its potential as a substitute for fly ash. The reclaimed fly ash was sourced from Eco Material Technologies, located in Taylorsville, GA.

With the type IL cement, reclaimed fly ash, and other SCMs, eight distinct cementitious paste compositions were tested. These mixes were designed to explore the effects of different SCM types and replacement ratios on hydration behavior. Table 1 provides a summary of the mix compositions used in the initial phase of testing.

Isothermal Calorimetry

Isothermal calorimetry is used to measure heat of hydration curves of the different cementitious pastes under constant temperature. The use of isothermal calorimetry to predict adiabatic temperature rise has been previously reported (Wadsö, 2003; Xu et al., 2015). Following the procedure outlined in Phase II (Cho et al., 2022), isothermal calorimetry was conducted at three discrete temperatures: 73.4 °F, 104 °F, and 140 °F (23 °C, 40 °C, and 60 °C, respectively).

Data from isothermal calorimetry can be used to convert from isothermal to either adiabatic or semi-adiabatic values. With the combination of cumulative heat evolved and corresponding temperature, a unique rate of heat release for concrete can be computed by mapping the relationship between experimental power (P), heat (H), and temperature (T) values and interpolating between them as necessary (Wadsö, 2003). Isothermal calorimetry

was performed in accordance with ASTM C1679 at different temperatures to find both the rate of heat release and corresponding cumulative heat curves (Cho et al., 2022). The effect of mixing action on the calorimetry results can be considered by using a high-shear mixer in accordance with ASTM C1738/C1738M-19 (ASTM International, 2019). After obtaining the heat of hydration curves for concrete, the finite difference (FD) or finite element (FE), thermal simulations can be supplemented with the heat of hydration curves to find internal temperatures in mass concrete elements. The FD or FE model can be provided with information regarding the geometry of the concrete volume (i.e., uniform and nonuniform), material properties (i.e., mechanical and thermal), thermal boundaries (e.g., insulation, formwork, ambient temperature), and cooling measures. Internal temperature development with time and at any point in space is then extracted as an output of the thermal modeling. This allows determining the values for maximum temperature and temperature differential, where they occur in the structure, and the time when they occur. At this point, modeling is conducted using the software "B4Cast," a finite element software that simulates temperatures and stresses in concrete structures during hardening (b4cast, 2025).

Eight distinct cementitious paste compositions were tested. These mixes were designed to explore the effects of different SCM types and replacement ratios on hydration behavior. Table 1 provides a summary of the mix compositions used in this phase of testing.

Table 1. Cementitious pastes used in isothermal calorimetry tests.

No.	Mix ID	Cement	Cement content	SCM	SCM content	w/s	Admixtures
1	IL100	Type IL	100	-	0	0.45	-
2	ILF20	Type IL	80	F ash	20	0.45	-
3	ILF40	Type IL	60	F ash	40	0.45	-
4	ILC40	Type IL	60	C ash	40	0.45	-
5	ILRF20	Type IL	80	Reclaimed F ash	20	0.45	-
6	ILRF40	Type IL	60	Reclaimed F ash	40	0.45	-
7	ILL10	Type IL	90	Limestone	10	0.45	-
8	ILS60	Type IL	40	Slag	60	0.45	-

Compressive Strength

Together with the isothermal calorimetry, compressive strength testing was conducted to ensure structural adequacy and compliance with GDOT requirements for mass concrete applications.

The following five mix designs were selected for strength testing:

- IL100: Type IL cement with no SCM replacement, serving as the baseline
- ILF20 / ILF40: Mixes containing 20% and 40% Class F fly ash, respectively, chosen to reflect current mass concrete practice
- ILRF20 / ILRF40: Mixes using reclaimed fly ash at 20% and 40% replacement levels, selected to evaluate how differently it performs compared with class F fly ash

The w/b ratios and the quantities of the high-range water-reducing admixture (PCHRWR) are summarized in Table 2. The coarse aggregate used in the concrete mix

designs was #67, in accordance with ASTM C33, in both the first and second mid-scale experiments, respectively, and both were granitic gneiss. Natural sand with a fineness modulus of 2.53 was used for fine aggregate.

Table 2. Concrete mix designs with selected pastes

		IL100	ILF40	ILRF40	ILF20	ILRF20
CEMENTITIOUS MATERIAL	OPC	0	0	0	0	0
	Type 1L cement	700	420	420	560	560
	Class F fly ash	0	280	0	140	0
	Rec fly ash	0	0	280	0	140
	Total binder	700	700	700	700	700
	water	315	315	315	315	315
	w/c ratio	0.45	0.45	0.45	0.45	0.45
AGGREGATE	#67	1685	1685	1685	1685	1685
	Natural Sand	1230	1230	1230	1230	1230
	Coarse/fine ratio	1.369919	1.369919	1.369919	1.369919	1.369919
ADMIXTURES	PCWR	13.755	13.755	13.755	13.755	13.755

Compression testing followed ASTM C39, and cylinders were tested at 7, 14, 28, and 56 days to capture both early-age and long-term strength development. Results indicate that all mixes meet the standard compressive strength of concrete class ‘D’, which is 4,000 psi by 28 days, as shown in Figure 1.

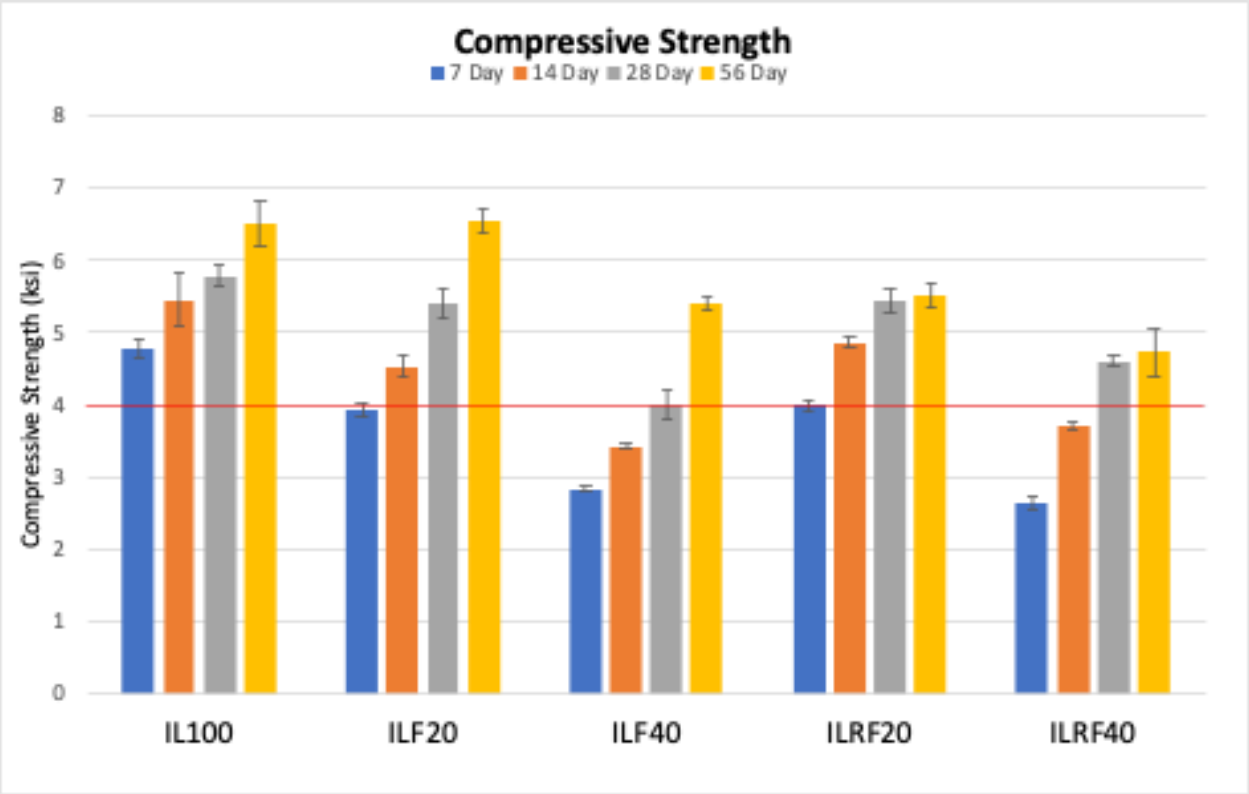

Figure 1. Compressive strength of concrete results

Semi-adiabatic Calorimetry

To validate the isothermal calorimetry predictions under more field-representative conditions, semi-adiabatic calorimetry tests were performed. These tests help simulate the thermal behavior of mass concrete by capturing temperature rise over time in a semi-insulated environment, mimicking real placement scenarios. Geokon low modulus strain sensors (Model 4200L) were used to capture temperatures as well as strains caused by differential temperatures. The accuracy of the sensors is ±0.5% full scale. Geokon temperature sensors (Model 3800) with an accuracy of ±0.5°C were used to assess the ‘‘ambient’’ temperature outside the formwork. Data collection was conducted at a 5-minute interval during the first 14 days, followed by a 15-minute interval for the remainder of the month.

Due to time and resource limitations, the following two representative mix designs

were selected: IL100 as a baseline mix with Type IL cement and ILRF40 with the 40% reclaimed fly ash, selected for its promising performance in earlier tests.

Each mix was cast into insulated containers embedded with sensors and placed in the ambient air conditioning with one other cylinder, as shown in Figure 2. The recorded temperature profiles were then compared to heat of hydration curves derived from isothermal data, allowing for calibration of heat generation curves in the models.

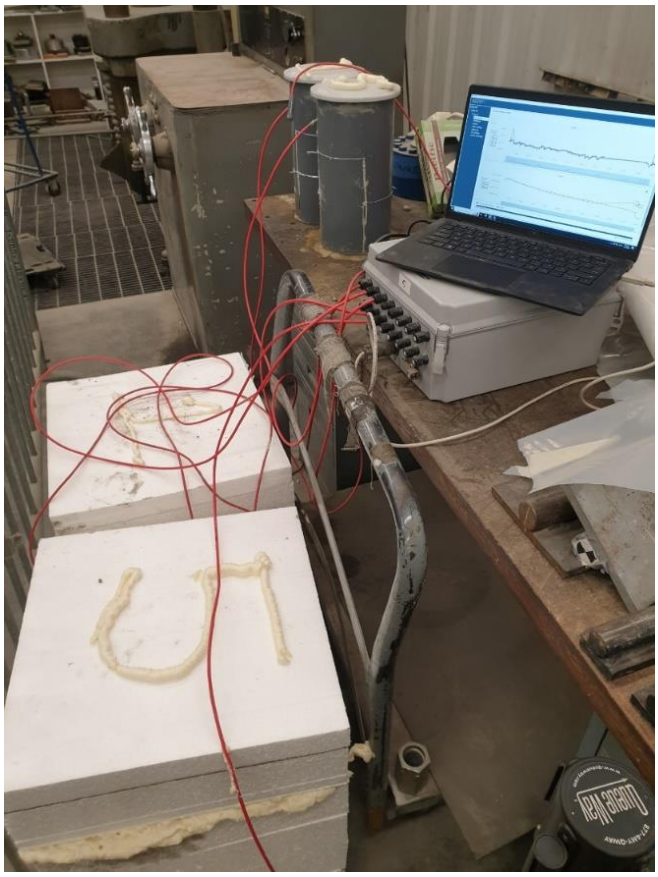

Figure 2. Semi-Adiabatic Calorimetry Experimental Setup

SUITABLE MIXTURE DESIGNS RECOMMENDATIONS

Each mix was cast into insulated containers embedded with sensors, and with one other cylinder placed in the ambient air conditioning, as shown in Figure 2. The recorded temperature profiles were then compared to heat of hydration curves derived from

isothermal data, allowing for calibration of heat generation curves in the models.

Based on the results of laboratory testing, several mixture designs have been identified as suitable candidates for application in mass concrete structures, particularly in scenarios where thermal control is an important consideration. These recommendations take into account, firstly, the heat of hydration—an essential factor in managing internal temperature rise—and secondly, the compressive strength performance required by GDOT specifications.

Mixtures incorporating Type IL cement with a high replacement ratio of supplementary cementitious materials (SCMs), both Class F fly ash and reclaimed fly ash, were among the lower side of the cumulative heat of hydration among all tested combinations. These blends consistently produced lower peak temperatures in both isothermal and semi-adiabatic calorimetry tests, reducing the possible temperature gradient in mass concrete.

Importantly, these mixtures also achieved compressive strengths exceeding the GDOT threshold of 4,000 psi at 28 days. Continued strength development up to 56 days indicates long-term durability, making high SCM Type IL mixes a viable and cost-effective solution for mass concrete applications.

Class F fly ash, a widely adopted SCM in Georgia and across the U.S., performed reliably when combined with Type IL cement. Mixtures with both 20% and 40% Class F fly ash substitution (ILF20 and ILF40) lowered the heat of hydration curve effectively, as shown in Figure 3. Given its well-understood behavior, established supply chains, and favorable pozzolanic properties, Class F fly ash remains a preferred choice for heat mitigation in mass concrete design.

Reclaimed fly ash, sourced from underground or buried under ponds, was evaluated

at 20% and 40% replacement levels (ILRF20 and ILRF40). The test results revealed performance characteristics closely aligned with those of Class F fly ash in both heat evolution and strength gain. Notably, the ILRF40 mix achieved higher compressive strength than the ILF40 mix, exceeing 4,000 psi at 28 days (see F 40% and Rec F 40% 0.45 in Figure 1). Together with its low cumulative heat output shown in Figure 4, this makes the ILRF40 a promising substitute where conventional fly ash availability is limited. Given growing supply constraints and sustainability goals, reclaimed fly ash may serve as an effective SCM option without introducing significant performance variability.

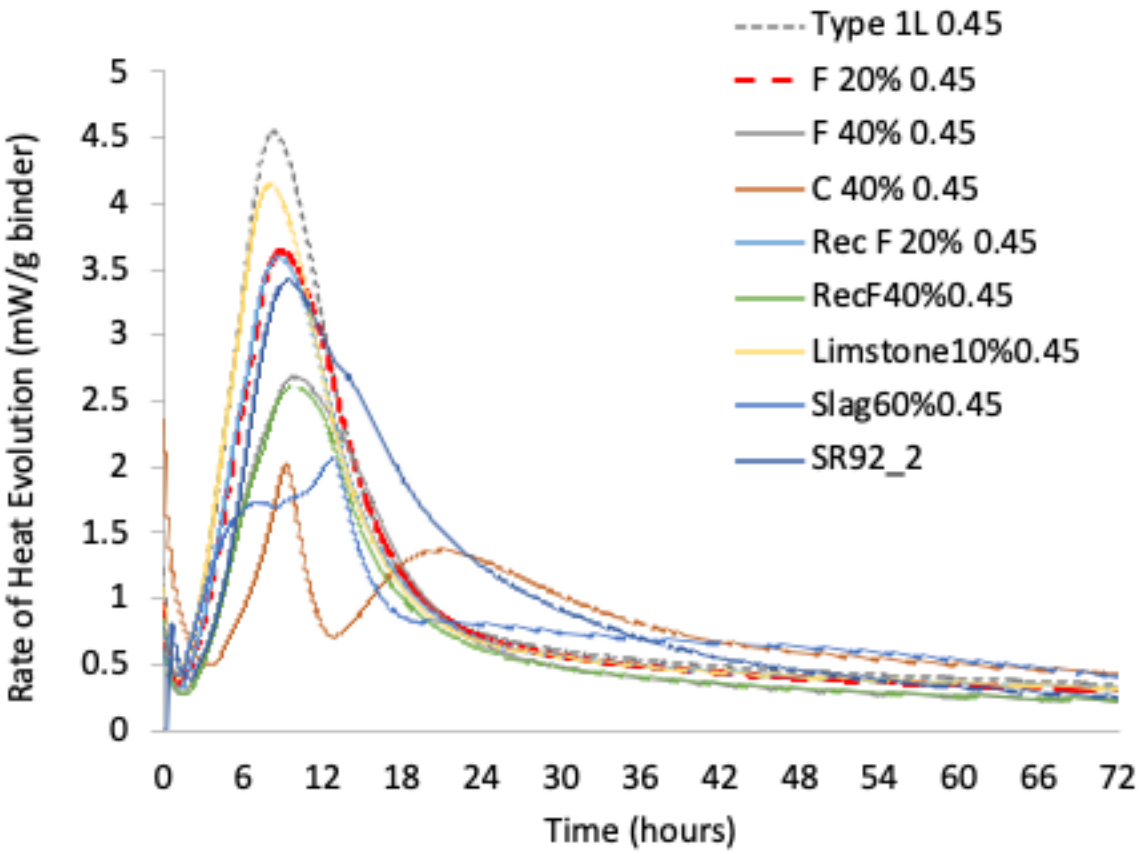

Figure 3. Rate of heat of hydration curve.

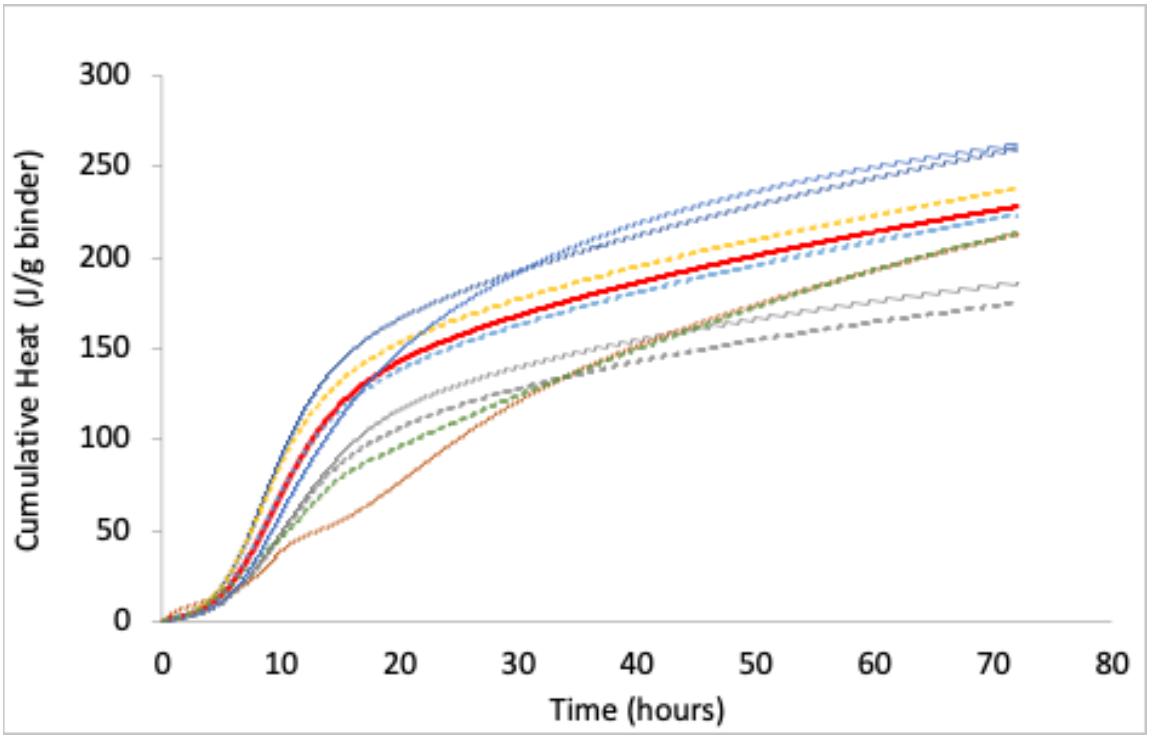

Figure 4. Cumulative heat of hydration curve.

CONCLUSION

The investigation of emerging cement and SCM combinations in Chapter 2 has demonstrated that incorporating Type IL cement and reclaimed fly ash as partial replacements for conventional cementitious materials can effectively reduce heat generation while maintaining adequate compressive strength for mass concrete applications. The laboratory tests, including isothermal calorimetry and semi-adiabatic calorimetry, confirmed that high SCM mixes, particularly those with 40% reclaimed fly ash (IL+RF40), achieved lower peak temperatures and temperature gradients without compromising structural integrity. These findings align with the Phase II results, which highlighted the thermal benefits of SCM-rich mixes but extend the applicability to more sustainable and readily available materials, addressing industry trends and material availability constraints. Overall, the proposed mix designs provide viable alternatives for

mass concrete projects, particularly in scenarios where thermal management is critical and fly ash supply is limited. Further validation through field-scale testing and monitoring is recommended to confirm these outcomes under real-world conditions and further refine the predictive models for thermal behavior in mass concrete structures.

CHAPTER 3. VALIDATION, EXTENSION, AND REFINEMENT OF NOMOGRAMS DEVELOPED FROM PHASE II (TASK 2)

The purpose of this task is to refine and better characterize simple models for estimating maximum temperatures in mass concrete, such as those developed in Phase II. The model used for the no-postcooling case in Phase II, while based on some physical reasoning, was nevertheless somewhat ad hoc. Here we propose another model with a firmer basis in physics. Furthermore, we characterize the uncertainty by extending this model into a Bayesian statistical model and then incorporating this uncertainty into a simple nomogram.

Creating simple models of complex phenomena, such as three-dimensional transient heat transfer involving complicated internal heat generation, requires understanding how the various parameters are interrelated. To investigate these relations, a fully analytic (closed-form) model of the no-postcooling case was derived using Green's functions; in contrast to the simple model, which only relates maximum temperature to the input parameters, this Green's function model is a fully three-dimensional transient model. This Green's function model reveals the difficulties in creating simple models that are capable of being depicted in nomograms. However, it has the advantage of being easily differentiated so that the temperature gradient can be computed directly from this Green's function model, despite requiring a computer implementation to be practicable. With this model implemented in computer code, maxima of temperature and temperature gradient can be found relatively easily using standard optimization routines and/or root-finding routines.

BAYESIAN STATISTICAL MODEL AND NOMOGRAM FOR NO-POSTCOOLING

Building on the work from Phase II, an improved statistical model for maximum temperatures in non-postcooled situations was developed. Consider that for mass concrete, the maximum temperature T_{max} is a small correction of the adiabatic temperature rise; this correction represents the energy loss due to the diathermal condition.

We based the model on a simple description of adiabatic temperature rise (SUZUKI et al., 1988), which uses the logistic function

$$f(t) = \left(1 - e^{-bt^c}\right)$$

to model the adiabatic temperature rise as

$$T_a(t) = T_i + \Delta T_a\left(1 - e^{-Gt^c}\right)$$

where T_i is the initial temperature, ΔT_a is the adiabatic temperature rise, G is a 'gain factor' to be regressed from isothermal calorimetry data when available, and c is a free parameter to be chosen later.

Consider that the temperature history during hydration is represented by the adiabatic temperature rise minus a corrective temperature 'loss' modeled by the same type of logistic function. Simulation data suggests this is a good approximation. Take this loss of temperature to be

$$T_L(t) = \Delta T_a\left(1 - e^{-Lt^d}\right)$$

where L is a 'loss factor' analogous to the gain factor G. Then the temperature is modeled as an adiabatic rise above the initial temperature, corrected by a temperature loss.

$$\begin{aligned} T(t) &= T_i + T_a(t) - T_L(t) \\ &= T_i + \Delta T_a\left(1 - e^{-Gt^c}\right) - \Delta T_a\left(1 - e^{-Lt^d}\right) \\ &= T_i + \Delta T_a\left(-e^{-Gt^c} + e^{-Lt^d}\right) \end{aligned}$$

We refer to this model, and derivatives of it, as "Suzuki" models in what follows;

we also refer to it as a "surrogate" model for reasons to be given later. In fitting these models with some finite-element simulations, it turns out that the fits do not generally yield solutions where the exponents c and d are equal. However, when this is constrained to be the case, e.g. $c = d = 2$, the resulting fits and errors between finite-element simulations and fitted Suzuki models are often below 5%.

The maximum temperature T_{max} occurs at a time t_m, say, which the Suzuki model would place at t such that

$$\frac{\partial T}{\partial t} = 0 = \frac{Gct^c e^{-Gt^c}}{t} - \frac{Ldt^d e^{-Lt^d}}{t}$$

Assuming $c = d$, then, t_m would be given by

$$t_m = \sqrt[c]{\frac{ln(G/L)}{G - L}}$$

then

$$T_{max} = T_i + \Delta T_a \left(-e^{-G\frac{ln(G/L)}{G-L}} + e^{-L\frac{ln(G/L)}{G-L}} \right)$$

With (diathermal) finite-element data already computed, we can compute G and L. However, doing this is inappropriate, as G and L are likely under constraint. G refers to a strictly adiabatic hydration curve. Comparing G fitted using data in which T_{max} is found using a diathermal simulation (as in the Python code above and the two equations immediately preceding it) to G fitted using adiabatic timeseries and shows percent errors between 16% and 64%; here we take G from adiabatic timeseries as the true value.

It was also noticed that G, fitted using data in which T_{max} is found using a non-adiabatic simulation, varied with size. This should not be the case, since adiabatic conditions render size irrelevant. This suggests that finding G and L using only the summary non-adiabatic simulation data conflates gains and losses.

To determine G, we run many adiabatic simulations, then compute G for each one using $T_a(t) = T_i + \Delta T_a\left(1 - e^{-Gt^c}\right)$

Then, using this set of "true" values for G, fit a model so that G_{fitted} can be computed; possible model for G_{fitted}:

$$G_{fitted} = u_0 e^{u_1 \frac{Ea}{R}\left(\frac{1}{T_r} - \frac{1}{T_i}\right)}$$

where u_0 and u_1 are coefficients to be determined by regression, and

- E_a: apparent activation energy
- R: universal gas constant
- T_r: reference temperature in Kelvin or degrees Rankine
- T_i: initial temperature in Kelvin or degrees Rankine

Then, using this fitted G, we can compute L using the (diathermal) finite element data.

Using this computed L and visualizing it against various parameters, a combination of slope-intercept models was proposed for L_{fitted}:

$$\begin{aligned} ln\left(\frac{1}{L_{fitted}}\right) &= m\frac{Ea}{RT_i} + b \\ &= m\frac{Ea}{RT_i} + (m_1 \cdot \Delta T_a + b_1) + \left(m_2 \cdot \frac{V}{qA} + b_2\right) + (m_3 \cdot ln(X) + b_3) \\ &\quad + (m_4 \cdot T_{amb} + b_4) + (m_5 \cdot \alpha + b_5) \\ &= m\frac{Ea}{RT_i} + m_1 \Delta T_a + m_2 \frac{V}{qA} + m_3 ln(X) + m_4 T_{amb} + m_5 \alpha + \Sigma b_* \end{aligned}$$

where

$$\Sigma b_* = b_1 + b_2 + b_3 + b_4 + b_5$$

Note that here the temperature T_i is in an absolute scale (i.e. either Kelvin or Rankine); for convenience, T_{amb} is in degrees Celsius or Fahrenheit. The other variables are as follows:

- V/qA: ratio of concrete volume to the surface area that participates in heat transfer; in this work, we assume the bottom surface is adiabatic, so qA does not include this bottom surface area. Units are meters or feet.
- X is the area-averaged U-value if SI units are used or the area-averaged R-value if USCS units are used; in both cases, the U-value or R-value includes the convection coefficient as well as any insulating blankets.
- $\alpha = \kappa/\rho c$ is the thermal diffusivity of the concrete.

With this, we can then calculate T_{max} with

$$T_{max} = T_i + \Delta T_a \left(-e^{-G\frac{ln(G/L)}{G-L}} + e^{-L\frac{ln(G/L)}{G-L}} \right)$$

Where we have dropped the $fitted$ subscripts from here on. We will sometimes refer to this as a surrogate model for maximum temperature as it encapsulates finite element simulations and is therefore only a representative of the underlying physics.

BASIC MODEL RESULTS

Values of the parameters for G and L were regressed on results from 896 finite-element simulations using calorimetry and associated concrete mix designs from Phases II and III, and span a range of initial temperatures, lengths, widths, heights, ambient temperatures, as well as formwork and thermal blanket types; simulations were conducted using the FEniCS package (Alnæs et al., 2015).

USCS units

In USCS units, it's convenient to express insulation as R-value (in USCS units, of course), then

$$ln\left(\frac{1}{L}\right) = m\frac{Ea}{RT_i} + m_1\Delta T_a + m_2\frac{V}{qA} + m_3 ln(R) + m_4 T_{amb} + \Sigma b_{**}$$

With $V/qA \geq 1$ ft ≈ 0.4 m and $T_i \geq 10°C = 50°F$, we get the following:

Parameters of the model for G:

- u0: 0.0029454
- u1: 1.9508283

Parameters of the model for L:

- m: 1.2988582
- m1: -0.0087839
- m2: 1.1824905
- m3: 0.2103447
- m4: 0.0103032
- m5: 1210035.8558403
- Sum_b_*: -19.7783795

Results can be seen in Figure 5 and Figure 6.

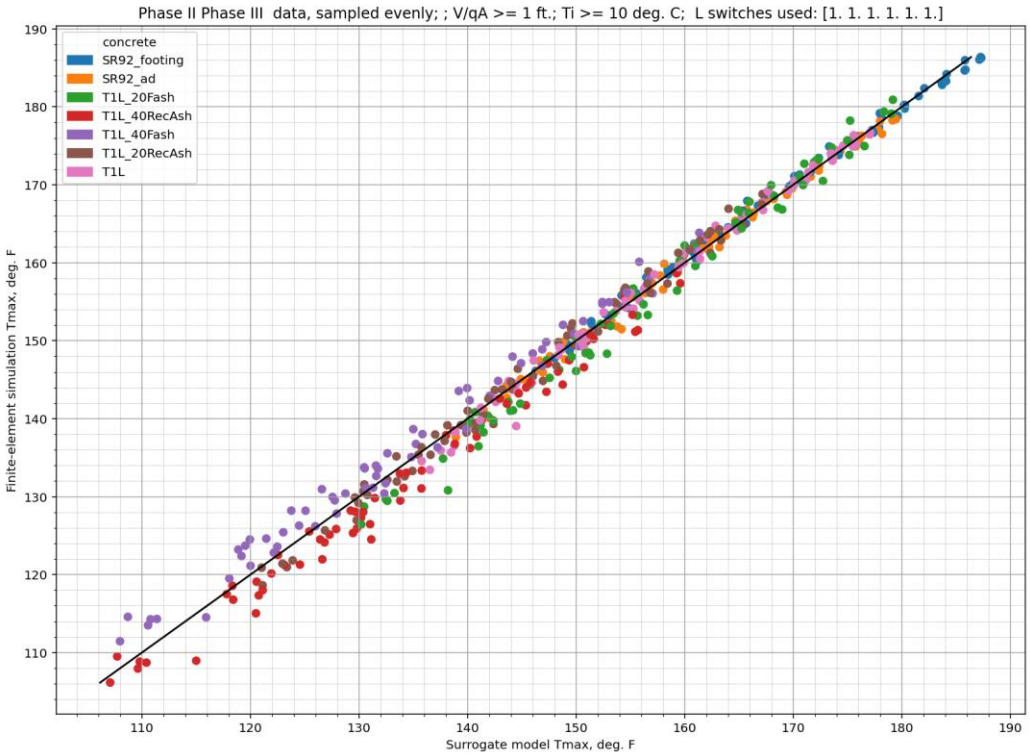

Figure 5. Basic model results sampled from Phase II and Phase III data, shown for cases with $V/qA \geq 1$ ft ≈ 0.4 m and $T_i \geq 10^{\circ}C = 50^{\circ}F$.

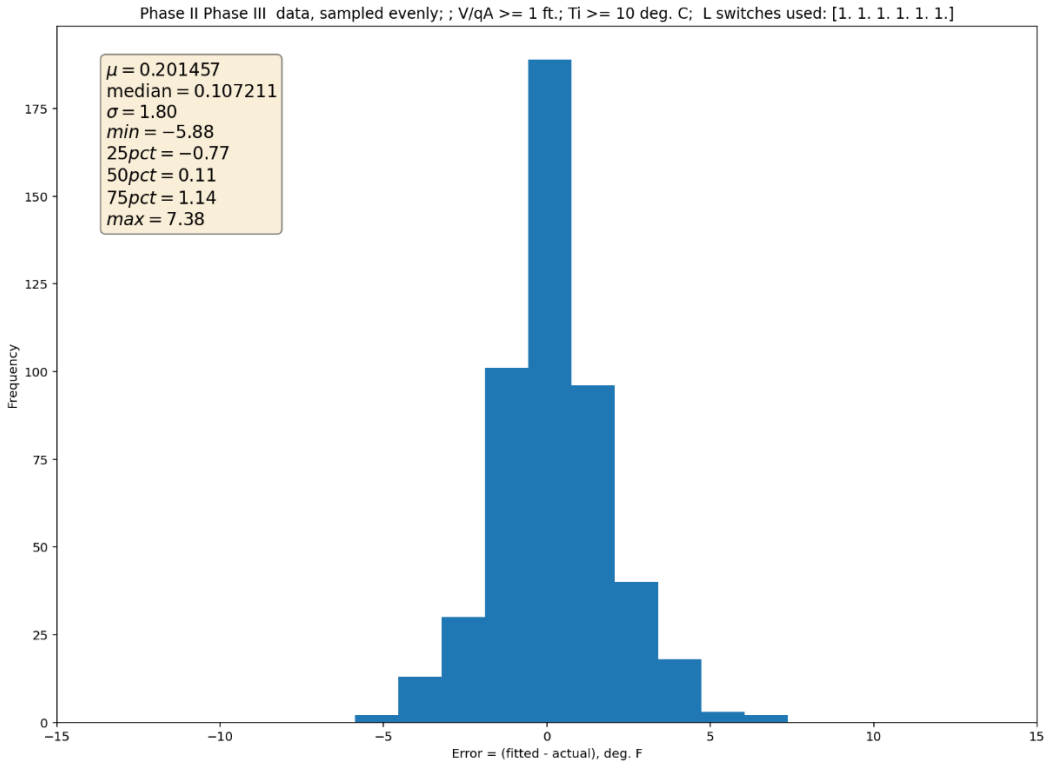

Figure 6. Histogram of prediction errors for the basic model under the same conditions as Figure 5.

With V/qA<1:

Parameters of the model for G

- u0: 0.0029454
- u1: 1.9508283

Parameters of the model for L

- m: 1.1365250
- m1: -0.0123765
- m2: 2.0641601
- m3: 0.3624182
- m4: 0.0173536
- m5: 730541.2779642
- Sum_b_*: -15.0785718

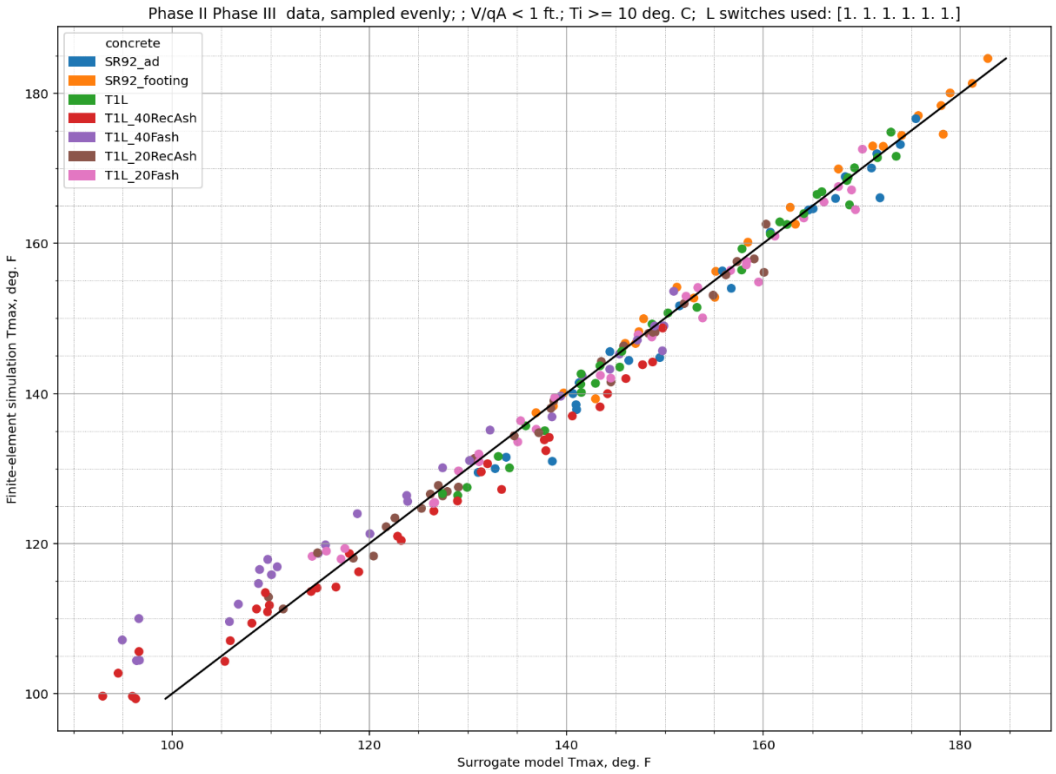

Figure 7. Basic model results sampled from Phase II and Phase III data, shown for cases with V/qA<1.

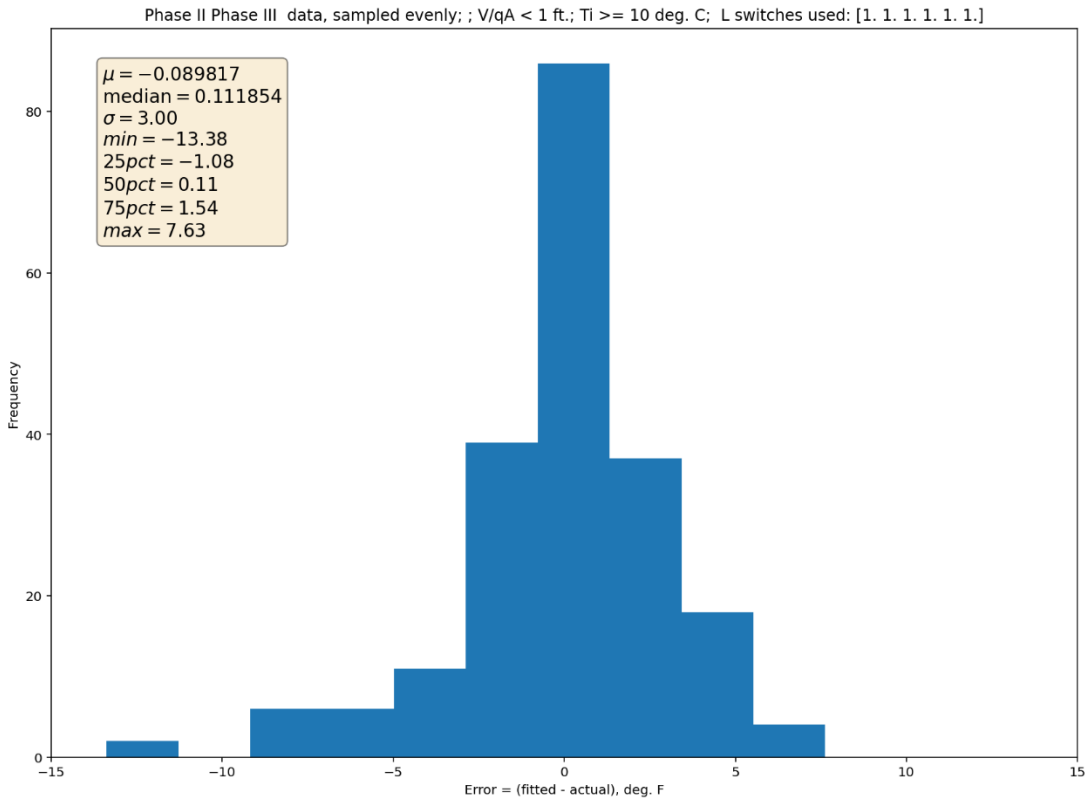

Figure 8. Histogram of prediction errors for the basic model under the same conditions as Figure 7.

BAYESIAN MODEL

To assess uncertainty, we take this basic model for T_{max} and wrap it in a probabilistic framework to form a Bayesian model (McElreath, 2018). The output of this model, besides an estimate of the uncertainty in the calculation of T_{max} is another estimate of the parameters in the equations for G and L (along with a few other parameters needed to define probability distributions used in this Bayesian model).

First, we assume that the surrogate model values for T_{max} follows a modified PERT distribution, chosen because this is a distribution with nonzero probability values only in a particular window (i.e., it is supported on a bounded interval, meaning the tails of the distribution do not go to $\pm\infty$); this accords with the assumption that the maximum concrete

temperature will not be greater than the initial temperature plus the adiabatic temperature rise. The minimum value of this distribution is assumed to be a fraction of the adiabatic temperature; the value of this fraction is determined as part of the statistical analysis. The remaining parameter of this distribution, a shape factor, is likewise determined during the analysis. The u_*, m_*, and b_* parameters of the models for G and L are assumed to follow uniform distributions whose limits are estimated based on the simple regressions in the previous section.

$$
\begin{aligned}
T_{max} &\sim pertm(T_{minmax_i}, T_{modemax_i}, T_{maxmax_i}, \lambda_i) \\
T_{maxmax_i} &= T_{i,i} + \Delta T_{a,i} \\
T_{minmax_i} &= T_{i,i} + \epsilon \Delta T_{a,i} \\
T_{modemax} &= T_i + \Delta T_a \left(-e^{-G\frac{ln(G/L)}{G-L}} + e^{-L\frac{ln(G/L)}{G-L}} \right) \\
G &= u_0 e^{u_1 \frac{Ea}{R}\left(\frac{1}{T_r} - \frac{1}{T_i}\right)} \\
ln\left(\frac{1}{L}\right) &= m\frac{Ea}{RT_i} + m_1 \Delta T_a + m_2 \frac{V}{qA} + m_3 ln(X) + m_4 T_{amb} + m_5 \alpha + \Sigma b_{**} \\
u_{*,i} &\sim uniform(u_{*,min}, u_{*,max}) \\
m_{*,i} &\sim uniform(m_{*,min}, m_{*,max}) \\
\Sigma b_{**,i} &\sim uniform(\Sigma b_{**,min}, \Sigma b_{**,max}) \\
\lambda_i &\sim uniform(\lambda_{i,min}, \lambda_{i,max})
\end{aligned}
$$

where, as before, X is the U-value if SI units are used or the R-value if USCS units are used.

The input data for the analysis is 493 finite-element simulations spanning the parameter space (Phase II and III calorimetry and concrete mix designs, initial temperatures, ambient temperatures, concrete emplacement sizes, thermal blankets, convection coefficients, etc.). This data is partitioned into training and testing data. The training data is then used by the Python library PyMC (Abril-Pla et al., 2023) to regress the model above using Markov chain Monte Carlo methods.

This analysis produces not single point estimates for the parameters u_* and m_* for G and L respectively, but distributions (in this case, uniform distributions) over the range

of values that these parameters may take. In this case, parameters in USCS units are estimated as shown below:

Table 3. Summary statistics for parameter distributions in the Bayesian model.

	mean	*std. dev.*	*hdi_3%*	*hdi_97%*
u0	0.0029297	0.000084	0.0027988	0.0030682
u1	2.1019825	0.07509	1.967747	2.2459187
m	1.3072829	0.008514	1.2904291	1.3219337
m1	-0.0087625	0.000209	-0.0090855	-0.0084307
m2	1.1878523	0.013363	1.1642203	1.2060408
m3	0.211148	0.002344	0.2071355	0.2145593
m4	0.0103047	0.000058	0.0102099	0.0103983
m5	1207770.52	6828.89172	1197671.74	1219219.41
*Sum_b_**	-19.85562	0.096326	-19.973656	-19.666466

The mean values compare well to the point estimates found by simple regression earlier. In particular, the standard deviation is at least one order of magnitude smaller than the mean value and is often several orders of magnitude smaller.

The mean values of these model parameters are then used to calculate maximum temperatures for the initial and boundary conditions of the testing data. Comparisons of these surrogate model T_{max} values are compared to the corresponding finite-element values; in the figure below, 89% of predictions fall in the orange shaded area.

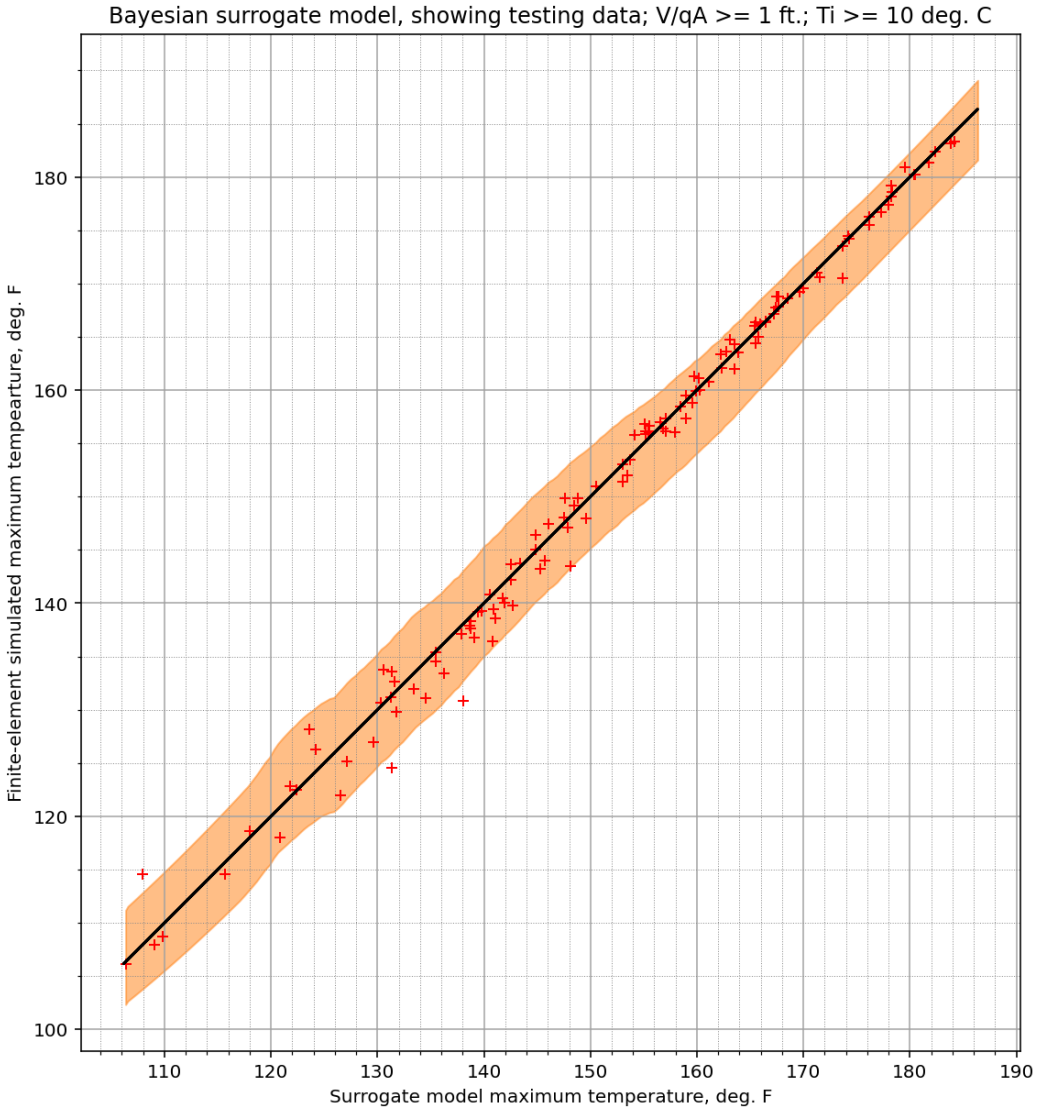

Figure 9. Bayesian surrogate model results, showing testing data where V/qA >=1.

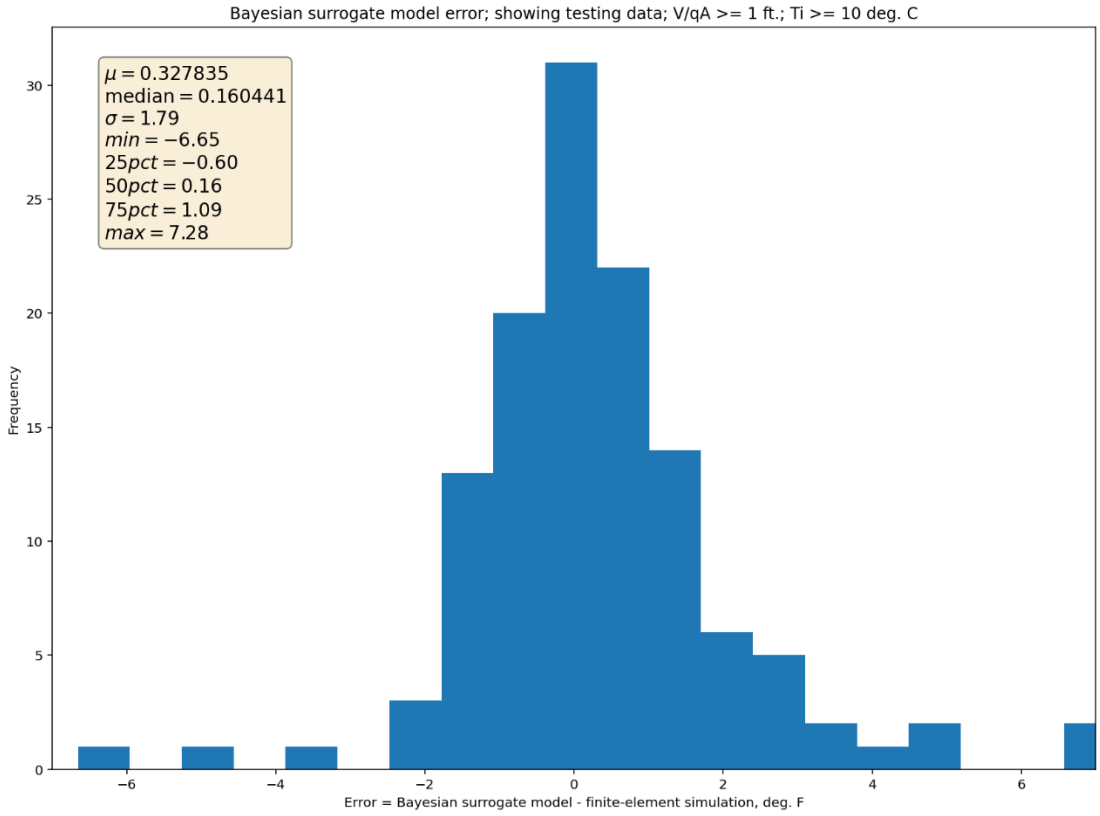

Figure 10. Histogram of prediction errors from the Bayesian surrogate model.

NOMOGRAM OF THE NO-POSTCOOLING SURROGATE MODEL

A nomogram of the surrogate model was constructed using the Python package Pynomo (Abril-Pla et al., 2023), taking into account that the the standard deviation of the errors in T_{max}, using the mean values of u_*, m_*, and Σb_*, is 1.79 °F. Specifically, we take twice this standard deviation to be the "half width" of the uncertainty band; i.e. we construct the nomogram to depict a lower bound for maximum temperature to be $T_{max} - 2(1.79)$°F and an upper bound to be $T_{max} + 2(1.79)$°F. The nomogram is presented below.

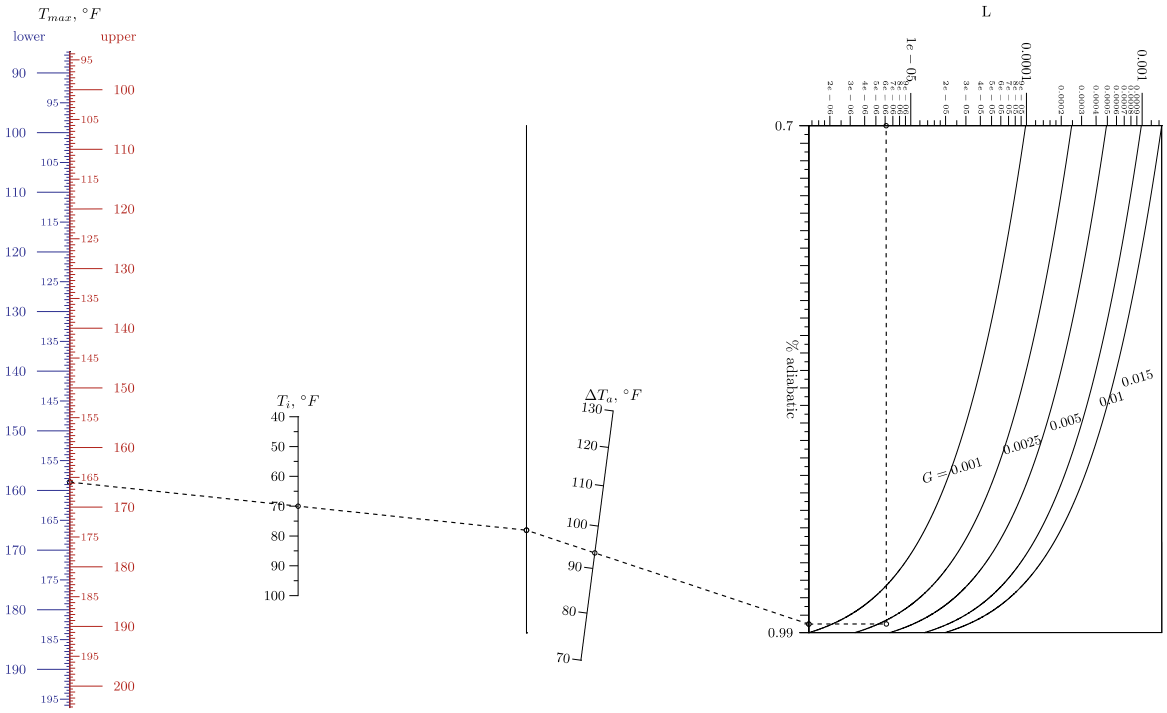

Figure 11. Nomogram of the Bayesian surrogate model.

The dashed line represents a calculation for the SR92 wall. The finite-element simulated maximum temperature for this project (i.e., if it had not been postcooled) as 161 °F, which is within the uncertainty band of this model.

While this nomogram is simple, it hides several complexities. It does not allow computation of G and L; expanding the nomogram to do this would make it complex. Additionally, the initial temperature T_i shows up explicitly in one axis; however, it is also embedded in the equations for G and L. If the nomogram were to be expanded to include a calculation of G and L, one would need to ensure the same value of initial temperatures was used consistently in three separate places, increasing the chances for error.

To explore the issue of the initial temperature showing up in several different places of the surrogate model, and to possibly replace them, further analytic models for temperature were derived. The analytic models developed here are closed-form solutions

of the heat diffusion equation with an energy generation term; this is discussed in the next section.

GREEN'S FUNCTION SOLUTION TO 3D THERMAL CONCRETE HYDRATION PROBLEM

Analytic solutions of the transient 3D heat diffusion equation with a generation term (labeled $\dot{e}_{gen}$ here) modeling cement hydration can be difficult to find, but the task is made tractable by representing cement hydration based on the "Suzuki" temperature rise model of the previous sections:

$$\dot{e}_{gen} = 2\rho c \Delta T_a G t e^{-Gt^2}$$

There are a variety of techniques to solve the heat diffusion equation. The technique used here is based on Green's function solutions (Cole et al., 2010). The derivation and the complete model are given in the appendix; what follows is a brief description of the result.

The temperature of hydrating concrete is the sum of three components: one arising from the boundary conditions (T_{bc}), one from the hydration of concrete (T_{egen}), and the initial temperature (T_i):

$$T(x, y, z, t) = T_{bc}(x, y, z, t) + T_{egen}(x, y, z, t) + T_i$$

The equations for T_{bc} and T_{egen} are complex and can be found, along with their derivation, in the appendix. These equations contain nested series terms, and practical calculations are done on a computer. Nevertheless, they are fully closed-form and provide results that compare quite well to finite-element solutions. An example can be seen in Figure 12.

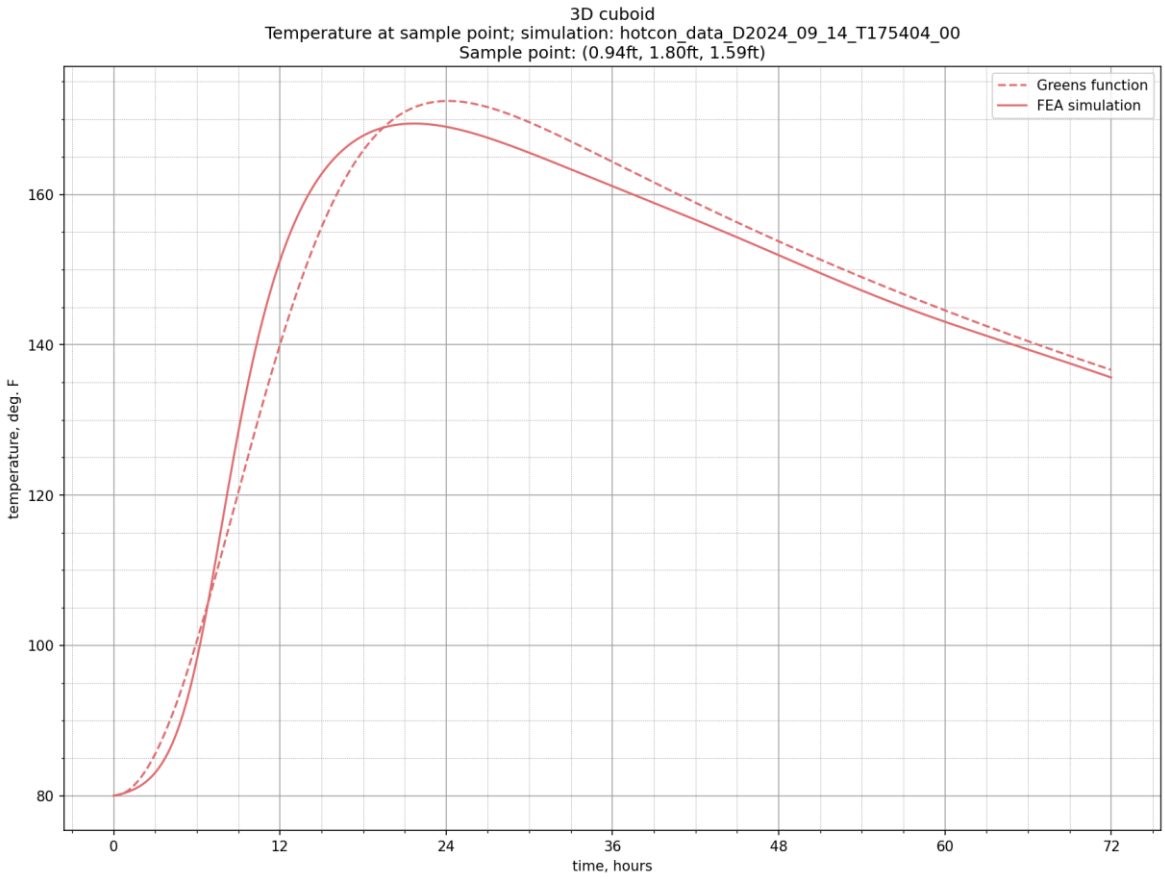

Figure 12. Temperature profiles from Green's function and finite element analysis (FEA) simulations at the same locations.

Inspection of these equations (see the Appendix) reveals that, like the surrogate model above, parameters (and variables) show up in several terms of the equations and in various combinations. This precludes them from being separable and independent, and reveals that a reduction in the dimensionality of the problem is unlikely.

Nevertheless, these equations provide an alternative to finite-element simulations. A particular advantage is that optimization routines may be used to determine the maximum temperature efficiently, without having to calculate temperatures at all locations and times. For example, the following figure depicts a comparison between 527 maximum temperatures calculated by finite-element simulations and maximum temperatures found

using the Green's function model, using concrete mix designs from Phases II and III:

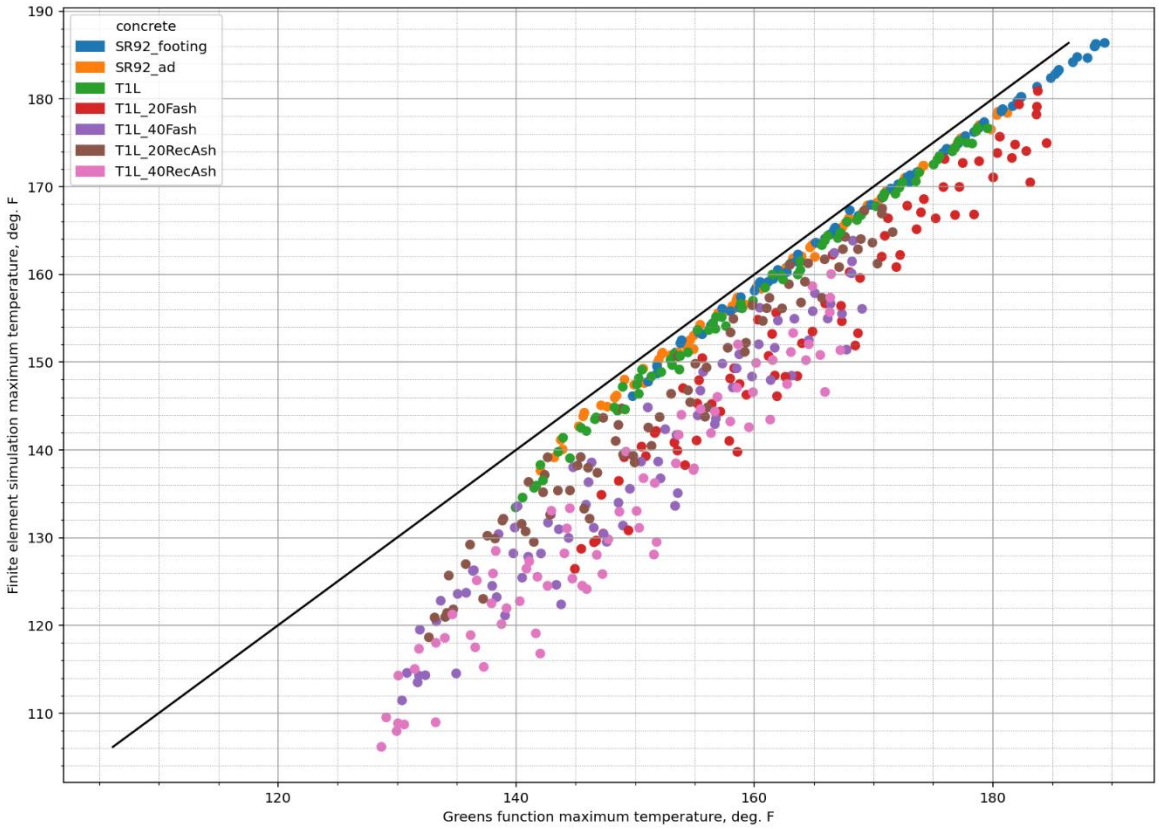

Figure 13. Comparison of maximum temperatures predicted by the Green's function model and FEA simulations using concrete mix designs from Phase II and Phase III.

In the current form, maximum temperatures are overpredicted by the Green's function model. For mix designs that do not contain fly ash, results of Green's function model correspond well to finite-element simulations.

The computation of maximum temperatures for these 527 cases took 59 seconds using the closed-form solution and optimization techniques. The time to compute these maxima using finite-element simulations ranged from hours to days, to investigate if the factor G was estimated separately for non-fly as mixes and for mixes containing fly ash. Using G fitted only to mixes without fly ash is represented in the following figure:

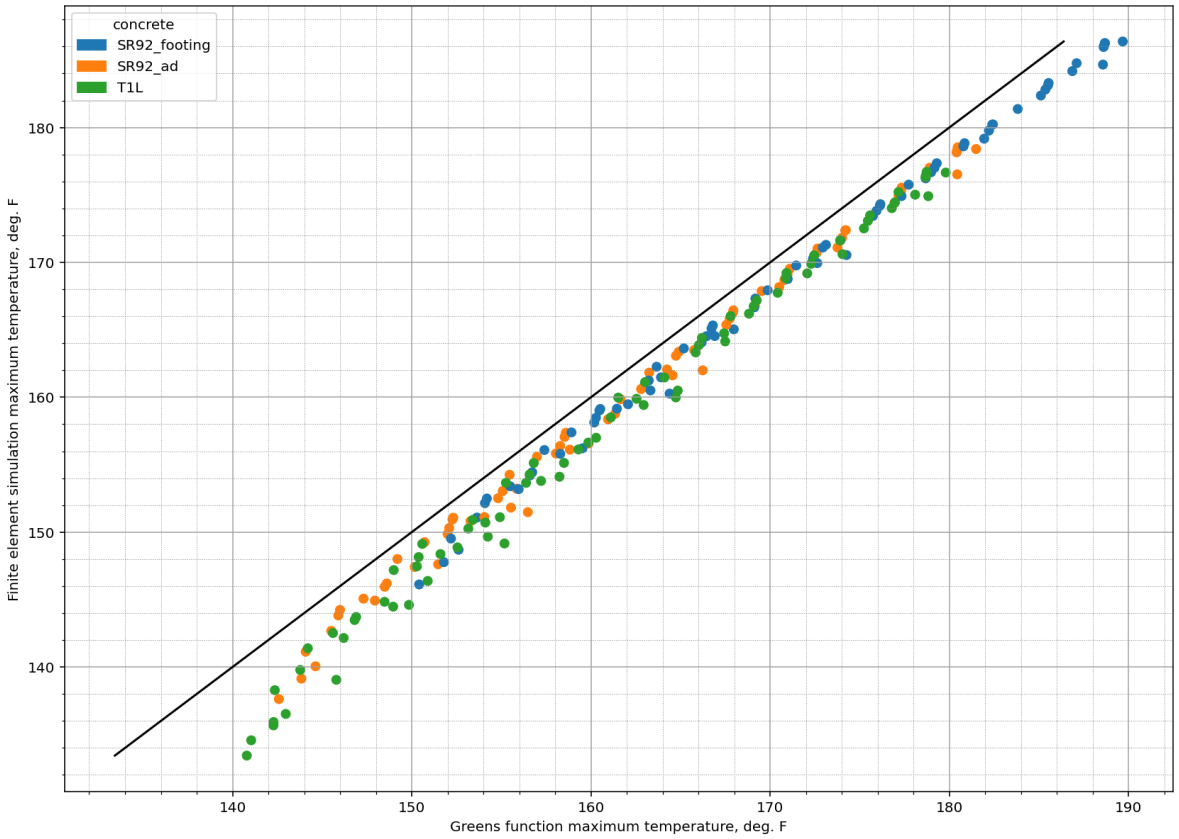

Figure 14. Green's function and FEA simulation results using the parameter G estimated separately for non-fly ash mixes and for mixes containing fly ash.

In Figure 14, the Green's function model overpredicts finite-element simulation maximum temperatures by roughly 2°F. Using G fitted only to mixes with fly ash is represented in the following figure:

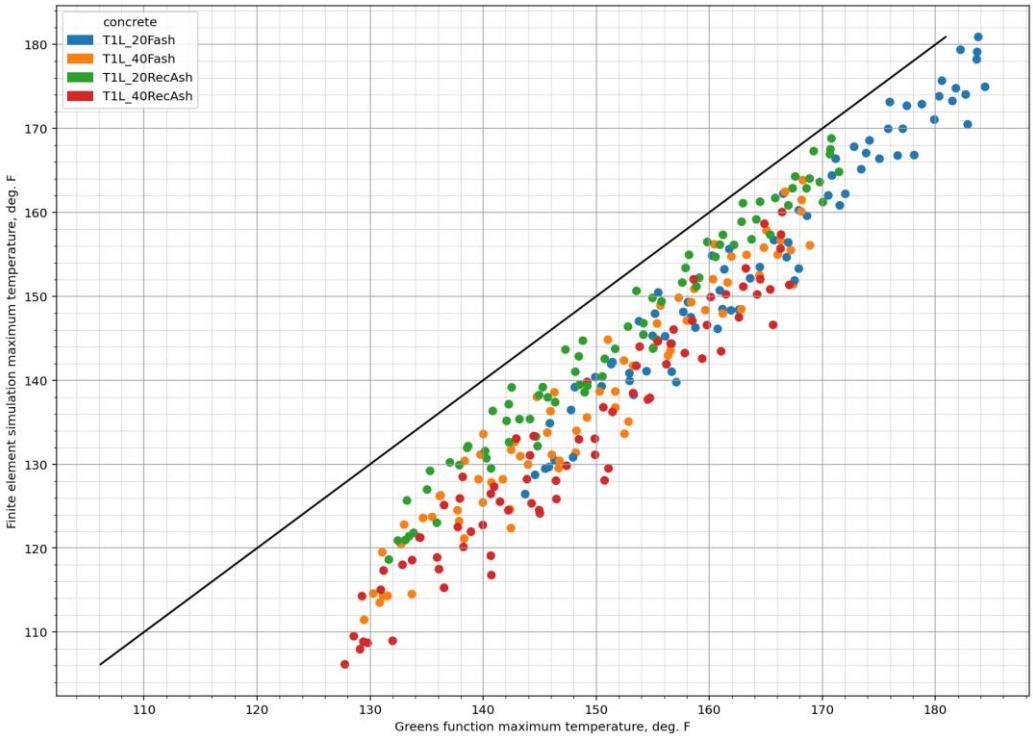

Figure 15.Green's function and FEA simulation comparison showing that the Green's function model overpredicts maximum temperature by approximately 2 °F.

As before, the Green's function model yields greater overpredictions—on the order of 10 °F—for mixes with fly ash than for mixes without fly ash.

A further advantage of these closed-form equations is that the gradient may be taken analytically to give a closed-form solution of the temperature gradient. Details are given in the appendix, and only an example result is given below:

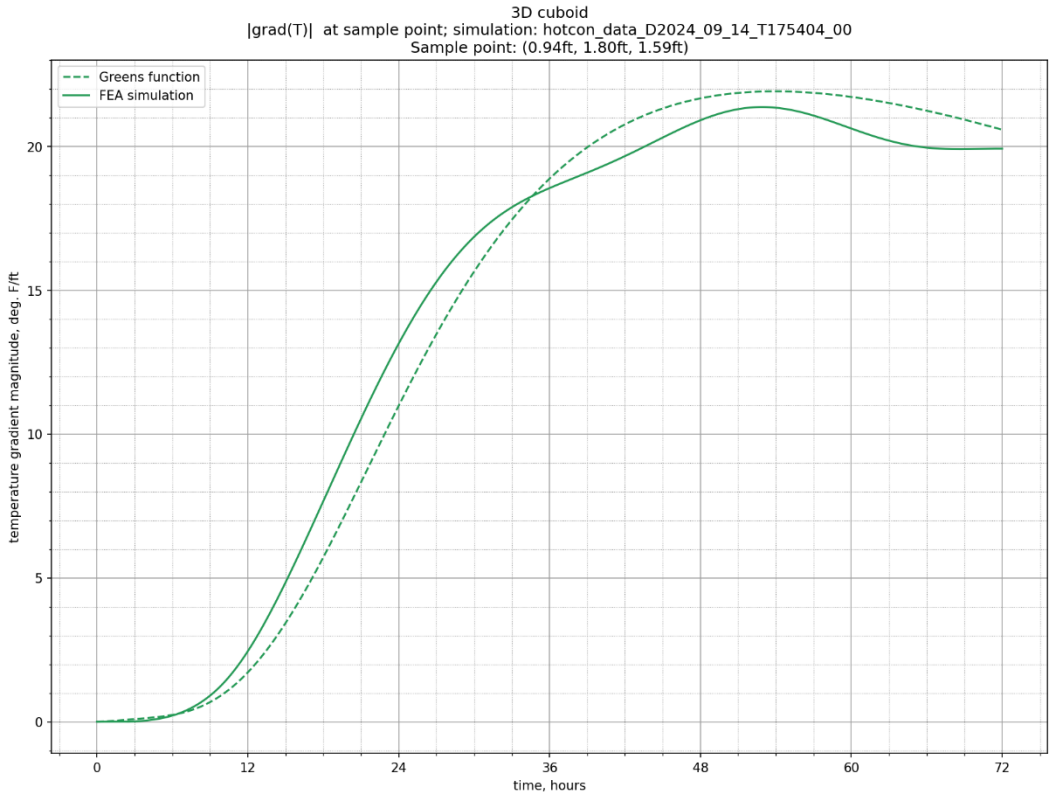

Figure 16. Example illustrating how closed-form equations allow analytical calculation of the temperature gradient.

In both of these closed-form models, the primary source of uncertainty rests in knowing the value of the parameter G.

CONCLUSION

The following two new analytical, closed-form models for concrete hydration in the no-postcooling case have been developed:

1. A statistical surrogate model of fairly simple form
2. A more complex exact solution using Green's functions and the hydration model used in the surrogate model

The uncertainty in the surrogate model was quantified using Bayesian techniques. This uncertainty was incorporated into a basic nomogram that visually represents the

overall features of this model, but due to the structure of the model, this nomogram cannot fully represent the model in a convenient form. However, this model may nevertheless be useful as it is simple enough for hand calculation.

The exact solution model shows the difficulty in representing concrete hydration in forms amenable to visual depiction, although this may be approximately done. These exact solutions are complex in form, and practical use is restricted to electronic computation. However, they have the advantage of also allowing temperature gradients to be directly calculated.

CHAPTER 4. IDENTIFICATION OF TIME-COST TRADEOFF AMONG THERMAL CONTROL METHODS (TASK 3)

OVERVIEW OF THE ECONOMIC ANALYSIS APPROACH

The thermal control of mass concrete is a critical factor in ensuring the structural integrity and longevity of large-scale concrete placements. Improper thermal management can lead to excessive internal temperature gradients, which can result in cracking, delayed ettringite formation (DEF), and other durability concerns. In this context, Task 3 aims to assess the economic implications of various thermal control methods, particularly focusing on the trade-off between cost and time in mass concrete applications.

The objective of this task is to evaluate different combinations of mix types and cooling methods to identify cost-effective approaches that comply with the GDOT regulations on temperature control and compressive strength. By comparing the economic impact of each method under controlled thermal conditions, this analysis seeks to provide practical recommendations for contractors in terms of both direct costs (e.g., materials, equipment) and indirect costs (e.g., extended curing periods, labor costs).

In this section, we will provide a comprehensive overview of the thermal control methods considered in Phase III, including passive cooling systems (e.g., insulation blankets), pre-cooling strategies (e.g., liquid nitrogen application), and embedded pipe cooling systems. Additionally, the economic implications of time-cost tradeoffs will be explored, emphasizing the potential for cost savings through optimized material selection and cooling method implementation. This analysis will form the basis for the subsequent sections, where detailed simulation results and findings will be presented.

COST ESTIMATION AND INDUSTRIAL PREFERENCE

The construction industry is currently experiencing significant shifts in material availability and environmental considerations. Phase III addresses these changes by assessing the cost implications of adopting low-carbon, low-heat supplementary cementitious materials (SCMs), particularly reclaimed fly ash (RFA) and Portland Limestone Cement (PLC). With the global depletion of conventional fly ash due to the closure of coal power plants, RFA has emerged as a viable alternative with comparable pricing to conventional fly ash. The industry's increasing emphasis on sustainable construction practices further supports the transition to PLC, which reduces greenhouse gas emissions by approximately 10% compared to traditional Portland cement.

Cost estimation in this context extends beyond material pricing to encompass the financial impact of various cooling systems. However, exact cost calculations can vary significantly depending on project size, location, and specific thermal control requirements. Therefore, rather than providing a detailed cost analysis, the focus is placed on identifying objective parameters such as curing time under different cooling conditions. Phase II provided valuable data on cost variations associated with cooling systems in mass concrete applications. Passive cooling methods, such as insulation blankets and tarping, were noted as relatively low-cost solutions with moderate effectiveness in maintaining temperature differentials. Active cooling systems, including precooling using liquid nitrogen and embedded pipe systems, were associated with significantly higher costs driven by equipment setup, operational requirements, and maintenance.

SCM pricing and contractor preferences play a pivotal role in the decision-making process. The emerging market for RFA, with its comparable cost to conventional fly ash, provides an environmentally favorable option without a significant financial burden. Meanwhile, PLC adoption continues to gain traction as more contractors recognize its

benefits in reducing carbon footprints while maintaining thermal performance. Additionally, the high costs associated with active cooling methods are mitigated when RFA and PLC mixes are used, as these mixes inherently exhibit lower thermal gradients, reducing the need for extensive cooling interventions.

The interplay between SCM selection and cooling system implementation underscores the importance of aligning material choice with project-specific thermal management strategies to achieve both cost efficiency and regulatory compliance in mass concrete projects.

REVIEW OF SR-92 SITE FOR SIMULATION BASELINE

The SR-92 Norfolk Southern Railway bridge construction site in Douglas County, Georgia, serves as the reference baseline for the thermal simulations in Phase III. This site provides a well-documented dataset on cooling configurations, concrete layout, and ambient conditions, making it an ideal benchmark for evaluating alternative mix types and cooling strategies under controlled scenarios.

The SR-92 site includes two primary concrete components: a foundation and an abutment wall. While the foundation, measuring 24.5 ft wide, 37 ft long, and 4.5 ft deep, did not require cooling systems, the abutment, with a thickness of 6 ft, height of 20.5 ft, and length of 37 ft, implemented comprehensive thermal control measures. These configurations will serve as the reference layout in Phase III simulations.

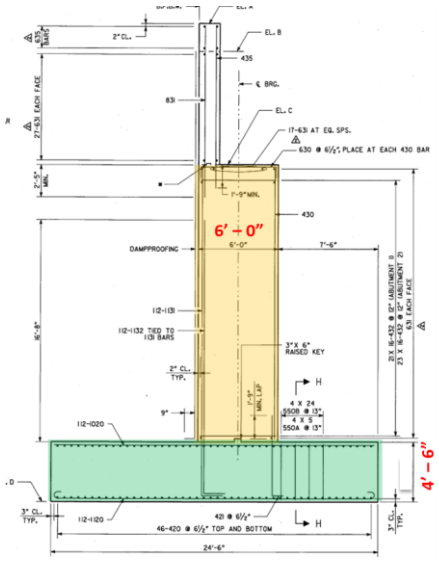

Figure 17. Cross-section view of abutment and foundation of SR-92 bridge.

In the baseline configuration, the cooling system for the abutment includes pre-cooling using liquid nitrogen and ice to reduce placement temperature to approximately 70 °F, along with a post-cooling network consisting of 3/4-inch PEX tubing spaced at 1x2 ft intervals. The chilled water maintained at 45 °F circulates through the system to mitigate temperature increases during curing. Additionally, heavy-duty blankets and sand layers are applied to minimize thermal exchange with the ambient environment.

Phase III simulations will adopt these baseline cooling configurations while modifying the mix types and selectively activating or deactivating specific cooling methods. The objective is to assess the thermal performance of alternative SCM combinations (e.g., Reclaimed Fly Ash, Portland Limestone Cement) under varying cooling conditions, using the SR-92 layout as a control scenario. By maintaining consistent baseline parameters, the analysis will focus on identifying potential trade-offs between cooling system implementation and mix design optimization, particularly in terms of curing time and thermal gradients.

Figure 18 presents the primary cooling components installed in the SR-92 abutment,

including fabricated manifolds, PEX tubing network, and the chiller and water tank assembly. Table 4 provides an overview of the key parameters associated with concrete placement and thermal control at SR-92, establishing the baseline framework for subsequent simulation analyses in Phase III.

A. Fabricated manifolds. B. Installed PEX tubes. C. Chiller and water tank.

Figure 18. Post cooling system used in the SR-92 concrete abutment.

Table 4. The conditions of the concrete placement in SR92 site.

Initial Conditions		**Cooling System**	
Placing temperature	69.3°F	Pipe spacing	1×2 ft
Ambient temperature	81°F	Water temperature	45°F
		PEX tube diameter	¾ in.
Material		**Shields**	
Cement	670 lb/yd^3	Plywood thickness	¾ in.
SCMs	N/A	Blanket thickness	N/A
w/c ratio	0.461	Time of removal	During day 4

THERMAL ASSESSMENT SIMULATION USING B4CAST

The B4Cast thermal assessment model provides a controlled simulation environment to evaluate the thermal performance of selected mix types under varied cooling configurations. By comparing five distinct SCM combinations across passive and active cooling strategies, the objective is to determine whether each mix type adheres to GDOT's thermal

requirements for maximum core temperature and temperature differentials. Additionally, the duration of cooling measures will be analyzed to assess the potential time savings associated with each method, forming the basis for cost-benefit analyses in subsequent sections.

Analysis Methodology

The B4Cast thermal analysis tool is utilized in this phase to systematically evaluate the thermal performance of five distinct mix types under varying cooling conditions. The selected mix types include: Type IL, Type IL + 20% FFA, Type IL + 20% RFA, Type IL + 40% FFA, and Type IL + 40% RFA.

All selected mix types meet the compressive strength requirement of 4,000 psi as specified by GDOT guidelines. Detailed compressive strength data, as outlined in Chapter 2, confirms that each mix type exceeds the minimum strength threshold under laboratory conditions. Specifically, the addition of FFA and RFA demonstrated a slight reduction in early-age strength, but all mixes achieved 4,000 psi within the designated curing period.

Each mix type is assessed under a range of cooling configurations, including both pre-cooling and active cooling strategies, to determine their thermal performance in relation to GDOT requirements. The primary thermal criteria for this analysis are the following:

- Maximum core temperature: must remain below the GDOT threshold of 158°F
- Maximum temperature differential: must not exceed 35°F

The cooling configurations simulated in B4Cast include pre-cooling using liquid nitrogen to reduce placement temperatures and active cooling through embedded PEX tubing circulating chilled water. These configurations are benchmarked against baseline conditions to assess the relative effectiveness of each cooling strategy.

Additionally, the analysis will focus on the following two key metrics for each mix type under each cooling scenario:

1. whether the mix type maintains thermal performance within GDOT limits
2. duration of the thermal control period

This approach enables direct comparisons of thermal performance and curing duration across different mix types and cooling strategies, providing actionable insights into optimal combinations of SCMs and cooling methods in mass concrete applications.

Key Parameters and Configurations

The thermal analysis conducted in Phase III follows the mass concrete design layout established in the SR-92 abutment section. This baseline serves as the reference framework for evaluating alternative mix types and cooling strategies under consistent geometric and environmental conditions.

Ambient Temperature Setting

Mass concrete structures are particularly sensitive to ambient temperature during the curing process, as higher external temperatures can exacerbate thermal gradients and increase the risk of cracking. In general, ambient temperature directly influences the internal temperature rise of mass concrete and the effectiveness of cooling strategies. For this analysis, an ambient temperature of 90°F represents peak summer conditions in Georgia. This temperature serves as a conservative estimate to assess worst-case thermal conditions, allowing for a more rigorous evaluation of cooling methods.

Passive Cooling Strategies

Insulation is a critical component in passive cooling, reducing thermal exchange between the concrete surface and the external environment. The effectiveness of insulation is quantified using the R-value, which indicates the material's resistance to heat flow. The R-

value is calculated as the ratio of the thickness of the insulating material (in inches) to its thermal conductivity (BTU·in/hr·ft²·°F). Mathematically, it can be expressed as:

$$\text{R-value} = \text{Thickness (in)} / \text{Thermal Conductivity (k)}$$

For instance, if a single blanket has a thickness of 1 inch and a thermal conductivity of 0.5 BTU·in/hr·ft²·°F, the R-value would be:

$$R = 1 / 0.5 = 2$$

In the current analysis, the R-values are categorized as follows:

- R0: No insulation applied, representing baseline thermal exchange.
- R1: Intermediate insulation level, estimated to be between R0 and R2.5.
- R2.5: Single layer of insulation blanket applied, a standard practice for moderate thermal control.
- R5: Double layer of insulation blankets, providing maximum resistance to thermal exchange.

Active Cooling Measures

Pre-cooling is employed as a key active cooling strategy, utilizing liquid nitrogen to reduce the initial placement temperature of the concrete. This method was previously implemented in the SR-92 abutment section where liquid nitrogen was applied to achieve a target placement temperature of approximately 70 °F. For Phase III, this pre-cooled temperature will serve as the initial condition for thermal analyses involving active cooling methods. This approach allows for direct comparisons between pre-cooled and non-pre-cooled scenarios, isolating the thermal impact of pre-cooling on each mix type under various ambient temperature conditions.

Analysis Outcomes

The results of the B4Cast thermal analysis are summarized in the table below, which

presents the maximum core temperature, temperature differential, and duration of thermal control across five mix types under varying insulation R-values. The analysis focuses solely on passive cooling strategies, omitting active cooling methods, as most scenarios achieved compliance with GDOT thermal regulations through passive measures alone. This approach emphasizes the effectiveness of insulation under extreme ambient temperature conditions (90 °F).

Table 5. B4Cast thermal analysis focusing on passive cooling strategies.

Ambient Temp	Concrete Temp	No Insulation (R-0)			R-Value = 1.0			R-Value = 2.5			R-Value = 5.0		
		Max Core Temp	Max Temp Diff	End Thermal Control	Max Core Temp	Max Temp Diff	End Thermal Control	Max Core Temp	Max Temp Diff	End Thermal Control	Max Core Temp	Max Temp Diff	End Thermal Control
°F	°F	°F	°F	Days	°F	°F	Days	°F	°F	Days	°F	°F	Days
Type IL													
90	90	182	60	N/A	184	38	6.0	186	24	9.5	187	15	15.4
	80	172	54	N/A	174	34	5.8	175	21	9.0	176	13	14.3
	70	163	48	N/A	164	30	5.5	165	19	8.4	166	12	13.1
IL + 20% FFA													
90	90	164	49	N/A	167	31	5.5	169	20	8.5	170	12	13.7
	80	154	43	N/A	157	28	5.1	158	17	7.8	160	11	12.2
	70	145	37	N/A	146	24	4.8	148	15	7.0	149	9	10.8
IL + 20% RFA													
90	90	165	50	N/A	168	32	5.5	169	20	8.5	171	12	13.7
	80	155	43	N/A	157	28	5.1	159	17	7.8	160	11	12.2
	70	145	37	N/A	147	24	4.8	149	15	7.0	150	9	10.8
IL + 40% FFA													
90	90	149	39	N/A	152	26	4.8	154	16	7.4	156	10	11.6
	80	140	33	N/A	142	22	4.3	144	14	6.4	145	9	9.8
	70	131	27	N/A	132	18	3.8	134	11	5.4	135	7	7.9
IL + 40% RFA													
90	90	147	38	N/A	150	25	4.8	153	16	7.4	154	10	11.7
	80	138	32	N/A	141	21	4.3	143	13	6.4	144	8	9.8
	70	129	26	N/A	131	17	3.7	133	11	5.3	134	7	7.9

Thermal Performance Analysis

Type IL exhibits the highest thermal stress, with maximum core temperatures reaching 182°F under R0 conditions. The temperature differential also exceeds the GDOT limit of 35°F, necessitating extended thermal control durations. Even with R5 insulation, the maximum temperature remains at 187°F, indicating that Type IL is not suitable without additional cooling measures.

IL + 20% FFA and IL + 20% RFA both demonstrate moderate thermal performance improvements over Type IL. The maximum core temperatures drop to 164 °F and 165 °F under R0, with corresponding temperature differentials decreasing to 49 °F and 48 °F, respectively. While these mixes do not consistently meet the GDOT thermal limits without insulation, applying R5 insulation effectively reduces core temperatures to below 160 °F

with thermal control durations shortened to approximately 13 days.

The high-SCM mixes IL + 40% FFA and IL + 40% RFA exhibit the most favorable thermal profiles with maximum core temperatures under R0 conditions reduced to 149 °F and 147 °F, respectively. Applying R5 insulation further reduces these temperatures to 153 °F and 150 °F, well below the GDOT limit. Notably, these mixes achieve thermal control completion within approximately 8 days under R5 insulation, suggesting potential cost savings through shorter curing durations.

Insight on Duration and Cost Reduction

The reduction in thermal control duration observed in high-SCM mixes (40% FFA and 40% RFA) underscores a significant cost-saving opportunity. By minimizing the need for extended thermal management measures, such as prolonged insulation application or active cooling systems, these mixes not only meet GDOT thermal requirements but also have the potential to slightly expedite project schedules. Additionally, the consistent performance of RFA as a sustainable alternative to FFA presents an environmentally favorable option without compromising thermal control efficiency.

Scenario-Based Case Study: Time–Cost Trade-Off Exploration

The results of the B4Cast thermal analysis are summarized in the table below, which presents the maximum core temperature

To explore the trade-off between thermal control duration and construction cost in mass concrete placement, a scenario-based case study was developed. This case study does not rely on real-world pricing data; instead, it introduces a structured conceptual framework using adjustable relative cost indices. The objective is to illustrate how different combinations of mix designs, insulation levels, and cooling strategies influence both direct construction inputs and the associated time required to meet thermal compliance.

The scenario is guided by a conceptual decision model that balances three core objectives: minimizing total cost, ensuring compliance with GDOT thermal specifications, and minimizing the duration of thermal control. These goals represent practical concerns for field engineers when selecting a placement strategy for mass concrete. The model evaluates combinations of mix types and thermal control strategies through a defined structure of inputs, constraints, and outputs.

The key inputs to the model include: the mix type (with varying SCMs), the level of insulation (passive cooling, represented by R-values), the presence of active cooling (via liquid nitrogen application to lower initial temperature), and the thermal performance output (duration of thermal control), derived from B4Cast simulations. The constraints are based on GDOT thermal specifications, specifically limits on maximum core temperature and temperature differential. Any combinations that fail to satisfy these constraints are flagged as infeasible. The outputs include: (1) a relative cost value calculated in Step 1, and (2) a Total Effective Cost value that incorporates indirect time cost, as developed in Step 2.

The foundation of this model is a simple yet meaningful cost structure that includes three components: material cost, insulation cost, and cooling cost. Each component was assigned a relative weight based on its expected influence on cost. The formulas used in this analysis are as follows:

Step1: Relative Cost Calculation

$$Relative\ Cost = C_{mix} + C_{insulation} + C_{cooling}$$

Step2: Total Effective Cost Calculation

$$Total\ Effective\ Cost = Relative\ Cost + \alpha \cdot Duration$$

Where:

- C_{mix} is the cost index of the selected concrete mix
- $C_{insulation}$ is the cost index based on the blanket R-value
- $C_{cooling}$ is the cost index for active cooling of lique nitrogen application
- α is the time cost coefficient

The following table summarizes the weights used in this analysis. Since actual cost values were not available, each component was represented by an adjustable relative parameter. This allowed the comparison to focus on trade-off patterns rather than absolute monetary values, providing a flexible and intuitive means of evaluating different strategies under hypothetical but realistic assumptions.

Table 6. Cost component weights and factors.

Component	Basis	Assigned Value	Notes
Material Cost	SCM replacement level		Lower SCM cost reflects sustainability and heat reduction
IL100	0% SCM	1.00	100% Type IL cement
IL+20% FFA	20% Class F Fly Ash	0.95	Slight cost reduction
IL+20% RFA	20% Reclaimed Fly Ash	0.92	Slightly cheaper than FFA
IL+40% FFA	40% Class F Fly Ash	0.90	Reduced cement, lower cost
IL+40% RFA	40% Reclaimed Fly Ash	0.88	Most cost-effective and sustainable
Insulation Cost	Blanket R-value		
R1.0	Minimal insulation	0.00	No added cost
R5.0	Enhanced insulation	0.20	Incremental cost
Cooling Cost	Initial concrete temperature		Based on active cooling effort
90°F	No cooling	0.00	Baseline
70°F	Active cooling	0.50	Highest level of intervention (e.g., liquid nitrogen)
Time Cost (Indirect)	Thermal control duration (days)	α = 0.04	Applied only in Step 2

The outcome of each scenario was also characterized by its thermal control duration — the number of days required to maintain temperature within specification. However, duration alone is insufficient unless its impact on construction operations is considered. To

address this, the model was extended to include an indirect cost component. A time-penalty coefficient (α) was introduced, multiplying the duration to simulate the broader impact of extended curing time, delayed formwork removal, or slower construction progress. The resulting metric, referred to as Total Effective Cost, reflects both immediate material/cooling costs and the implicit cost of time.

The first analysis, presented in Figure 19A, plots relative cost against thermal control duration for all evaluated combinations. Step 1A highlights trends by cooling strategy, showing a general downward trade-off. Step 1B adds 'X' markers to indicate combinations that fail GDOT thermal limits, filtering out non-compliant low-cost options. It reveals a general inverse trend: as cost increases, required duration decreases. This trend is emphasized by the inclusion of a reference background curve in the form of an inverse function, which serves as a conceptual guide representing the typical behavior of time-cost trade-offs. The rationale behind this shape is that higher-cost strategies tend to involve greater investment in thermal control measures such as higher SCM content or active cooling, which in turn reduce the time required for the concrete to meet thermal compliance. The curve visually reinforces this behavior and helps distinguish outlier combinations that do not align with the expected trade-off pattern. Figure 19B refines this view by identifying combinations that failed to meet GDOT's thermal specifications. These are marked with an 'X' and show that many low-cost, long-duration combinations are thermally infeasible, further supporting the logic of the downward trend.

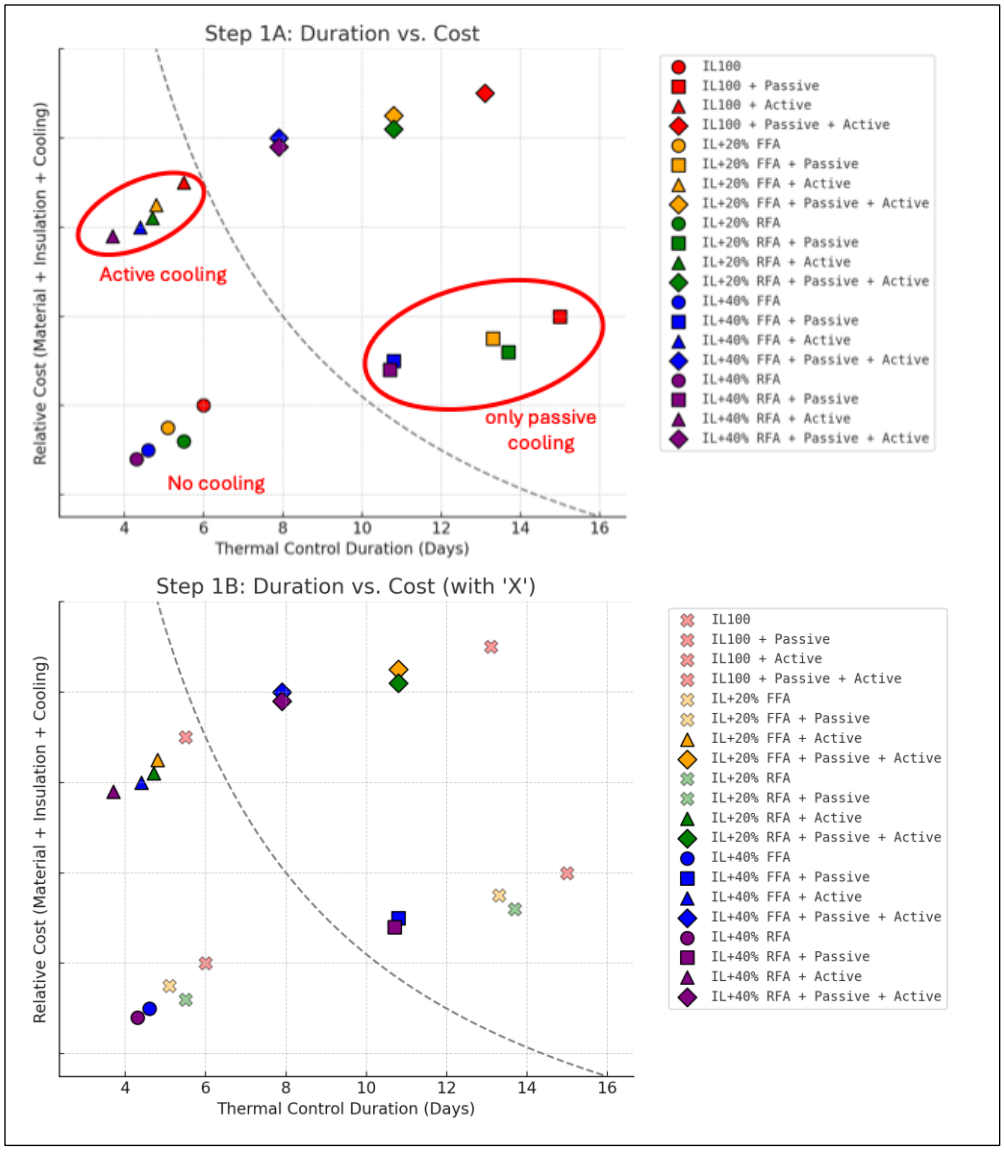

Figure 19. Relative cost vs. thermal control duration.

The second phase of the study introduces the Total Effective Cost metric. Figure 20 plots this value against duration. The time-penalty coefficient α was calibrated such that combinations using only passive or only active cooling strategies tend to cluster in a similar cost range. Given the lack of reliable real-world cost data, this relative and structured approach offers the most intuitive and practical way to visualize trade-offs among feasible options under assumed constraints and estimated parameters. A shaded horizontal band highlights this range, suggesting that there exists a practical efficiency zone where these

strategies yield comparable overall performance. Compared to Step 1, where relative cost alone defined optimality, the inclusion of time cost in Step 2 reshapes the decision space: certain combinations with moderate relative cost but significantly shorter durations become more competitive. For example, combinations with active cooling, which were initially penalized for higher cooling cost, now appear more favorable due to their reduced duration. Notably, the IL+40% RFA mix without any cooling appears to deliver the best performance in this site-specific scenario. Due to the relatively moderate ambient conditions or favorable heat dissipation characteristics of the placement, additional cooling strategies such as insulation or active cooling were not necessary to meet the thermal requirements. This highlights the unique nature of the project conditions, where a sustainable and low-cost mix without cooling outperforms more complex thermal control strategies.

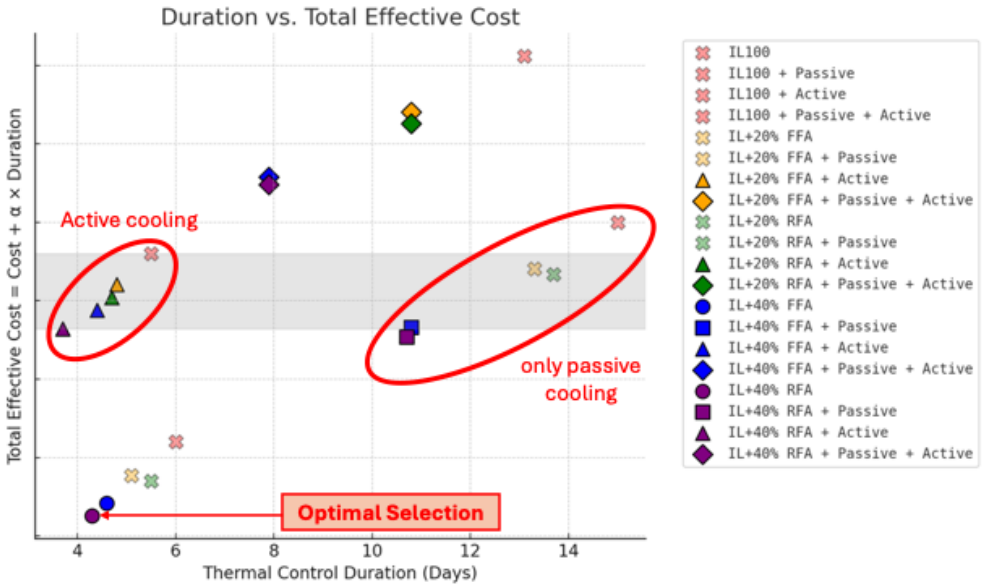

Figure 20. Total Effective Cost vs. duration, incorporating indirect time cost.

This scenario-based case study illustrates how rational selection of mix and thrmal control strategies can be guided by a structured trade-off model. Although it does not use real cost data, the model highlights the critical role of indirect time-related costs and

demonstrates how even modest investments in SCM or cooling can lead to overall project efficiency when time is valued. The approach presented here can be expanded into a formal decision-support tool with the inclusion of site-specific cost figures and scheduling constraints.

FINDINGS AND IMPLICATIONS

The thermal analysis conducted in Phase III provides several key insights regarding the effectiveness of passive cooling methods across various SCM combinations. The primary objective was to evaluate whether selected mix types could maintain GDOT thermal compliance under passive cooling strategies alone, given that active cooling methods were excluded from this phase due to limited observed benefits.

- Thermal Performance Across Mix Types: Type IL consistently exhibited the highest thermal stress, with core temperatures exceeding 180°F under low insulation conditions (R0 and R1). In contrast, high-SCM mixes (40% FFA and 40% RFA) demonstrated more favorable thermal profiles, with peak core temperatures remaining below 155 °F under R5 insulation.
- Duration of Thermal Control: The duration of thermal control varied significantly based on SCM content and insulation level. High-SCM mixes achieved thermal control completion within 8-9 days under R5 insulation, whereas Type IL required up to 15 days, indicating potential cost-saving opportunities through SCM utilization.
- Cost Implications: By reducing the duration of thermal control, high-SCM mixes present a cost-effective alternative to extended insulation application or active cooling. Additionally, RFA emerges as a viable substitute for FFA, offering

comparable thermal performance with potential cost and environmental benefits.

The findings suggest that optimizing SCM content in mass concrete can effectively reduce thermal stress and minimize the need for active cooling methods. Additionally, prioritizing passive cooling strategies, such as R5 insulation, can significantly curtail thermal control durations, translating to reduced labor and material costs. The use of RFA as a sustainable SCM further enhances the cost-benefit profile of mass concrete projects aligning with broader industry trends toward environmentally conscious construction practices.

CHAPTER 5. CASE STUDY: INVESTIGATION OF ALTERNATIVE METHODS TO AVOID ACTIVE COOLING (TASK 4)

INTRODUCTION TO NON-ACTIVE COOLING STRATEGIES

Active cooling systems, such as embedded cooling pipes with chilled water circulation, are widely employed in mass concrete applications to manage internal temperature rise and mitigate thermal gradients. While effective, these systems involve substantial costs, logistical complexity, and increased construction time. Consequently, there is growing interest in exploring non-active cooling strategies that minimize or eliminate reliance on active cooling methods.

This study investigates the feasibility of implementing non-active cooling strategies as a cost-effective alternative for thermal management in mass concrete placements. These strategies primarily focus on precooling materials (e.g., dry ice, liquid nitrogen) and utilizing passive insulation methods (e.g., formwork and blankets) to maintain temperature control during hydration.

To assess the effectiveness of these approaches, simulations were conducted using B4Cast, a finite element software designed to simulate temperature evolution and stress distribution in concrete structures during the hardening process. The simulations were structured to replicate real-world construction scenarios, incorporating site-specific ambient conditions, structural geometry, and thermal boundary conditions.

The study also examined the combined effect of non-active cooling strategies and low-heat cementitious mix designs with high supplementary cementitious material (SCM) replacement rates. By substituting cement with SCMs such as fly ash and reclaimed fly ash, the heat of hydration can be significantly reduced, thereby enhancing the efficacy of passive cooling techniques in controlling thermal gradients and mitigating delayed

ettringite formation.

The objective was to determine whether these strategies, when applied alongside SCM-rich mix designs, could maintain maximum concrete temperatures within the GDOT-specified limits of 158°F and control temperature differentials to 35°F, without the use of embedded cooling pipes. The following sections provide a comprehensive analysis of the findings, with a specific focus on the Albany bridge construction site serving as the primary case study for evaluating the practical implementation of these alternative cooling methods.

SITE OVERVIEW: ALBANY BRIDGE CONSTRUCTION

The case study focuses on a bridge construction project located along State Route 520 (SR 520), spanning the Flint River in Dougherty County, Albany, Georgia. The bridge has a total length of approximately 728 ft, consisting of six spans and supporting vehicular traffic as part of a major transportation network.

The bridge structure comprises both concrete superstructure and substructure components with specified compressive strengths of 4,000 psi and 3,500 psi, respectively. The substructure includes drilled caissons embedded into the riverbed, providing structural support and intermediate bents designed to accommodate river flow and transfer live loads to the foundation.

The bridge's structural configuration, featuring substantial mass concrete components with a minimum dimension exceeding 5 ft, presents an ideal case for evaluating the effectiveness of non-active cooling strategies. The B4Cast simulations incorporated these structural elements to assess thermal behavior under varying environmental and material conditions.

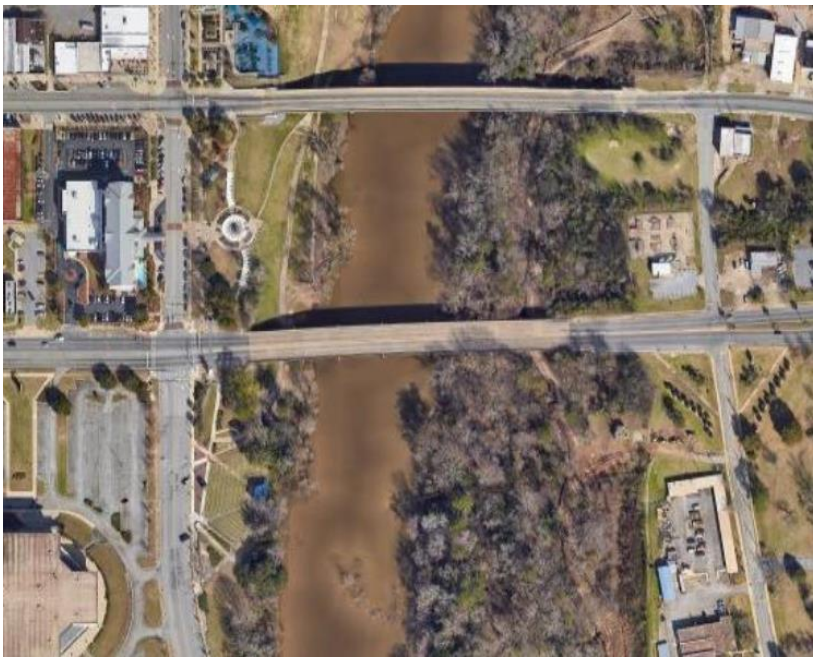

Figure 21. Location of Albany bridge construction project.

B4CAST SIMULATION

Mass Concrete Components

- *Caisson:* The drilled caissons, serving as the primary foundation system, consist of 6 ft diameter cylindrical shafts. Given their submerged positioning, caissons are subject to cooling from river water, potentially leading to significant thermal gradients. Simulations assessed temperature control scenarios in both underwater and ambient air conditions.

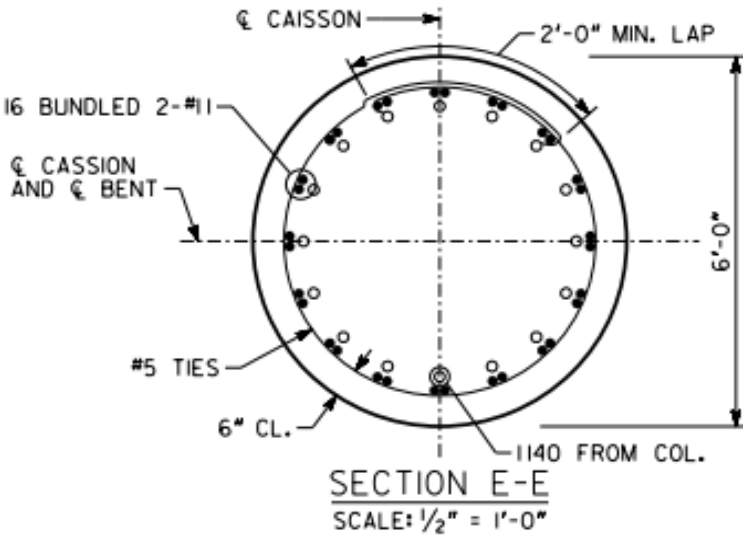

Figure 22. Cross-Section view of drilled caisson geometry.

- *Intermediate Bent:* The intermediate bent structures support the bridge superstructure and range in height from 6.5 ft to 8.5 ft with a consistent width of 5.5 ft. Unlike the caissons, intermediate bents are exposed solely to ambient air temperatures, allowing for focused analysis of passive insulation and precooling techniques.

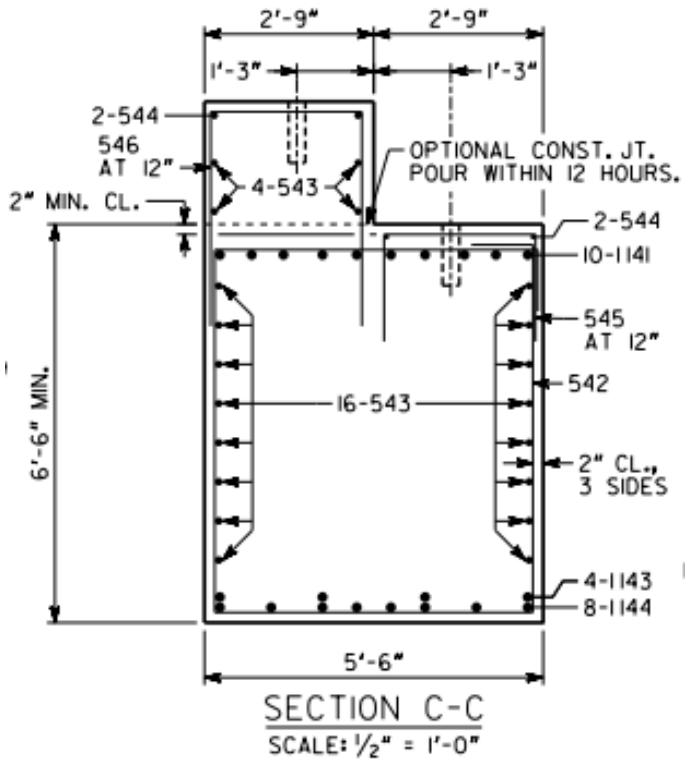

Figure 23. Cross-section view of intermediate bent geometry.

According to the GDOT specifications, any structural concrete element with a minimum dimension of 5 ft or greater qualifies as mass concrete due to the potential for excessive internal temperature buildup and thermal gradients during hydration (Ga.gov, 2025). Both the caisson foundations and intermediate bent elements in the Albany bridge project exceed this threshold, thus qualifying as mass concrete structural elements.

The Albany bridge project's structural configuration, with its mass concrete structural components, presents an ideal case for evaluating the effectiveness of non-active cooling thermal control strategies.

Simulation Parameters

The B4Cast simulations incorporated thermal properties derived from laboratory testing of selected mix designs from Chapter 2. Project-specific ambient conditions were assumed for July, and appropriate weather temperature data and river water temperature data were

acquired from a dataset in USGS (USGS, 2019). Key parameters included: concrete thermal properties (specific heat, thermal conductivity), placement temperature, ambient air and river water temperatures (daily average ranges), formwork insulation assumptions, and element geometry and boundary condition setup.

Table 7. B4Cast thermal analysis input variables for Albany Bridge site.

Parameter	Input Value	Parameter	Input Value
Pre-cooling		**Environmental Factors**	
Initial temperature	20°C (68°F) 13°C (55.4°F)	Ambient temperature	Albany air temperature (July) Albany River water temperature (July)
Post-cooling		**Passive Cooling**	
Int. Bent Cooling pipes	None 2’ x 4’ 4’ x 4’	R-value insulation	1hr·ft2·°F/Btu 2.5hr·ft2·°F/Btu
Caisson Cooling pipes	None 5 pipes 9 pipes	Time of insulation removal	During day 4
Material			
Activation energy	37221 J/mol		
Density	2332 kg/m^3 (3931 lb/yd$^{3)}$		
Heat generation curve	Found using isothermal calorimetry		

For precooling, there were two cases, one without any precooling (68 °F) and one with precooling to 55.4 °F. For ambient temperature in July, one case used air temperature data from Albany, while the other used the river water temperature, respectively. For postcooling, in the case of intermediate bents, the cooling pipes layout options included: no cooling pipes, a 2 ft by 4 ft spacing layout, and a 4 ft by 4 ft spacing layout. Similarly, caissons ranged from no pipes to a five pipe layout with one pipe in the middle and the remaining four tied along the edges to, lastly, a nine-pipe layout with one in the middle and the remaining eight tied along the perimeter of the caisson. For passive cooling, there were

insulations with different R-values provided. “R-X” corresponded to the R-value of X provided as insulation. All insulations were removed during day 4. For each different mix, the heat generation curve parameter was found using isothermal calorimetry curves. Each scenario was run over a 14-day simulation window to capture early-age peak temperature rise and evaluate maximum internal temperatures and the internal thermal gradients.

FINDINGS AND ANALYSIS

The B4Cast simulations were conducted to find the “best-case scenario” to reduce the overall cost of thermal control where no active cooling or additional cooling would be required. Through iterations, best-case scenarios were found from the following five sample mix designs chosen for the compressive tests: IL100, ILF20, ILF40, ILRF20, and ILRF40.

Intermediate Bent Analysis

The intermediate bent was modeled in B4Cast, with parameters matching the construction scenario as closely as possible to reality. Starting off with just passive cooling with an R-1 insulation, no pre-cooling or post-cooling, all mix designs were simulated to achieve the threshold of maximum temperature and temperature gradient set by the GDOT mass concrete specification. For the intermediate bent, baseline mix IL100 and both 20 percent replacement mix ILF20 and ILRF20 all required post-cooling with cooling pipes in order to stay within the threshold of maximum temperature and maximum temperature difference. As shown in Figure 24, the model shows how a 2 ft by 4 ft layout is installed in the intermediate bent. For the 40% replacement mixes, ILF40 and ILRF40, the threshold maximum temperature and the temperature gradient limit were met, even without any installation of post-cooling. However, it did require precooling down to 13 °C. This result

clearly shows that a 40% replacement mix with fly ash is adequate to meet GDOT threshold limits without any postcooling involved. In addition, the results indicated slightly better results with ILRF40 mix, about 1 °C maximum temperature lower and 0.5°C maximum temperature difference lower, compared to ILF40 mix.

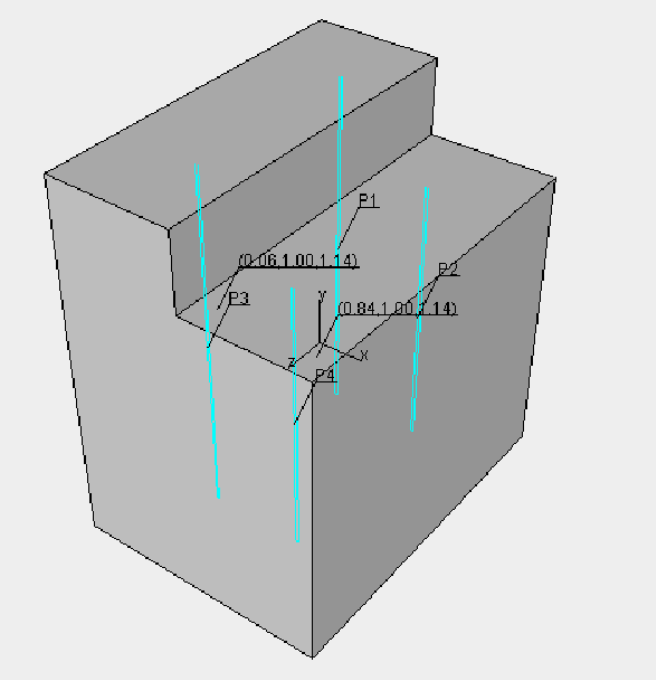

Figure 24. B4Cast model of intermediate bent with 2'x4' layout.

Caisson Analysis

For the second mass concrete element, the caisson was modeled in B4Cast under two different conditions: underwater and in-air. For both the underwater and in-air caisson cases, only IL100 mix required precooling to pass the maximum temperature and temperature gradient threshold, however it did not require active cooling, such as shown in Figure 25. All other mix designs passed the threshold without any additional cooling parameters, except for R-1 insulation. The cylindrical shape of the caisson provides the most volume-to-surface area ratio compared to other shapes such as a rectangular beam. This means that even with the same minimum dimension of 6 feet, a 6 ft diameter caisson

has more surface area compared to a rectangular beam with a width of 6 ft. This means that caissons are generally able to dissipate heat better than the intermediate bent simulation cases.

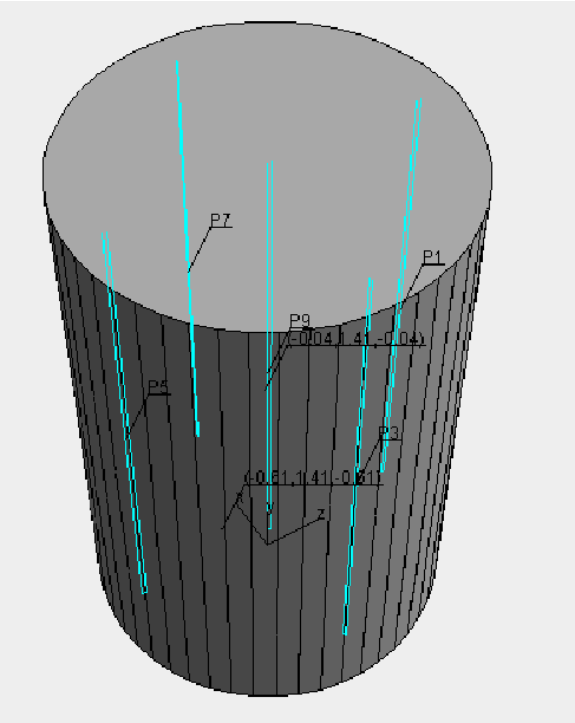

Figure 25. B4Cast model of caisson with 5 pipes layout.

	Mix ID	Amb Temp	Passivecool	Precooling	Postcooling	Status	max temp (°F)	maxtempdelta(°F)
Condition	100IL	Air	R=1	none(20.1dc)	2x4	PASS	149.18	22.27
			R=1	13dc	none	FAIL	151.05	47.90
	20FFA		R=1	none(20.1dc)	2x4	PASS	131.49	18.25
			R=1	13dc	none	FAIL	134.40	39.28
	20RFA		R=1	none(20.1dc)	2x4	PASS	132.73	18.18
			R=1	13dc	none	FAIL	135.05	39.49
	40FFA		R=1	13dc	none	PASS	120.58	31.53
			R=1	none(20.1dc)	none	FAIL	132.79	38.09
	40RFA		R=1	13dc	none	PASS	119.47	31.01
			R=1	none(20.1dc)	none	FAIL	131.56	37.72

Figure 26. Intermediate bent simulation results.

	Cement Mix	Amb Temp	Passivecool	Precooling	Postcooling	Status	max temp (°F)	maxtempdelta(°F)
Condition	100IL	real	R=1	none(20.1dc)	none	FAIL	163.29	31.97
		real	R=1	13dc	none	PASS	150.53	27.72
	20FFA	real	R=1	none(20.1dc)	none	PASS	146.48	26.08
						PASS		
	20RFA	real	R=1	none(20.1dc)	none	PASS	147.16	26.23
						PASS		
	40FFA	real	R=1	none(20.1dc)	none	PASS	132.35	20.74
						PASS		
	40RFA	real	R=1	none(20.1dc)	none	PASS	131.13	20.43
						PASS		

Figure 27. Underwater caisson simulation results.

	Cement Mix	Amb Temp	Passivecool	Precooling	Postcooling	Status	max temp (°F)	maxtempdelta(°F)
Condition	100IL	real	R=1	none(20.1dc)	none	FAIL	163.20	37.01
		real	R=1	13dc	none	PASS	150.33	32.81
	20FFA	real	R=1	none(20.1dc)	none	PASS	146.30	31.19
						PASS		
	20RFA	real	R=1	none(20.1dc)	none	PASS	147.02	31.32
						PASS		
	40FFA	real	R=1	none(20.1dc)	none	PASS	132.08	25.90
						PASS		
	40RFA	real	R=1	none(20.1dc)	none	PASS	131.13	20.43
						PASS		

Figure 28. Typical caisson in air simulation results.

Alternatives for Mass Concrete Construction

The B4Cast simulations conducted for the Albany bridge project provided compelling evidence that non-active cooling strategies, when paired with optimized cementitious mix designs, can effectively mitigate thermal risks associated with mass concrete placements.

As anticipated from laboratory test results from chapter 2, reclaimed fly ash mix (ILRF40) exhibited thermal behavior comparable to, and in most cases slightly better than, traditional Class F fly ash. In the simulated Albany bridge conditions, mixtures containing RFA maintained internal temperature and gradient levels below GDOT threshold limits, without requiring active cooling interventions.

This performance strongly supports the use of RFA as a viable and sustainable alternative to Class F fly ash, which is expected to decline in availability due to the ongoing retirement of coal-fired power plants. RFA, when used with Type IL cement, provides not only environmental and logistical advantages but also strong technical performance in

thermal control, as shown by the results of B4Cast simulation.

Across all simulated scenarios, mixes incorporating high SCM replacement rates (≥40%) with Type IL cement showed reduced adiabatic heat rise and slower thermal gradients. These characteristics, coupled with adequate precooling and passive insulation, ensured that neither the maximum internal temperature nor the maximum allowable temperature differential exceeded the thresholds established by GDOT specifications for mass concrete structures. These findings support a shift in design and construction approach, allowing for more cost-effective, sustainable, and simplified thermal management practices in future GDOT mass concrete projects.

Addendum: Use of the Surrogate Model from Task 2

For cases without postcooling and the intermediate bent geometry, the surrogate model developed in Task 2 was used to compute maximum temperatures. Results are given in the following figure:

Condition	Cement Mix	Amb Temp	Passivecool	Precooling	Postcooling	max temp (°F), B4cast	max temp (°F), FEniCS FEA Simulation	max temp (°F), Task 2 Surrogate Model
	100IL	Air	R=1	none(20.1dc)	2x4			
			R=1	13dc	none	151.1	140.6	140.8
	20FFA		R=1	none(20.1dc)	2x4			
			R=1	13dc	none	134.4	134.1	136.2
	20RFA		R=1	none(20.1dc)	2x4			
			R=1	13dc	none	135.1	126.2	126.5
	40FFA		R=1	13dc	none	120.6	119.4	114.7
			R=1	none(20.1dc)	none	132.8	132.7	130.5
	40RFA		R=1	13dc	none	119.5	114.0	113.7
			R=1	none(20.1dc)	none	131.6	127.0	129.3

Figure 29. Surrogate model results.

Comparison to B4Cast simulations are favorable in 20FFA, 40FFA (no precooling) and 40RFA (no precooling) cases. In other cases the comparision is less favorable, perhaps reflecting that the surrogate model was not trained on B4Cast simulations; for this reason the table also includes a comparison to simulations using the FEniCS finite element simulation package used to train the surrogate model. For these comparisons the surrogate

model compares well.

CONCLUSION

The B4Cast simulations conducted for the Albany bridge project demonstrated the viability of non-active cooling strategies when coupled with SCM-rich mix designs. Specifically, ILRF40 showed comparable or superior thermal performance to traditional Class F fly ash mixes, suggesting that reclaimed fly ash is a promising alternative given the anticipated decline in conventional fly ash availability.

For intermediate bents, mixes with 40% SCM replacement effectively mitigated thermal gradients without active cooling but required strategic precooling to achieve optimal results. For caissons, the cylindrical shape allowed for enhanced heat dissipation, reducing the necessity for postcooling even in underwater conditions.

Overall, the findings indicate that high SCM replacement mixes combined with precooling and passive insulation present a viable alternative to active cooling methods in mass concrete applications. Future research should focus on field-scale validation to further refine these strategies and assess long-term thermal and structural performance.

CHAPTER 6. THE BEST PRACTICE GUIDELINE FOR MASS CONCRETE

The best practice guidelines for mass concrete construction aim to provide comprehensive recommendations that integrate findings from Phases I, II, and III of this research project. The guidelines focus on material selection, thermal control methods, and decision-making frameworks that leverage the newly developed predictive tools and validated cooling strategies. By consolidating the lessons learned across various simulation and laboratory testing scenarios, the guidelines provide actionable guidance for minimizing thermal gradients, optimizing material costs, and achieving regulatory compliance in mass concrete construction projects.

MATERIAL SELECTION

The selection of appropriate cementitious materials is pivotal in controlling temperature rise and reducing thermal gradients in mass concrete. Incorporating SCM-rich mixes, such as reclaimed fly ash (RFA) or Class F fly ash at high replacement levels (≥ 40%), has been proven to effectively mitigate temperature rise while maintaining structural integrity. Type IL cement is now a typical standard of the current industry and would be a good choice for mass concrete applications due to its lower heat of hydration than type I/II cement. Availability and sourcing of SCMs must also be evaluated to mitigate supply chain variability. Moreover, project-specific features such as structural geometry, placement location, and anticipated environmental conditions should guide the choice of cementitious materials to ensure optimal thermal performance.

THERMAL CONTROL METHODS

Environmental factors such as ambient temperature, wind speed, and curing method significantly influence the effectiveness of thermal control strategies. For projects located in high-temperature regions, precooling techniques like chilled water or dry ice batching are recommended to maintain placement temperatures below 70 °F. Passive cooling measures, such as R-2.5 insulation blankets, can effectively minimize thermal gradients during curing but must be monitored through embedded sensors to ensure uniform thermal control. For projects with complex geometries or extensive mass concrete elements, a combination of passive and active cooling methods may be necessary to maintain temperature differentials within the GDOT limits.

DECISION-MAKING

A robust decision-making framework is essential for implementing effective thermal control strategies in mass concrete construction. The nomograms developed in Phase III offer a rapid estimation of maximum concrete temperatures under various cooling scenarios. By integrating Bayesian uncertainty modeling, practitioners can account for material property variations and environmental conditions, enhancing predictive accuracy. Furthermore, cost-benefit analyses should be employed to assess the trade-offs between passive, precooling, and active cooling methods, with an emphasis on minimizing costs and environmental impact.

IMPLEMENTATION AND MONITORING

Effective implementation of thermal control strategies requires a systematic approach to monitoring and data analysis. Project-specific thermal control plans should be developed using predictive modeling data and validated cooling strategies, with real-time temperature

monitoring employed to verify the effectiveness of selected measures. Temperature sensors should be strategically placed to capture data at critical locations, allowing for timely adjustments to the thermal control plan based on real-time observations.

CHAPTER 7. CONCLUSION

The Phase III research successfully extended the scope of mass concrete thermal management by incorporating emerging cementitious materials and refining predictive modeling tools. The findings from each task collectively provide a comprehensive framework for optimizing thermal control strategies.

In Task 1, the investigation of SCM-rich mixes demonstrated that 40% reclaimed fly ash (ILRF40) effectively reduces heat generation and thermal gradients without compromising compressive strength. The use of Type IL cement further moderated temperature rise, providing a sustainable alternative to conventional cementitious materials. The results indicate that reclaimed fly ash has competitive performance to conventional Class F fly ash, suggesting a sustainable alternative to substitute for declining fly ash availability.

Task 2 focused on refining and validating the nomograms developed in Phase II, incorporating Bayesian statistical models to account for material variability and environmental conditions. The resulting predictive tools enable quick but conservative estimation of maximum temperatures, offering practical guidance for early-stage planning.

Task 3 introduced a time-cost tradeoff analysis to evaluate the economic implications of cooling strategies. High SCM mixes, particularly ILRF40 and ILF40, exhibited reduced thermal gradients, allowing for shorter curing durations and lower cooling costs. The findings emphasize the feasibility of passive and precooling methods as cost-effective alternatives to embedded pipe systems.

In Task 4, the Albany Bridge case study validated the effectiveness of non-active cooling strategies under real-time conditions. By employing precooling and passive

cooling, SCM-rich mixes successfully maintained thermal control without active cooling interventions, and the mix designs and best alternative were verified through mass concrete structure simulation via B4Cast, reinforcing the practical viability of the proposed guidelines.

The findings underscore the potential for SCM-rich mixes not only to mitigate thermal gradients but also to shorten curing durations, thereby reducing labor and material costs. The use of reclaimed fly ash as a sustainable SCM presents a viable alternative to conventional Class F fly ash, aligning thermal control practices with broader environmental objectives. Furthermore, the study highlights the importance of integrating predictive modeling techniques to refine thermal control guidelines and improve decision-making across diverse construction scenarios. The outcomes of Phase III provide GDOT with actionable guidance for adopting sustainable, cost-effective thermal management practices in mass concrete construction, ultimately enhancing project efficiency and reducing environmental impact.

ACKNOWLEDGMENTS

The research reported herein was sponsored by the Georgia Department of Transportation (GDOT) through Research Project Number 22-21. The research team gratefully acknowledges the support and contributions of GDOT personnel throughout the project, especially Mr. Patrick Allen, Director of Construction; Mr. John Hancock, Administrator of Construction; Mr. Beau Quarles, P.E., Assistant State Construction Administrator; and Ms. Kamari Jordan, Research Project Manager.

REFERENCES

Abril-Pla, O., Andreani, V., Carroll, C., Dong, L., Fonnesbeck, C. J., Kochurov, M., Kumar, R., Lao, J., Luhmann, C. C., & Martin, O. A. (2023). PyMC: a modern, and comprehensive probabilistic programming framework in Python. *PeerJ Computer Science*, *9*, e1516.

Al-Hasani, L. E., Park, J., Brown, J. B., Antommattei, O., Cho, Y. K., Gentry, T. R., & Kurtis, K. E. (2024). Performance-based limit criteria and temperature mitigation alternatives for the holistic reassessment of a mass concrete structure. *Case Studies in Construction Materials*, *20*, e03326.

Al-Hasani, L. E., Park, J., Perez, G., Herndon, H. N., Brown, J. B., Cho, Y. K., Gentry, T. R., & Kurtis, K. E. (2022). Quantifying concrete adiabatic temperature rise based on temperature-dependent isothermal calorimetry; modeling and validation. *Materials and Structures*, *55*(7), 191.

Al-Hasani, L. E., Perez, G., Herndon, H. N., Park, J., Poole, J. L., Tien, I., Washburn, N. R., Cho, Y. K., Gentry, T. R., & Kurtis, K. E. (2023). Prediction of heat of hydration of cementitious systems using Gaussian process regression enables mass concrete thermal modeling. *Materials and Structures*, *56*(2), 45.

Alnæs, M., Blechta, J., Hake, J., Johansson, A., Kehlet, B., Logg, A., Richardson, C., Ring, J., Rognes, M. E., & Wells, G. N. (2015). The FEniCS project version 1.5. *Archive of Numerical Software*, *3*(100).

ASTM International. (2017). *STM C1679 Standard Practice for Measuring Hydration Kinetics of Hydraulic Cementitious Mixtures Using Isothermal Calorimetry*. ASTM International.

ASTM International. (2019). *ASTM C1738 / C1738M-19, Standard Practice for High-Shear Mixing of Hydraulic Cement Pastes*.

b4cast. (2025). *Simulation of Hardening Concrete*. http://www.b4cast.com/b4cast/b4cast.html

Brown, J., Al-Hasani, L. E., Park, J., Kurtis, K. E., Gentry, R., & Cho, Y. K. (2023). Family of thermal nomograms for mass concrete. *ACI Materials Journal*, *120*(6), 81–93.

Cho, Y. K., Gentry, R., Brown, J., Kahn, L. F., & Park, J. (2019). *Investigation and guidelines for mass concrete construction management*. Georgia. Dept. of Transportation.

Cho, Y. K., Gentry, R., Kurtis, K., Brown, J., Park, J., & Hasani, L. Al. (2022). *Phase II–Investigation and guidelines for best practices of mass concrete construction management*. Georgia. Department of Transportation. Office of Performance-Based ….

Cole, K., Beck, J., Haji-Sheikh, A., & Litkouhi, B. (2010). *Heat conduction using Greens functions*. CRC Press.

Cooper M. (n.d.). *Spragg R Portland Limesone Cement*.

Diaz-Loya, I., Juenger, M., Seraj, S., & Minkara, R. (2019). Extending supplementary cementitious material resources: Reclaimed and remediated fly ash and natural pozzolans. *Cement and Concrete Composites*, *101*, 44–51.

Ga.gov. (2025). *GDOT Specifications for Contractors*. 2025. www.dot.ga.gov/GDOT/pages/TheSource.aspx

Georgia Department of Transportation. (2013). *DOT state of Georgia Special Provision, Section 500-Concrete Structures*.

McElreath, R. (2018). *Statistical rethinking: A Bayesian course with examples in R and Stan*. Chapman and Hall/CRC.

Park, J., Brown, J., Al-Hasani, L. E., Gentry, T. R., Kurtis, K. E., & Cho, Y. K. (2024). Cost-Effective Thermal Control Planning for Mass Concrete Construction Using Nomograms. *Journal of Construction Engineering and Management*, *150*(10), 06024001.

Rashidi, M., Paul, A., Kim, J.-Y., Jacobs, L. J., & Kurtis, K. E. (2017). Insights into delayed ettringite formation damage through acoustic nonlinearity. *Cement and Concrete Research*, *95*, 1–8.

Riding, K. A., Poole, J. L., Folliard, K. J., Juenger, M. C. G., & Schindler, A. K. (2012). Modeling hydration of cementitious systems. *ACI Materials Journal*, *109*(2), 225–234.

Riding, K. A., Poole, J. L., Schindler, A. K., Juenger, M. C. G., & Folliard, K. J. (2006). Evaluation of temperature prediction methods for mass concrete members. *ACI Materials Journal*, *103*(5), 357–

365.
Schindler, A. K., & Folliard, K. J. (2005). Heat of hydration models for cementitious materials. *ACI Materials Journal*, *102*(1), 24.
Standard Specification for Blended Hydraulic Cements. . (2025). ttps://store.astm.org/c0595-08a.html
Standard Specification for Coal Fly Ash and Raw or Calcined Natural Pozzolan for Use in Concrete. (2025). https://store.astm.org/c0618-22.html.
Sustainable construction for a circular economy. In: Cement Association of Canada. (2025). https://cement.ca/sustainability/portland-limestone-cement/
SUZUKI, Y., HARADA, S., MAEKAWA, K., & TSUJI, Y. (1988). Evaluation of adiabatic temperature rise of concrete measured with the new testing apparatus. *Doboku Gakkai Ronbunshu*, *1988*(396), 109–117.
USGS. (2019). *USGS Water Data for the Nation*. waterdata.usgs.gov/nwis
Wadsö, L. (2003). An experimental comparison between isothermal calorimetry, semi-adiabatic calorimetry and solution calorimetry for the study of cement hydration. *Nordtest Report TR*, *522*.
Xu, Q., Wang, K., Medina, C., & Engquist, B. (2015). A mathematical model to predict adiabatic temperatures from isothermal heat evolutions with validation for cementitious materials. *International Journal of Heat and Mass Transfer*, *89*, 333–338.

APPENDIX

Point estimates for G and L in SI units

Using SI units, the model of L uses U-value:

$$ln\left(\frac{1}{L}\right) = m\frac{Ea}{RT_i} + m_1\Delta T_a + m_2\frac{V}{qA} + m_3 ln(U) + m_4 T_{amb} + \Sigma b_{**}$$

and limiting the analysis to situations with $V/qA \geq 1$ ft ≈ 0.4 m and $T_i \geq 10°C = 50°F$, we get the following point-estimate for the parameters of the models for G and L:

If we limit the analysis to situations where $V/qA < 1$, we get

Derivation of the Green's function solution for temperature

Governing equations

Consider a three-dimensional cuboid of concrete undergoing early-age hydration. The dimensions are:

- widthW in the x (or w) direction
- depth D in the y (or d) direction
- height H in the z (or h) direction

For simplicity we assume the $\mathrm{z} = 0$ surface is adiabatic. Due to symmetry, we only need to solve for one quadrant of the cuboid, i.e., one sized $(\frac{\mathrm{W}}{2}, \frac{\mathrm{D}}{2}, \mathrm{H})$. For this quarter cuboid, the $(\mathrm{x} = 0, \mathrm{y} = 0, \mathrm{z} = 0)$ surfaces are adiabatic, and the outer surfaces $(\mathrm{x} = \frac{\mathrm{W}}{2}, \mathrm{y} = \frac{\mathrm{D}}{2}, \mathrm{z} = \mathrm{H})$ have boundary conditions defined by convection and possibly insulating blankets; the blankets are combined with convection to have an effective $\mathrm{U-value}$ or effective convection coefficient h. The ambient temperature is T_∞. The initial temperature is $\mathrm{T_i}$ at all locations in the cuboid. The governing equation with initial and boundary conditions is then

$$\frac{\partial T}{\partial t} = \alpha\left(\frac{\partial^2 T}{\partial x^2} + \frac{\partial^2 T}{\partial y^2} + \frac{\partial^2 T}{\partial z^2}\right) + \frac{1}{\rho c}\dot{e}_{gen}$$

$$T(x, y, z, t = 0) = T_i$$

$$\frac{\partial T}{\partial x}|_{x=0} = 0$$

$$\frac{\partial T}{\partial y}|_{y=0} = 0$$

$$\frac{\partial T}{\partial z}|_{z=0} = 0$$

$$-\kappa\frac{\partial T}{\partial x}|_{x=W/2} = h_x(T|_{x=D/2} - T_\infty)$$

$$-\kappa\frac{\partial T}{\partial y}|_{y=D/2} = h_y(T|_{y=D/2} - T_\infty)$$

$$-\kappa\frac{\partial T}{\partial z}|_{z=H} = h_z(T|_{z=H} - T_\infty)$$

where ρ is density, c is specific heat, κ is thermal conductivity, α is thermal diffusivity, and $\dot{e}_{gen}$ is the energy generation due to cement hydration. We can model $\dot{e}_{gen}$ using the "Suzuki" model:

$$\dot{e}_{gen} = 2\rho c\Delta T_a G t e^{-Gt^2}$$

where ΔT_a is the adiabatic temperature rise and G is a gain factor that depends, in part, on the initial concrete temperature T_i. With this, and rewriting the boundary conditions slightly for reasons that will become apparent, the governing equations can then be written as

$$\frac{\partial T}{\partial t} = \alpha\left(\frac{\partial^2 T}{\partial x^2} + \frac{\partial^2 T}{\partial y^2} + \frac{\partial^2 T}{\partial z^2}\right) + 2\Delta T_a G t e^{-Gt^2}$$

$$'T(x, y, z, t = 0) = T_i$$

$$\frac{\partial T}{\partial x}|_{x=0} = 0 = f_{x1}$$

$$\frac{\partial T}{\partial y}|_{y=0} = 0 = f_{y1}$$

$$\frac{\partial T}{\partial z}|_{z=0} = 0 = f_{z1}$$

$$\kappa\frac{\partial T}{\partial x}|_{x=W/2} + h_x T_{x=W/2} = h_x T_\infty = f_{x2}$$

$$\kappa\frac{\partial T}{\partial y}|_{y=D/2} + h_y T_{y=D/2} = h_y T_\infty = f_{y2}$$

$$\kappa\frac{\partial T}{\partial z}|_{z=H} + h_z T_{z=H} = h_z T_\infty = f_{z2}$$

Solution by Green's functions

For a multidimensional solution, the solution will be a function of the product of 1-dimensional Green's functions **G**, and will involve integrating over time t and over the volume **V** whose coordinates are **x**. Using the notation of the original Green's functions paper, the current problem, in the x direction, is referred to as X23B01T0Gt-, and the correspoinding Green's function is referred to as $\mathbf{G}_{\mathrm{X23}}$. In the y direction, we would say Y23B01T0Gt-, and $\mathbf{G}_{\mathrm{Y23}}$, and z would be similar, $\mathbf{G}_{\mathrm{Z23}}$. We will be using the product $\mathbf{G}_{\mathrm{X23}}\mathbf{G}_{\mathrm{Y23}}\mathbf{G}_{\mathrm{Z23}}$ which for brevity we'll sometimes refer to as $\mathbf{G}_{\mathrm{XYZ}}$.

The solution $\mathrm{T(x, y, z, t)}$ is composed of contributions, in terms of the product of Green's functions $\mathbf{G}_{\mathrm{XYZ}}$, from the initial and boundary conditions, and from internal energy generation

$$T(x, y, z, t) = T_{ic}(\mathbf{G}_{XYZ}) + T_{bc}(\mathbf{G}_{XYZ}) + T_{egen}(\mathbf{G}_{XYZ})$$

Initial condition component

The contribution from the initial condition, noting that $T_i \neq f(x, y, z)$ is

$$T_{ic}(\mathbf{G}_{XYZ}) = \int_{\mathbf{V}} \mathbf{G}_{XYZ}\,(\mathbf{x}, t|\mathbf{x}', \gamma = 0) T_i(\mathbf{V}') d\mathbf{V}'$$
$$= T_i \int_{x'=0}^{W/2} \int_{y'=0}^{D/2} \int_{z'=0}^{H} \mathbf{G}_{X23}\,(x, t|x', \gamma = 0) \cdot \mathbf{G}_{Y23}(y, t|y', \gamma = 0) \cdot \mathbf{G}_{Z23}(z, t|z', \gamma = 0) dx' dy' dz'$$

This term can be eliminated by redefining the temperature scale such that $T_i = 0$:

$T = T - T_i$.

Boundary condition component

Taking the material properties α and κ as constants, the boundary contributions are of the form:

$$T_{bc}(\mathbf{G}_{XYZ}) = \frac{\alpha}{\kappa} \int_{\gamma=0}^{t} \sum_{i=1}^{s} \int_{S_i} f_i\, \mathbf{G}_{XYZ}(\mathbf{x}, t|\mathbf{x}_{i'}, \gamma) ds_{i'} d\gamma$$

where S_i denotes the i-th surface, of which there are $s = 6$ for the cuboids under consideration. The f_i are the boundary condition 'functions' given in the statement of the problem above. Here we number them:

$$f_{x1}(x = 0) = f_1(x = 0) = 0$$
$$f_{x2}(x = W/2) = f_2(x = W/2) = h_x T_\infty$$
$$f_{y1}(y = 0) = f_3(y = 0) = 0$$
$$f_{y2}(y = D/2) = f_4(y = D/2) = h_y T_\infty$$
$$f_{z1}(z = 0) = f_5(z = 0) = 0$$
$$f_{z2}(z = H) = f_6(z = H) = h_z T_\infty$$

Expanding the summation over the surfaces and incorporating the f_*:

$$T_{bc}(\mathbf{G}_{XYZ}) = \frac{\alpha}{\kappa} \int_{\gamma=0}^{t} \int_{y'=0}^{D/2} \int_{z'=0}^{H} h_x\, T_\infty \cdot \mathbf{G}_{X23}(x, t|x' = W/2, \gamma) \cdot \mathbf{G}_{Y23}(y, t|y', \gamma) \cdot \mathbf{G}_{Z23}(z, t|z', \gamma) dy' dz' d\gamma$$
$$+ \frac{\alpha}{\kappa} \int_{\gamma=0}^{t} \int_{x'=0}^{W/2} \int_{z'=0}^{H} h_y\, T_\infty \cdot \mathbf{G}_{X23}(x, t|x', \gamma) \cdot \mathbf{G}_{Y23}(y, t|y' = D/2, \gamma) \cdot \mathbf{G}_{Z23}(z, t|z', \gamma) dx' dz' d\gamma$$
$$+ \frac{\alpha}{\kappa} \int_{\gamma=0}^{t} \int_{x'=0}^{W/2} \int_{y'=0}^{D/2} h_z\, T_\infty \cdot \mathbf{G}_{X23}(x, t|x', \gamma) \cdot \mathbf{G}_{Y23}(y, t|y', \gamma) \cdot \mathbf{G}_{Z23}(z, t|z' = H, \gamma) dx' dy' d\gamma$$

taking the convection coefficients to be constant in time and different on each face but not varying over their respective faces, and leaving open that the ambient temperature may be a function of time:

$$T_{bc}(\mathbf{G}_{XYZ}) = \frac{\alpha}{\kappa} h_x \int_{\gamma=0}^{t} T_\infty \int_{y'=0}^{D/2} \int_{z'=0}^{H} \mathbf{G}_{X23}\,(x,t|x'=W/2,\gamma)\cdot \mathbf{G}_{Y23}(y,t|y',\gamma)\cdot \mathbf{G}_{Z23}(z,t|z',\gamma)dy'dz'd\gamma$$
$$+\frac{\alpha}{\kappa} h_y \int_{\gamma=0}^{t} T_\infty \int_{x'=0}^{W/2} \int_{z'=0}^{H} \mathbf{G}_{X23}\,(x,t|x',\gamma)\cdot \mathbf{G}_{Y23}(y,t|y'=D/2,\gamma)\cdot \mathbf{G}_{Z23}(z,t|z',\gamma)dx'dz'd\gamma$$
$$+\frac{\alpha}{\kappa} h_z \int_{\gamma=0}^{t} T_\infty \int_{x'=0}^{W/2} \int_{y'=0}^{D/2} \mathbf{G}_{X23}\,(x,t|x',\gamma)\cdot \mathbf{G}_{Y23}(y,t|y',\gamma)\cdot \mathbf{G}_{Z23}(z,t|z'=H,\gamma)dx'dy'd\gamma$$

Let's examine the Green's functions and go through the integrations. Consider the x direction as the prototype:

$$\mathbf{G}_{X23} = \frac{2}{L_x}\sum_{m=1}^{\infty} e^{-\beta_{x,m}^2\alpha(t-\gamma)/L_x^2}\frac{\beta_{x,m}^2+Bi_x^2}{\beta_{x,m}^2+Bi_x^2+Bi_x}\cdot\cos\left(\beta_{x,m}\frac{x}{L_x}\right)\cdot\cos\left(\beta_{x,m}\frac{x'}{L_x}\right)$$

Where L_x is the total length in the x direction. For all the directions:

- for x, $L_x = W/2$
- for y, $L_y = D/2$
- for z, $L_z = H$

and

$$\beta_{*,m}tan\beta_{*,m} = Bi_* = \frac{h_* L_*}{\kappa}$$

where $_*$ is the wild card for x, y,or z. Spatial integrations operate on each Green's function individually. We will need to integrate from $x' = 0$ to $x' = L_x$:

$$\int_{x'=0}^{L_x}\mathbf{G}_{X23}\,(x,t|x',\gamma)dx' = \int_{x'=0}^{L_x}\frac{2}{L_x}\sum_{m=1}^{\infty} e^{-\beta_{x,m}^2\alpha(t-\gamma)/L_x^2}\frac{\beta_{x,m}^2+Bi_x^2}{\beta_{x,m}^2+Bi_x^2+Bi_x}\cdot\cos\left(\beta_{x,m}\frac{x}{L_x}\right)\cdot\cos\left(\beta_{x,m}\frac{x'}{L_x}\right)dx'$$
$$= \frac{2}{L_x}\sum_{m=1}^{\infty} e^{-\beta_{x,m}^2\alpha(t-\gamma)/L_x^2}\frac{\beta_{x,m}^2+Bi_x^2}{\beta_{x,m}^2+Bi_x^2+Bi_x}\cdot\cos\left(\beta_{x,m}\frac{x}{L_x}\right)\cdot\frac{L_x}{\beta_{x,m}}\sin(\beta_{x,m})$$
$$= 2\sum_{m=1}^{\infty} e^{-\beta_{x,m}^2\alpha(t-\gamma)/L_x^2}\frac{\beta_{x,m}^2+Bi_x^2}{\beta_{x,m}^2+Bi_x^2+Bi_x}\cdot\cos\left(\beta_{x,m}\frac{x}{L_x}\right)\cdot\frac{1}{\beta_{x,m}}\sin(\beta_{x,m})$$
$$= 2\sum_{m=1}^{\infty}\mathbf{C}_{x,m}\cdot\mathbf{S}_{x,m}$$

where $\mathbf{C}_{x,m}$ is the time (**C**hronos) term, and $\mathbf{S}_{x,m}$ is the **S**pace term:

$$\mathbf{C}_{x,m} = e^{-\beta_{x,m}^2\alpha(t-\gamma)/L_x^2}$$
$$\mathbf{S}_{x,m} = \frac{\beta_{x,m}^2+Bi_x^2}{\beta_{x,m}^2+Bi_x^2+Bi_x}\cdot\cos\left(\beta_{x,m}\frac{x}{L_x}\right)\cdot\frac{1}{\beta_{x,m}}\sin(\beta_{x,m})$$

For convenience, we write the term that is not integrated, $\mathbf{G}_{X23}(x,t|x'=W/2=L_x,\gamma)$, and similar as

$$\mathbf{G}_{X23}(x,t|x'=W/2=L_x,\gamma)=\frac{2}{L_x}\sum_{m=1}^{\infty}e^{-\beta_{x,m}^2\alpha(t-\gamma)/L_x^2}\frac{\beta_{x,m}^2+Bi_x^2}{\beta_{x,m}^2+Bi_x^2+Bi_x}\cdot\cos\left(\beta_{x,m}\frac{x}{L_x}\right)\cdot\cos(\beta_{x,m})$$
$$=\frac{2}{L_x}\sum_{m=1}^{\infty}\mathbf{C}_{x,m}\cdot\hat{\mathbf{S}}_{x,m}$$

where

$$\hat{\mathbf{S}}_{x,m}=\frac{\beta_{x,m}^2+Bi_x^2}{\beta_{x,m}^2+Bi_x^2+Bi_x}\cdot\cos\left(\beta_{x,m}\frac{x}{L_x}\right)\cdot\cos(\beta_{x,m})$$

Then we can write $T_{bc}(\mathbf{G}_{XYZ})$ compactly as

$$T_{bc}(\mathbf{G}_{XYZ})=8\frac{\alpha h_x}{\kappa L_x}\int_{\gamma=0}^{t}T_\infty\sum_{m=1}^{\infty}\mathbf{C}_{x,m}\,\hat{\mathbf{S}}_{x,m}\sum_{n=1}^{\infty}\mathbf{C}_{y,n}\,\mathbf{S}_{y,n}\sum_{p=1}^{\infty}\mathbf{C}_{z,p}\,\mathbf{S}_{z,p}d\gamma$$
$$+8\frac{\alpha h_y}{\kappa L_y}\int_{\gamma=0}^{t}T_\infty\sum_{m=1}^{\infty}\mathbf{C}_{x,m}\,\mathbf{S}_{x,m}\sum_{n=1}^{\infty}\mathbf{C}_{y,n}\,\hat{\mathbf{S}}_{y,n}\sum_{p=1}^{\infty}\mathbf{C}_{z,p}\,\mathbf{S}_{z,p}d\gamma$$
$$+8\frac{\alpha h_z}{\kappa L_z}\int_{\gamma=0}^{t}T_\infty\sum_{m=1}^{\infty}\mathbf{C}_{x,m}\,\mathbf{S}_{x,m}\sum_{n=1}^{\infty}\mathbf{C}_{y,n}\,\mathbf{S}_{y,n}\sum_{p=1}^{\infty}\mathbf{C}_{z,p}\,\hat{\mathbf{S}}_{z,p}d\gamma$$

or as

$$T_{bc}(\mathbf{G}_{XYZ})=8\frac{\alpha h_x}{\kappa L_x}\sum_{m=1}^{\infty}\sum_{n=1}^{\infty}\sum_{p=1}^{\infty}\left(\int_{\gamma=0}^{t}T_\infty\,\mathbf{C}_{x,m}\mathbf{C}_{y,n}\mathbf{C}_{z,p}d\gamma\right)\hat{\mathbf{S}}_{x,m}\mathbf{S}_{y,n}\mathbf{S}_{z,p}$$
$$+8\frac{\alpha h_y}{\kappa L_y}\sum_{m=1}^{\infty}\sum_{n=1}^{\infty}\sum_{p=1}^{\infty}\left(\int_{\gamma=0}^{t}T_\infty\,\mathbf{C}_{x,m}\mathbf{C}_{y,n}\mathbf{C}_{z,p}d\gamma\right)\mathbf{S}_{x,m}\hat{\mathbf{S}}_{y,n}\mathbf{S}_{z,p}$$
$$+8\frac{\alpha h_z}{\kappa L_z}\sum_{m=1}^{\infty}\sum_{n=1}^{\infty}\sum_{p=1}^{\infty}\left(\int_{\gamma=0}^{t}T_\infty\,\mathbf{C}_{x,m}\mathbf{C}_{y,n}\mathbf{C}_{z,p}d\gamma\right)\mathbf{S}_{x,m}\mathbf{S}_{y,n}\hat{\mathbf{S}}_{z,p}$$

now,

$$\int_{\gamma=0}^{t}T_\infty\,\mathbf{C}_{x,m}\mathbf{C}_{y,n}\mathbf{C}_{z,p}d\gamma$$
$$=\int_{\gamma=0}^{t}T_\infty\cdot e^{-\beta_{x,m}^2\alpha(t-\gamma)/L_x^2}\cdot e^{-\beta_{y,n}^2\alpha(t-\gamma)/L_y^2}\cdot e^{-\beta_{z,p}^2\alpha(t-\gamma)/L_z^2}d\gamma$$

For simplicity, take T_∞ to be a constant. Then

$$T_\infty\int_{\gamma=0}^{t}e^{-\beta_{x,m}^2\alpha(t-\gamma)/L_x^2}\cdot e^{-\beta_{y,n}^2\alpha(t-\gamma)/L_y^2}\cdot e^{-\beta_{z,p}^2\alpha(t-\gamma)/L_z^2}d\gamma=T_\infty\int_{\gamma=0}^{t}e^{-(t-\gamma)\cdot\alpha\cdot(\beta_{x,m}^2/L_x^2+\beta_{y,n}^2/L_y^2+\beta_{z,p}^2/L_z^2)}\,d\gamma$$
$$=T_\infty\int_{\gamma=0}^{t}e^{-\Psi(t-\gamma)}\,d\gamma$$
$$=\frac{T_\infty}{\Psi}(1-e^{-\Psi t})$$

where

$$\Psi = \alpha\left(\frac{\beta_{x,m}^2}{L_x^2} + \frac{\beta_{y,n}^2}{L_y^2} + \frac{\beta_{z,p}^2}{L_z^2}\right)$$

then

$$T_{bc}(\mathbf{G}_{XYZ}) = 8T_\infty \frac{\alpha}{\kappa}\left[\frac{h_x}{L_x}\sum_{m=1}^{\infty}\sum_{n=1}^{\infty}\sum_{p=1}^{\infty}\frac{1}{\Psi}(1-e^{-\Psi t})\hat{\mathbf{S}}_{x,m}\mathbf{S}_{y,n}\mathbf{S}_{z,p}\right.$$
$$+\frac{h_y}{L_y}\sum_{m=1}^{\infty}\sum_{n=1}^{\infty}\sum_{p=1}^{\infty}\frac{1}{\Psi}(1-e^{-\Psi t})\mathbf{S}_{x,m}\hat{\mathbf{S}}_{y,n}\mathbf{S}_{z,p}$$
$$\left.+\frac{h_z}{L_z}\sum_{m=1}^{\infty}\sum_{n=1}^{\infty}\sum_{p=1}^{\infty}\frac{1}{\Psi}(1-e^{-\Psi t})\mathbf{S}_{x,m}\mathbf{S}_{y,n}\hat{\mathbf{S}}_{z,p}\right]$$
$$\Psi = \alpha\left(\frac{\beta_{x,m}^2}{L_x^2} + \frac{\beta_{y,n}^2}{L_y^2} + \frac{\beta_{z,p}^2}{L_z^2}\right)$$
$$\hat{\mathbf{S}}_{x,m} = \frac{\beta_{x,m}^2 + Bi_x^2}{\beta_{x,m}^2 + Bi_x^2 + Bi_x}\cdot\cos\left(\beta_{x,m}\frac{x}{L_x}\right)\cdot\cos(\beta_{x,m})$$
$$\mathbf{S}_{x,m} = \frac{\beta_{x,m}^2 + Bi_x^2}{\beta_{x,m}^2 + Bi_x^2 + Bi_x}\cdot\cos\left(\beta_{x,m}\frac{x}{L_x}\right)\cdot\frac{1}{\beta_{x,m}}\sin(\beta_{x,m})$$

and similar for $\hat{\mathbf{S}}_{y,n}, \mathbf{S}_{y,n}$, etc.

An important note is that the ambient temperature T_∞ is referenced to the initial temperature. For example, if:

- Initial temperature = 15 °C
- Ambient temperature = 35 °C
- Then, the ambient temperature used for calculation in the equation above would be (35 - 15) = 20 °C

That is,

$$T_\infty^{for\cdot calculation} = T_\infty - T_i$$

Decomposition into steady and unsteady components.

Inspection of T_{bc} shows a steady and an unsteady component,

$$T_{bc}(\mathbf{G}_{XYZ}) = 8T_\infty \frac{\alpha}{\kappa}[\frac{h_x}{L_x}\sum_{m=1}^{\infty}\sum_{n=1}^{\infty}\sum_{p=1}^{\infty}\frac{1}{\Psi}(1-e^{-\Psi t})\hat{\mathbf{S}}_{x,m}\mathbf{S}_{y,n}\mathbf{S}_{z,p} + \frac{h_y}{L_y}\sum_{m=1}^{\infty}\sum_{n=1}^{\infty}\sum_{p=1}^{\infty}\frac{1}{\Psi}(1-e^{-\Psi t})\mathbf{S}_{x,m}\hat{\mathbf{S}}_{y,n}\mathbf{S}_{z,p} + \frac{h_z}{L_z}\sum_{m=1}^{\infty}\sum_{n=1}^{\infty}\sum_{p=1}^{\infty}\frac{1}{\Psi}(1-e^{-\Psi t})\mathbf{S}_{x,m}\mathbf{S}_{y,n}\hat{\mathbf{S}}_{z,p}]$$

$$T_{bc}(\mathbf{G}_{XYZ}) = 8T_\infty \frac{\alpha}{\kappa}[\frac{h_x}{L_x}\sum_{m=1}^{\infty}\sum_{n=1}^{\infty}\sum_{p=1}^{\infty}\frac{1}{\Psi}\hat{\mathbf{S}}_{x,m}\mathbf{S}_{y,n}\mathbf{S}_{z,p} - \frac{h_x}{L_x}\sum_{m=1}^{\infty}\sum_{n=1}^{\infty}\sum_{p=1}^{\infty}\frac{1}{\Psi}\cdot e^{-\Psi t}\cdot\hat{\mathbf{S}}_{x,m}\mathbf{S}_{y,n}\mathbf{S}_{z,p} + \frac{h_y}{L_y}\sum_{m=1}^{\infty}\sum_{n=1}^{\infty}\sum_{p=1}^{\infty}\frac{1}{\Psi}\mathbf{S}_{x,m}\hat{\mathbf{S}}_{y,n}\mathbf{S}_{z,p} - \frac{h_y}{L_y}\sum_{m=1}^{\infty}\sum_{n=1}^{\infty}\sum_{p=1}^{\infty}\frac{1}{\Psi}\cdot e^{-\Psi t}\cdot\mathbf{S}_{x,m}\hat{\mathbf{S}}_{y,n}\mathbf{S}_{z,p} + \frac{h_z}{L_z}\sum_{m=1}^{\infty}\sum_{n=1}^{\infty}\sum_{p=1}^{\infty}\frac{1}{\Psi}\mathbf{S}_{x,m}\mathbf{S}_{y,n}\hat{\mathbf{S}}_{z,p} - \frac{h_z}{L_z}\sum_{m=1}^{\infty}\sum_{n=1}^{\infty}\sum_{p=1}^{\infty}\frac{1}{\Psi}\cdot e^{-\Psi t}\cdot\mathbf{S}_{x,m}\mathbf{S}_{y,n}\hat{\mathbf{S}}_{z,p}]$$

Gathering the steady and unsteady terms together

$$T_{bc}(\mathbf{G}_{XYZ}) = 8T_\infty \frac{\alpha}{\kappa}[\frac{h_x}{L_x}\sum_{m=1}^{\infty}\sum_{n=1}^{\infty}\sum_{p=1}^{\infty}\frac{1}{\Psi}\hat{\mathbf{S}}_{x,m}\mathbf{S}_{y,n}\mathbf{S}_{z,p} + \frac{h_y}{L_y}\sum_{m=1}^{\infty}\sum_{n=1}^{\infty}\sum_{p=1}^{\infty}\frac{1}{\Psi}\mathbf{S}_{x,m}\hat{\mathbf{S}}_{y,n}\mathbf{S}_{z,p} + \frac{h_z}{L_z}\sum_{m=1}^{\infty}\sum_{n=1}^{\infty}\sum_{p=1}^{\infty}\frac{1}{\Psi}\mathbf{S}_{x,m}\mathbf{S}_{y,n}\hat{\mathbf{S}}_{z,p}] - 8T_\infty \frac{\alpha}{\kappa}[\frac{h_x}{L_x}\sum_{m=1}^{\infty}\sum_{n=1}^{\infty}\sum_{p=1}^{\infty}\frac{1}{\Psi}\cdot e^{-\Psi t}\cdot\hat{\mathbf{S}}_{x,m}\mathbf{S}_{y,n}\mathbf{S}_{z,p} + \frac{h_y}{L_y}\sum_{m=1}^{\infty}\sum_{n=1}^{\infty}\sum_{p=1}^{\infty}\frac{1}{\Psi}\cdot e^{-\Psi t}\cdot\mathbf{S}_{x,m}\hat{\mathbf{S}}_{y,n}\mathbf{S}_{z,p} + \frac{h_z}{L_z}\sum_{m=1}^{\infty}\sum_{n=1}^{\infty}\sum_{p=1}^{\infty}\frac{1}{\Psi}\cdot e^{-\Psi t}\cdot\mathbf{S}_{x,m}\mathbf{S}_{y,n}\hat{\mathbf{S}}_{z,p}]$$

The steady term

$$T_{bc,s}(\mathbf{G}_{XYZ}) = 8T_\infty \frac{\alpha}{\kappa}\left[\frac{h_x}{L_x}\sum_{m=1}^{\infty}\sum_{n=1}^{\infty}\sum_{p=1}^{\infty}\frac{1}{\Psi}\hat{\mathbf{S}}_{x,m}\mathbf{S}_{y,n}\mathbf{S}_{z,p} + \frac{h_y}{L_y}\sum_{m=1}^{\infty}\sum_{n=1}^{\infty}\sum_{p=1}^{\infty}\frac{1}{\Psi}\mathbf{S}_{x,m}\hat{\mathbf{S}}_{y,n}\mathbf{S}_{z,p} + \frac{h_z}{L_z}\sum_{m=1}^{\infty}\sum_{n=1}^{\infty}\sum_{p=1}^{\infty}\frac{1}{\Psi}\mathbf{S}_{x,m}\mathbf{S}_{y,n}\hat{\mathbf{S}}_{z,p}\right]$$

must be the solution to the steady state problem, which in this case is

$$T_{bc,s}(\mathbf{G}_{XYZ}) = T_\infty$$

Thus

$$T_{bc}(\mathbf{G}_{XYZ}) = T_\infty - 8T_\infty \frac{\alpha}{\kappa}\left[\frac{h_x}{L_x}\sum_{m=1}^{\infty}\sum_{n=1}^{\infty}\sum_{p=1}^{\infty}\frac{1}{\Psi}\cdot e^{-\Psi t}\cdot\hat{\mathbf{S}}_{x,m}\mathbf{S}_{y,n}\mathbf{S}_{z,p} + \frac{h_y}{L_y}\sum_{m=1}^{\infty}\sum_{n=1}^{\infty}\sum_{p=1}^{\infty}\frac{1}{\Psi}\cdot e^{-\Psi t}\cdot\mathbf{S}_{x,m}\hat{\mathbf{S}}_{y,n}\mathbf{S}_{z,p} + \frac{h_z}{L_z}\sum_{m=1}^{\infty}\sum_{n=1}^{\infty}\sum_{p=1}^{\infty}\frac{1}{\Psi}\cdot e^{-\Psi t}\cdot\mathbf{S}_{x,m}\mathbf{S}_{y,n}\hat{\mathbf{S}}_{z,p}\right]$$

Energy generation component

Energy generation contributes:

$$T_{egen}(\mathbf{G}_{XYZ}) = \int_{\gamma=0}^{t}\int_{z'=0}^{L_z}\int_{y'=0}^{L_y}\int_{x'=0}^{L_x}\frac{1}{\rho c}\dot{e}_{gen}(\gamma)\cdot\mathbf{G}_{X23}(x,t|x',\gamma)\cdot\mathbf{G}_{Y23}(y,t|y',\gamma)\cdot\mathbf{G}_{Z23}(z,t|z',\gamma)dx'dy'dz'd\gamma$$

Recall:

$$\int_{x'=0}^{L_x}\mathbf{G}_{X23}(x,t|x',\gamma)dx' = 2\sum_{m=1}^{\infty}\mathbf{C}_{x,m}\cdot\mathbf{S}_{x,m}$$

$$\mathbf{C}_{x,m} = e^{-\beta_{x,m}^2\alpha(t-\gamma)/L_x^2}$$

$$\mathbf{S}_{x,m} = \frac{\beta_{x,m}^2 + Bi_x^2}{\beta_{x,m}^2 + Bi_x^2 + Bi_x}\cdot\cos\left(\beta_{x,m}\frac{x}{L_x}\right)\cdot\frac{1}{\beta_{x,m}}\sin(\beta_{x,m})$$

Thus,

$$T_{egen}(\mathbf{G}_{XYZ}) = 8\int_{\gamma=0}^{t}\frac{1}{\rho c}\dot{e}_{gen}(\gamma)\sum_{m=1}^{\infty}\mathbf{C}_{x,m}\,\mathbf{S}_{x,m}\sum_{n=1}^{\infty}\mathbf{C}_{y,n}\,\mathbf{S}_{y,n}\sum_{p=1}^{\infty}\mathbf{C}_{z,p}\,\mathbf{S}_{z,p}d\gamma$$
$$= 8\int_{\gamma=0}^{t}\sum_{m=1}^{\infty}\sum_{n=1}^{\infty}\sum_{p=1}^{\infty}\frac{1}{\rho c}\dot{e}_{gen}(\gamma)\,\mathbf{C}_{x,m}\mathbf{C}_{y,n}\mathbf{C}_{z,p}\mathbf{S}_{x,m}\mathbf{S}_{y,n}\mathbf{S}_{z,p}d\gamma$$

Recall that

$$\frac{1}{\rho c}\dot{e}_{gen} = 2\Delta T_a G t e^{-Gt^2}$$
$$\frac{1}{\rho c}\dot{e}_{gen}(\gamma) = 2\Delta T_a G \gamma e^{-G\gamma^2}$$

Our time integrals will be (not writing in the summation signs for now):

$$\int_{\gamma=0}^{t}\frac{1}{\rho c}\dot{e}_{gen}(\gamma)\,\mathbf{C}_{x,m}\mathbf{C}_{y,n}\mathbf{C}_{z,p}d\gamma = \int_{\gamma=0}^{t}\left(2\Delta T_a G\gamma e^{-G\gamma^2}\right)\left(e^{-\beta_{x,m}^2\alpha(t-\gamma)/L_x^2}\right)\left(e^{-\beta_{y,n}^2\alpha(t-\gamma)/L_y^2}\right)\left(e^{-\beta_{z,p}^2\alpha(t-\gamma)/L_z^2}\right)d\gamma$$
$$= 2\Delta T_a G\int_{\gamma=0}^{t}\gamma\, e^{-G\gamma^2-\beta_{x,m}^2\alpha(t-\gamma)/L_x^2-\beta_{y,n}^2\alpha(t-\gamma)/L_y^2-\beta_{z,p}^2\alpha(t-\gamma)/L_z^2}d\gamma$$
$$= (2\Delta T_a G)e^{-\left(\frac{\beta_{x,m}^2\alpha t}{L_x^2}+\frac{\beta_{y,n}^2\alpha t}{L_y^2}+\frac{\beta_{z,p}^2\alpha t}{L_z^2}\right)}\int_{\gamma=0}^{t}\gamma\, e^{\left(\frac{\beta_{x,m}^2\alpha\gamma}{L_x^2}+\frac{\beta_{y,n}^2\alpha\gamma}{L_y^2}+\frac{\beta_{z,p}^2\alpha\gamma}{L_z^2}-G\gamma^2\right)}d\gamma$$

From experience with symbolic engines like Wolfram Alpha, the closed-form solution of this integral doesn't seem to be well-behaved, so compute it numerically.

Then,

$$T_{egen}(\mathbf{G}_{XYZ}) = 8\int_{\gamma=0}^{t}\sum_{m=1}^{\infty}\sum_{n=1}^{\infty}\sum_{p=1}^{\infty}\frac{1}{\rho c}\dot{e}_{gen}(\gamma)\,\mathbf{C}_{x,m}\mathbf{C}_{y,n}\mathbf{C}_{z,p}\mathbf{S}_{x,m}\mathbf{S}_{y,n}\mathbf{S}_{z,p}d\gamma$$
$$= 16\Delta T_a G\sum_{m=1}^{\infty}\sum_{n=1}^{\infty}\sum_{p=1}^{\infty}e^{-\left(\frac{\beta_{x,m}^2\alpha t}{L_x^2}+\frac{\beta_{y,n}^2\alpha t}{L_y^2}+\frac{\beta_{z,p}^2\alpha t}{L_z^2}\right)}\int_{\gamma=0}^{t}\gamma\, e^{\left(\frac{\beta_{x,m}^2\alpha\gamma}{L_x^2}+\frac{\beta_{y,n}^2\alpha\gamma}{L_y^2}+\frac{\beta_{z,p}^2\alpha\gamma}{L_z^2}-G\gamma^2\right)}d\gamma\cdot\mathbf{S}_{x,m}\mathbf{S}_{y,n}\mathbf{S}_{z,p}$$
$$= 16\Delta T_a G\sum_{m=1}^{\infty}\sum_{n=1}^{\infty}\sum_{p=1}^{\infty}\mathbf{S}_{x,m}\,\mathbf{S}_{y,n}\mathbf{S}_{z,p}\cdot e^{-\Psi t}\int_{\gamma=0}^{t}\gamma\, e^{(\Psi\gamma-G\gamma^2)}d\gamma$$
$$= 16\Delta T_a G\sum_{m=1}^{\infty}\sum_{n=1}^{\infty}\sum_{p=1}^{\infty}\mathbf{S}_{x,m}\,\mathbf{S}_{y,n}\mathbf{S}_{z,p}\cdot\int_{\gamma=0}^{t}\gamma\, e^{(\Psi(\gamma-t)-G\gamma^2)}d\gamma$$

where

$$\Psi = \alpha\left(\frac{\beta_{x,m}^2}{L_x^2}+\frac{\beta_{y,n}^2}{L_y^2}+\frac{\beta_{z,p}^2}{L_z^2}\right)$$
$$\mathbf{S}_{x,m} = \frac{\beta_{x,m}^2+Bi_x^2}{\beta_{x,m}^2+Bi_x^2+Bi_x}\cdot\cos\left(\beta_{x,m}\frac{x}{L_x}\right)\cdot\frac{1}{\beta_{x,m}}\sin\left(\beta_{x,m}\right)$$
$$\mathbf{S}_{y,n} = \cdots$$
$$\mathbf{S}_{z,p} = \cdots$$

Let's look at that time integral. Wolfram Alpha integrates this

integrate y exp(P*y - G*y^2) dy from 0 to t

as:

$$\int_{\gamma=0}^{t} \gamma\, e^{(\Psi\gamma - G\gamma^2)} d\gamma$$

$$= \frac{\sqrt{\pi}\cdot\Psi\cdot e^{\Psi^2/4G}\left[erf\left(\frac{2Gt-\Psi}{2\sqrt{G}}\right)+erf\left(\frac{\Psi}{2\sqrt{G}}\right)\right]-2\sqrt{G}\left(e^{t(\Psi-Gt)}-1\right)}{4G^{3/2}}$$

This is a numerically troublesome result: the term $e^{\Psi^2/4G}$ is huge, effectively infinite.

For practical purposes we will calculate the time integral numerically.

Summary

The temperature solution, scaled to a nonzero initial temperature, is

$$T = T_{bc} + T_{egen} + T_i,$$

Where T_{bc} is the component of the temperature due to the boundary conditions; in the solution below, the steady-state and unsteady solutions have been partitioned

$$T_{bc} = \hat{T}_\infty\{1 - 8\frac{\alpha}{\kappa}[\frac{h_x}{L_x}\sum_{m=1}^{\infty}\sum_{n=1}^{\infty}\sum_{p=1}^{\infty}\frac{1}{\Psi}\cdot e^{-\Psi t}\cdot\hat{\mathbf{S}}_{x,m}\mathbf{S}_{y,n}\mathbf{S}_{z,p}$$
$$+\frac{h_y}{L_y}\sum_{m=1}^{\infty}\sum_{n=1}^{\infty}\sum_{p=1}^{\infty}\frac{1}{\Psi}\cdot e^{-\Psi t}\cdot\mathbf{S}_{x,m}\hat{\mathbf{S}}_{y,n}\mathbf{S}_{z,p}$$
$$+\frac{h_z}{L_z}\sum_{m=1}^{\infty}\sum_{n=1}^{\infty}\sum_{p=1}^{\infty}\frac{1}{\Psi}\cdot e^{-\Psi t}\cdot\mathbf{S}_{x,m}\mathbf{S}_{y,n}\hat{\mathbf{S}}_{z,p}]\}$$

$$\Psi = \alpha\left(\frac{\beta_{x,m}^2}{L_x^2}+\frac{\beta_{y,n}^2}{L_y^2}+\frac{\beta_{z,p}^2}{L_z^2}\right)$$

$$\hat{\mathbf{S}}_{x,m} = \frac{\beta_{x,m}^2+Bi_x^2}{\beta_{x,m}^2+Bi_x^2+Bi_x}\cdot\cos\left(\beta_{x,m}\frac{x}{L_x}\right)\cdot\cos(\beta_{x,m})$$

$$\mathbf{S}_{x,m} = \frac{\beta_{x,m}^2+Bi_x^2}{\beta_{x,m}^2+Bi_x^2+Bi_x}\cdot\cos\left(\beta_{x,m}\frac{x}{L_x}\right)\cdot\frac{1}{\beta_{x,m}}\sin(\beta_{x,m})$$

$$\beta_{*,m}tan\beta_{*,m} = Bi_* = \frac{h_*L_*}{\kappa}$$

and similar for $\mathbf{S}_{y,n}$, $\hat{\mathbf{S}}_{y,n}$, etc., and where $_*$ is the wild card for x, y,or z; and

- for x, $L_x = W/2$
- for y, $L_y = D/2$

- for z, $L_z = H$
- An important note is that $\hat{T}_\infty$ is the ambient temperature referenced to the initial temperature. For example, if:
- initial temperature = 15 °C
- ambient temperature = 35 °C
- then ambient temperature used for calculation in the equation above would be (35 - 15) = 20 °C

That is,

$$\hat{T}_\infty = T_\infty - T_i$$

The temperature component due to internal energy generation T_{egen} is

$$T_{egen} = 16\Delta T_a G \sum_{m=1}^{\infty}\sum_{n=1}^{\infty}\sum_{p=1}^{\infty} \mathbf{S}_{x,m}\,\mathbf{S}_{y,n}\mathbf{S}_{z,p} \cdot \int_{\gamma=0}^{t} \gamma\, e^{(\Psi(\gamma-t)-G\gamma^2)} d\gamma$$

The integral is computed numerically.

Derivation of the Green's function solution for temperature gradient
The gradient is:

$$\begin{aligned}\nabla T &= \left[\frac{\partial T}{\partial x}, \frac{\partial T}{\partial y}, \frac{\partial T}{\partial z}\right] \\ &= \left[\frac{\partial}{\partial x}(T_{bc} + T_{egen}), \frac{\partial}{\partial y}(T_{bc} + T_{egen}), \frac{\partial}{\partial z}(T_{bc} + T_{egen})\right] \\ &= \left[\frac{\partial T_{bc}}{\partial x} + \frac{\partial T_{egen}}{\partial x}, \frac{\partial T_{bc}}{\partial y} + \frac{\partial T_{egen}}{\partial y}, \frac{\partial T_{bc}}{\partial z} + \frac{\partial T_{egen}}{\partial z}\right]\end{aligned}$$

And the magnitude of the gradient $|\nabla T|$ is

$$\begin{aligned}|\nabla T| &= \sqrt{(\frac{\partial T}{\partial x})^2 + (\frac{\partial T}{\partial y})^2 + (\frac{\partial T}{\partial z})^2} \\ &= \sqrt{(\frac{\partial T_{bc}}{\partial x} + \frac{\partial T_{egen}}{\partial x})^2 + (\frac{\partial T_{bc}}{\partial y} + \frac{\partial T_{egen}}{\partial y})^2 + (\frac{\partial T_{bc}}{\partial z} + \frac{\partial T_{egen}}{\partial z})^2}\end{aligned}$$

T is a function of time as well as of space, and ideally we want to pinpoint the time

as well as the location of the maximum gradient.

We need to determine derivatives of the components of the temperature T_{bc} and T_{egen}, but can such derivatives be calculated by distributing the derivatives into the series? In other words, is the derivative of, e.g., T_{egen} the sum of the derivatives of the terms of the series? That is:

$$\frac{\partial}{\partial x}T_{egen} = \frac{\partial}{\partial x}\left[16\Delta T_a G \sum_{m=1}^{\infty}\sum_{n=1}^{\infty}\sum_{p=1}^{\infty}\mathbf{S}_{x,m}\,\mathbf{S}_{y,n}\mathbf{S}_{z,p}\cdot\int_{\gamma=0}^{t}\gamma\, e^{\left(\Psi(\gamma-t)-G\gamma^2\right)}d\gamma\right]$$
$$= 16\Delta T_a G \sum_{m=1}^{\infty}\sum_{n=1}^{\infty}\sum_{p=1}^{\infty}\frac{\partial\mathbf{S}_{x,m}}{\partial x}\mathbf{S}_{y,n}\mathbf{S}_{z,p}\cdot\int_{\gamma=0}^{t}\gamma\, e^{\left(\Psi(\gamma-t)-G\gamma^2\right)}d\gamma]$$

Derivatives of the boundary condition component

$$\frac{\partial T_{bc}}{\partial x} = -8T_\infty\frac{\alpha}{\kappa}[\frac{h_x}{L_x}\sum_{m=1}^{\infty}\sum_{n=1}^{\infty}\sum_{p=1}^{\infty}\frac{1}{\Psi}\cdot e^{-\Psi t}\cdot\frac{\partial\hat{\mathbf{S}}_{x,m}}{\partial x}\mathbf{S}_{y,n}\mathbf{S}_{z,p}$$
$$+\frac{h_y}{L_y}\sum_{m=1}^{\infty}\sum_{n=1}^{\infty}\sum_{p=1}^{\infty}\frac{1}{\Psi}\cdot e^{-\Psi t}\cdot\frac{\partial\mathbf{S}_{x,m}}{\partial x}\hat{\mathbf{S}}_{y,n}\mathbf{S}_{z,p}$$
$$+\frac{h_z}{L_z}\sum_{m=1}^{\infty}\sum_{n=1}^{\infty}\sum_{p=1}^{\infty}\frac{1}{\Psi}\cdot e^{-\Psi t}\cdot\frac{\partial\mathbf{S}_{x,m}}{\partial x}\mathbf{S}_{y,n}\hat{\mathbf{S}}_{z,p}]$$

$$\frac{\partial T_{bc}}{\partial y} = -8T_\infty\frac{\alpha}{\kappa}[\frac{h_x}{L_x}\sum_{m=1}^{\infty}\sum_{n=1}^{\infty}\sum_{p=1}^{\infty}\frac{1}{\Psi}\cdot e^{-\Psi t}\cdot\hat{\mathbf{S}}_{x,m}\frac{\partial\mathbf{S}_{y,n}}{\partial y}\mathbf{S}_{z,p}$$
$$+\frac{h_y}{L_y}\sum_{m=1}^{\infty}\sum_{n=1}^{\infty}\sum_{p=1}^{\infty}\frac{1}{\Psi}\cdot e^{-\Psi t}\cdot\mathbf{S}_{x,m}\frac{\partial\hat{\mathbf{S}}_{y,n}}{\partial y}\mathbf{S}_{z,p}$$
$$+\frac{h_z}{L_z}\sum_{m=1}^{\infty}\sum_{n=1}^{\infty}\sum_{p=1}^{\infty}\frac{1}{\Psi}\cdot e^{-\Psi t}\cdot\mathbf{S}_{x,m}\frac{\partial\mathbf{S}_{y,n}}{\partial y}\hat{\mathbf{S}}_{z,p}]$$

$$\frac{\partial T_{bc}}{\partial z} = -8T_\infty\frac{\alpha}{\kappa}[\frac{h_x}{L_x}\sum_{m=1}^{\infty}\sum_{n=1}^{\infty}\sum_{p=1}^{\infty}\frac{1}{\Psi}\cdot e^{-\Psi t}\cdot\hat{\mathbf{S}}_{x,m}\mathbf{S}_{y,n}\frac{\partial\mathbf{S}_{z,p}}{\partial z}$$
$$+\frac{h_y}{L_y}\sum_{m=1}^{\infty}\sum_{n=1}^{\infty}\sum_{p=1}^{\infty}\frac{1}{\Psi}\cdot e^{-\Psi t}\cdot\mathbf{S}_{x,m}\hat{\mathbf{S}}_{y,n}\frac{\partial\mathbf{S}_{z,p}}{\partial z}$$
$$+\frac{h_z}{L_z}\sum_{m=1}^{\infty}\sum_{n=1}^{\infty}\sum_{p=1}^{\infty}\frac{1}{\Psi}\cdot e^{-\Psi t}\cdot\mathbf{S}_{x,m}\mathbf{S}_{y,n}\frac{\partial\hat{\mathbf{S}}_{z,p}}{\partial z}]$$

We might be able to speed things up by factoring α out of Ψ; for example

$$\frac{\partial T_{bc}}{\partial x} = -8T_\infty \frac{1}{\kappa}\left[\frac{h_x}{L_x}\sum_{m=1}^{\infty}\sum_{n=1}^{\infty}\sum_{p=1}^{\infty}\frac{1}{\psi}\cdot e^{-\Psi t}\cdot\frac{\partial \hat{\mathbf{S}}_{x,m}}{\partial x}\mathbf{S}_{y,n}\mathbf{S}_{z,p}\right.$$
$$+\frac{h_y}{L_y}\sum_{m=1}^{\infty}\sum_{n=1}^{\infty}\sum_{p=1}^{\infty}\frac{1}{\psi}\cdot e^{-\Psi t}\cdot\frac{\partial \mathbf{S}_{x,m}}{\partial x}\hat{\mathbf{S}}_{y,n}\mathbf{S}_{z,p}$$
$$\left.\frac{h_z}{L_z}\sum_{m=1}^{\infty}\sum_{n=1}^{\infty}\sum_{p=1}^{\infty}\frac{1}{\psi}\cdot e^{-\Psi t}\cdot\frac{\partial \mathbf{S}_{x,m}}{\partial x}\mathbf{S}_{y,n}\hat{\mathbf{S}}_{z,p}\right]$$

where

$$\psi = \left(\frac{\beta_{x,m}^2}{L_x^2}+\frac{\beta_{y,m}^2}{L_y^2}+\frac{\beta_{z,m}^2}{L_z^2}\right)$$

Derivatives of the energy generation component

$$\frac{\partial T_{egen}}{\partial x} = 16\Delta T_a G\sum_{m=1}^{\infty}\sum_{n=1}^{\infty}\sum_{p=1}^{\infty}\frac{\partial \mathbf{S}_{x,m}}{\partial x}\mathbf{S}_{y,n}\mathbf{S}_{z,p}\cdot\int_{\gamma=0}^{t}\gamma\, e^{\left(\Psi(\gamma-t)-G\gamma^2\right)}d\gamma$$

$$\frac{\partial T_{egen}}{\partial y} = 16\Delta T_a G\sum_{m=1}^{\infty}\sum_{n=1}^{\infty}\sum_{p=1}^{\infty}\mathbf{S}_{x,m}\frac{\partial \mathbf{S}_{y,n}}{\partial y}\mathbf{S}_{z,p}\cdot\int_{\gamma=0}^{t}\gamma\, e^{\left(\Psi(\gamma-t)-G\gamma^2\right)}d\gamma$$

$$\frac{\partial T_{egen}}{\partial z} = 16\Delta T_a G\sum_{m=1}^{\infty}\sum_{n=1}^{\infty}\sum_{p=1}^{\infty}\mathbf{S}_{x,m}\mathbf{S}_{y,n}\frac{\partial \mathbf{S}_{z,p}}{\partial z}\cdot\int_{\gamma=0}^{t}\gamma\, e^{\left(\Psi(\gamma-t)-G\gamma^2\right)}d\gamma$$

Derivatives of the spatial terms

The only terms the derivatives act on are $\mathbf{S}_{\mathrm{x,m}}$, $\hat{\mathbf{S}}_{\mathrm{x,m}}$, etc.

$$\frac{\partial \mathbf{S}_{\mathrm{x,m}}}{\partial \mathrm{x}} = \frac{\partial}{\partial \mathrm{x}}\left(\frac{\beta_{\mathrm{x,m}}^2+\mathrm{Bi}_{\mathrm{x}}^2}{\beta_{\mathrm{x,m}}^2+\mathrm{Bi}_{\mathrm{x}}^2+\mathrm{Bi}_{\mathrm{x}}}\cdot\cos\left(\beta_{\mathrm{x,m}}\frac{\mathrm{x}}{\mathrm{L}_{\mathrm{x}}}\right)\cdot\frac{1}{\beta_{\mathrm{x,m}}}\sin\left(\beta_{\mathrm{x,m}}\right)\right)$$
$$= -\frac{\beta_{\mathrm{x,m}}^2+\mathrm{Bi}_{\mathrm{x}}^2}{\beta_{\mathrm{x,m}}^2+\mathrm{Bi}_{\mathrm{x}}^2+\mathrm{Bi}_{\mathrm{x}}}\cdot\frac{1}{\mathrm{L}_{\mathrm{x}}}\cdot\sin\left(\beta_{\mathrm{x,m}}\right)\cdot\sin\left(\beta_{\mathrm{x,m}}\frac{\mathrm{x}}{\mathrm{L}_{\mathrm{x}}}\right)$$

$$\frac{\partial \hat{\mathbf{S}}_{\mathrm{x,m}}}{\partial \mathrm{x}} = \frac{\partial}{\partial \mathrm{x}}\left(\frac{\beta_{\mathrm{x,m}}^2+\mathrm{Bi}_{\mathrm{x}}^2}{\beta_{\mathrm{x,m}}^2+\mathrm{Bi}_{\mathrm{x}}^2+\mathrm{Bi}_{\mathrm{x}}}\cdot\cos\left(\beta_{\mathrm{x,m}}\frac{\mathrm{x}}{\mathrm{L}_{\mathrm{x}}}\right)\cdot\cos\left(\beta_{\mathrm{x,m}}\right)\right)$$
$$= -\frac{\beta_{\mathrm{x,m}}^2+\mathrm{Bi}_{\mathrm{x}}^2}{\beta_{\mathrm{x,m}}^2+\mathrm{Bi}_{\mathrm{x}}^2+\mathrm{Bi}_{\mathrm{x}}}\cdot\frac{\beta_{\mathrm{x,m}}}{\mathrm{L}_{\mathrm{x}}}\cdot\cos\left(\beta_{\mathrm{x,m}}\right)\cdot\sin\left(\beta_{\mathrm{x,m}}\frac{\mathrm{x}}{\mathrm{L}_{\mathrm{x}}}\right)$$

etc.